FUNDAMENTALS OF BUBBLE TRANSPORT IN AN ULTRASONICALLY ASSISTED SEPARATION PROCESS

by

JENNIFER LYNN MALERS

Submitted in partial fulfillment of the requirements

For the degree of Doctor of Philosophy

Dissertation Advisor: Dr. Donald L. Feke

Department of Chemical Engineering

CASE WESTERN RESERVE UNIVERSITY

May 2008

CASE WESTERN RESERVE UNIVERSITY

SCHOOL OF GRADUATE STUDIES

We hereby approve the dissertation of

Jennifer Lynn Malers

candidate for the Ph.D. degree *.

(signed) Dr. Donald Feke
(chair of the committee)

Dr. J. Adin Mann Jr.

Dr. Robert Edwards

Dr. Dov Hazony

(date) 03/12/2008

*We also certify that written approval has been obtained for any proprietary material contained therein.

Table of Contents

List of Tables

List of Figures

Acknowledgements

First I would like to acknowledge God for giving me the opportunities that He has in my life. I may not be on the path I originally intended, but I'm trusting that He has a better idea of what's best for me than I do. Second I would like to thank my parents who have managed to put up with a daughter who was in college for ten years with only the occasional comment about when I was going to finally be able to support them. I love you both. And thanks to the rest of my family for their support; I love you all…most of the time anyway.

I would like to thank Dr. Feke for his guidance and for his ability to answer my questions, no matter how many times I managed to ask the same ones over and over again. Also, thank you to the rest of my committee for your comments and suggestions: Dr. Mann, Dr. Edwards, and Dr. Hazony. I may hate making corrections now, but my dissertation will be better because of your help. I would also like to thank the NASA Glenn Research Center for their support under Grant NNC05GA29G and Nestle for their fellowship support.

Thanks to Jason for our acoustic knowledge sessions where we bounced questions off each other before we talked to Dr. Feke so we wouldn't seem quite so stupid. My ego comes out of this with a few less dents because of you. And thanks to Meg. Our trips to get coffee kept me from banging my head against the wall on numerous occasions. And even though I don't drink coffee, my sanity comes out of this with a few more threads attached than had I not had you as a procrastination buddy. You will survive. Also,

thanks to all my other friends who kept me from taking myself too seriously. You made my life here memorable.

Nomenclature List

a = radius [m]

$a_{ar}(\theta_d)$ = radius of deformed bubble [m]

a_1 = radius of the larger bubble (bubble 1) [m]

a_2 = radius of the smaller bubble (bubble 2) [m]

a_{j0} = initial radius of bubble j

$$\hat{a} = \frac{a_2}{a_1}$$

$$a_m = \frac{a_1 a_2}{(a_1 + a_2)}$$

A = Hamaker constant [J]

$\hat{A}$ = cubic spline interpolation term

A_c = cross sectional area (m^2)

$\hat{B}$ = cubic spline interpolation term

c = speed of sound [m/s]

c_g = speed of sound through gas [m/s]

c_l = speed of sound through liquid [m/s]

c_p = speed of sound through solid particle [m/s]

C_0 = contribution of external expansion to Λ

$\hat{C}$ = cubic spline interpolation term

$\hat{D}$ = cubic spline interpolation term

D^0_{12} = relative diffusivity due to Brownian motion for two widely separated bubbles

$d_1 = \hat{\rho}-1$

$d_2 = 1+2\hat{\rho}$

$d_3 = 2+3\hat{\rho}$

$d_{1,j} = \frac{d_1}{d_j}$

e_r = unit vector in the radial direction

e_θ = unit vector in the tangential direction

E_{ac} = average energy density [J/m^3]

F = acoustic contrast factor

F_{vdW} = van der Waals force [N]

g = gravity [m/s^2]

G_ρ = density acoustic contrast factor

G_β = compressibility acoustic contrast factor

G(s) = axisymmetric far-field mobility function

$G(\xi)$ = axisymmetric near-field mobility function

$h_0 = r-(a_1+a_2)$

H(s) = asymmetric far-field mobility function

$\bar{I}$ = unit second-order tensor

k = Boltzmann constant = $1.38065 \cdot 10^{-23}$ [kg m^2/s^2 K]

L = surface to surface bubble separation [m]

L_0 = initial surface to surface bubble separation [m]

L(s) = axisymmetric far-field mobility function

$L(\xi)$ = axisymmetric near-field mobility function

$$m = \frac{\left(a_m/h_0\right)^{1/2}}{\hat{\mu}}$$

$M = p = \frac{a^2(\rho_l-\rho_g)g}{3\mu_l}$ = ratio of the buoyancy force to the drag force divided by the velocity; the velocity the bubble would travel with no acoustic force [m/s]

$M(s)$ = asymmetric far-field mobility function

$M(\xi)$ = asymmetric near-field mobility function

M_0 = term in the asymmetric near-field mobility function

M_1 = term in the asymmetric near-field mobility function

$N_{ac} = \frac{q}{p} = \frac{3\kappa E_{ac} F}{(\rho_l-\rho_g)g}$ = ratio of the primary acoustic force to the buoyancy force

$p = \frac{a^2(\rho_l-\rho_g)g}{3\mu_l}$ = ratio of the buoyancy force to the drag force divided by the velocity; the velocity the bubble would travel with no acoustic force [m/s]

p_{12} = pair distribution function; probability that bubble one is at position $\bar{r}$ relative to bubble two.

P = pressure [Pa]

P_{20} = static portion of the component of radial projection which is mainly responsible for bubble deformation [Pa]

$P_s = \sqrt{2\rho_l c_l^2 E_{ac}}$ = pressure amplitude of the unmodulated standing acoustic wave [Pa]

$P_{j0} = \frac{2\sigma_i}{a_{j0}} + P_{atm}$ = pressure inside a bubble [Pa]

P_{atm} = atmospheric pressure [Pa]

$q = \frac{a^2 \kappa E_{ac} F}{3\mu_l}$ [m/s]

Q = general term for mobility functions used in spline calculations

r = center to center bubble separation distance [m]

$\bar{r}$ = vector of the center to center bubble separation distance [m]

$s = \frac{2r}{a_1+a_2}$ = dimensionless bubble separation

s_{far} = value of s up to which the far field mobility functions are valid

s_{near} = value of s at which the near field mobility functions become valid

T = temperature [K]

t = time [s]

v = velocity [m/s]

V_0 = initial volume [m^3]

V_1^0 = initial velocity of bubble 1 [m/s]

V_2^0 = initial velocity of bubble 2 [m/s]

V_1 = velocity of bubble 1 [m/s]

V_2 = velocity of bubble 2 [m/s]

V_{12} = relative velocity of bubble 1 to bubble 2 [m/s]

$V_{12}^0 = V_1^0 - V_2^0$ = relative initial velocity of bubble 1 to bubble 2 [m/s]

V_{p1} = volume of particle 1 [m^3]

V_{p2} = volume of particle 2 [m^3]

V_{vdW} = van der Waals force inter-particle force potential [J]

V_{vdW}^* = the van der Waals potential made dimensionless by dividing by the Hamaker constant

$x(\theta_d)$ = deformation term in $r_{ar}(\theta_d)$ [m]

y = distance of bubble center from pressure antinode [m]

$\alpha = 2\kappa$ [1/m]

$\alpha_{ac} = F_{2,ac}r^2$ = expresses the strength of secondary acoustic forces [Nm = kgm^3/s^2]

β_1 = correction to the Hadamard-Rybczynski drag force for bubble 1

β_2 = correction to the Hadamard-Rybczynski drag force for bubble 2

$\gamma = \frac{1}{\rho c^2}$ = compressibility [1/Pa = ms^2/kg]

γ_p = compressibility of particle [1/Pa = ms^2/kg]

γ_l = compressibility of liquid [1/Pa = ms^2/kg]

$$\Gamma = \kappa Mt\sqrt{1-N_{ac}^2} + \tan^{-1}\left(\frac{N_{ac} + \tan\left[\kappa y_0\right]}{\sqrt{1-N_{ac}^2}}\right)$$

Δx = x coordinate of bubble position [m]

Δy = y coordinate of bubble position [m]

θ_d = polar angle of a point on the bubble surface with respect to the vertical axis for deformation calculations

$\kappa = \frac{\omega}{c}$ = wavenumber [1/m]

λ = wavelength [m]

$\Lambda(\xi)$ = asymptotic solution for the resistance function

Φ_{12} = total interparticle force potential

φ = phase angle

ρ = density [kg/m^3]

ρ_g = density of gas [kg/m^3]

ρ_l = density of liquid [kg/m^3]

ρ_p = density of solid particle [kg/m^3]

$$\hat{\rho} = \frac{\rho_g}{\rho_l} = \frac{\rho_p}{\rho_l}$$

$$\hat{\sigma} = \frac{c_g}{c_l} = \frac{c_p}{c_l}$$

σ_i = interfacial tension [dynes/cm = kg/s^2]

μ_g = viscosity of the gas [Ns/m^2]

μ_l = viscosity of the liquid [Ns/m^2]

$$\hat{\mu} = \frac{\mu_g}{\mu_l}$$

η = polytrophic exponent of the gas (1.4 for a diatomic gas - air)

ξ = s-2

ξ_x = displacement

$$\Psi = \alpha t M \sqrt{N_{ac}^2 - 1} = 2\kappa t M \sqrt{N_{ac}^2 - 1}$$

ω = the angular driving frequency [Hz = 1/s]

ω_j = monopole resonance frequency of bubble j [Hz = 1/s]

ω_1 = monopole resonance frequency of bubble 1 [Hz = 1/s]

ω_2 = monopole resonance frequency of bubble 2 [Hz = 1/s]

$$\omega_j = \frac{1}{a_{j0}} \left(\frac{3\gamma P_{j0}}{\rho_l} - \frac{(3\gamma - 1)2\sigma_i}{\rho_l a_{j0}} \right)^{1/2}$$

∇ = gradient operator

Fundamentals of Bubble Transport in an Ultrasonically Assisted Separation Process

Abstract

By

JENNIFER LYNN MALERS

Previous research endeavors resulted in a process to recover solid particles and oil droplets from aqueous suspensions. This process involves applying a one-dimensional resonant ultrasonic field to the suspension while it is flowing through or resting in a rectangular chamber. The same process has been utilized here for gas bubbles in an aqueous medium. Bubbles in this system move to the acoustic pressure antinodes, based on the density and compressibility of the bubble and the surrounding fluid as well as the driving frequency and the radius of the bubble.

To obtain a fundamental understanding of the movement of a single bubble within the acoustic chamber, a balance of the relevant physical forces was completed: primary acoustic force, buoyancy force, and drag force. The resulting equations could be used to determine the position of a single bubble within the chamber and the velocity at which that bubble would be moving toward those positions.

A microscopic mathematical model was developed to predict the relative trajectory of a bubble pair in an acoustic field. This model not only took into account the primary forces previously discussed, but also inter-bubble effects: secondary acoustic force, van der Waals force, hydrodynamic interactions, and Brownian diffusivity. The trajectory analysis was used to track the movement of the bubble pairs under a variety of operating conditions and the results were compared to experimental data. This data was

then used to calculate volume cleared by the collision of different bubble pairs, thus describing the kinetics of the collision process.

The results from the models were then compared to experimental data obtained by injecting small numbers of bubbles into an acoustic chamber. This comparison was done by taking video of bubbles colliding, mapping their path, and comparing this to the trajectory determined from the bubble pair model. The projected trajectory and the experimental trajectory were shown to be in good agreement. The model can then be used to calculate the collision time for a variety of energy densities at experimental conditions. This relationship can then be used to determine the energy density of the experimental system based on the observed collision time.

Introduction and Research Objectives

1.1 Purpose

The use of ultrasonic fields to induce phase separations of a dispersed solid, immiscible liquid, or gas within a suspending liquid phase has received increasing attention over the past two decades. Dissolved and entrained gases, and thus gas bubbles, have the potential to produce transport inefficiencies in closed-loop flow systems and also have the possibility of causing materials failure. Research conducted in this study investigates the applicability of the use of a resonant ultrasonic wave field to entrap and harvest gas bubbles from a surrounding liquid for potential applications in microgravity environments. It is hoped that by subjecting the bubbles to a standing acoustic field, their migration and coalescence can be managed, allowing for greater ease of removal.

This research aims to develop a fundamental understanding of the effect of forces induced by resonant ultrasonic fields on the entrapment and coalescence phenomena. Modeling efforts illustrate the relationship between the size of bubbles, their sphericity, acoustic field parameters (frequency and intensity), bubble equilibrium position relative to acoustic pressure antinodes, and the bubble coalescence phenomena. Experiments involving small numbers of bubbles (less than ten) are used to test the basic predictions of the model. These results support subsequent studies of the clustering and coalescence of swarms of bubbles.

1.2 Bubble Transport

There are a few fundamental differences in using acoustic processing techniques when dealing with bubbles as opposed to solid particles or liquid droplets. These issues will be explored at greater length in subsequent chapters, but they warrant a brief introduction.

The first issue is possible shape distortion caused by the acoustic field (which may also be encountered in experiments with liquid drops). Performing the experiments with spherical bubbles is most desirable because it allows for the least sophisticated analytical models. Pressures induced by acoustic fields can distort bubbles from a spherical shape. Therefore knowledge of this practical limit on acoustic field intensity is important from an analytical perspective.

The large density difference between the gas bubbles and the surrounding fluid, in this case water, results in changes in the key equations defining the system. The acoustic contrast factor, a term that is seen in the primary acoustic force equation and which determines the migration to pressure nodes or pressure antinodes, becomes dependent on bubble radius and the wavenumber of the acoustic field as well as densities and speeds of sound. This dependence on radius and wavenumber does not show up for the case of solid particles and liquid droplets. The secondary acoustic force also differs from that of solid particles and liquid droplets in that it is dependent on the monopole resonance frequencies of the bubbles, and must take into account how different those values are compared to the angular driving frequency of the acoustic field.

Another issue that arises is obtaining accurate visual documentation of experiments. Because the micron to millimeter sized bubbles move so quickly, often

with initial velocities ranging between 30 m/s and more than 200 m/s depending on the energy density, it is difficult to monitor their movement, clustering, and coalescence. Under typical conditions, it rarely takes more than a few hundredths of a second for a bubble to reach its approximate equilibrium position, though it may make small adjustments to obtain its actually equilibrium position that can be measured on a more lengthy time scale.

1.3 Microgravity

In ground based studies, density differences between bubbles and liquids can make phase separation relatively easy. But in microgravity environments more expensive and complex systems must be used. Current techniques for gas-liquid separations in microgravity include static separators, which can be prone to fouling; vortex separators, which are not suited for low flow; and rotary separators, which tend to be mechanically complex and expensive.

This research provides preliminary information to address the specific need of removing bubbles from closed loop flow systems in microgravity, possibly space station, applications without incurring the cost or equipment failure of current techniques. In the future it is desirable to conduct studies in environments with induced microgravity to determine the true value of this research under the desired conditions.

1.4 Roadmap to this Dissertation

In this document chapter two describes basic acoustic theory, covering ultrasonic waves, ultrasonic standing waves, and the primary and secondary acoustic forces acting on a compressible sphere. Chapter two also discusses previous work done in the area of ultrasonic phase separation and how ultrasonics has been used in a variety of other areas. Chapter three begins with calculations concerning the deformation of the bubble, building on work previously done Marston [43, 44]. It continues with the determination of the primary force balance and subsequent solving for the position and velocity of a single bubble using previously defined ratios and values [5] to facilitate the ease of managing these equations. This force balance was different from previous work in that there were two equations determined, one for the bubble release case, and one for the bubble capture case. The next major section of chapter three discusses inter-bubble forces with much of the analysis resulting in the equations used in determining the inter-bubble forces advancing work done by Zhang and Davis [52], who didn't consider acoustic forces. Primary forces and bubble-bubble interaction forces have been considered separately by other groups, often only in microgravity environments, whereas this work endeavors to consider all of these interacting together: primary acoustic force, buoyancy force, secondary acoustic force, van der Waals force, and Brownian diffusion. Chapter three continues on with the development of a new mathematical model which determines the relative trajectory of a bubble pair. Though this has been done previously for solid particle and droplets, the case of bubbles is a new endeavor and involves more convoluted relationships between parameters due to new equations resulting from calculations for bubbles. Chapter three closes with examples of relative bubble

trajectories as well as iso-time contours and volume cleared analyses. Chapter four covers experimental procedures and results which covers new issues arising from the use of bubbles not seen in previous research from this group, and chapter five rounds things out with conclusions and suggestions for future work. A flow chart of the basic steps taken in this research can be seen in Figure 1.

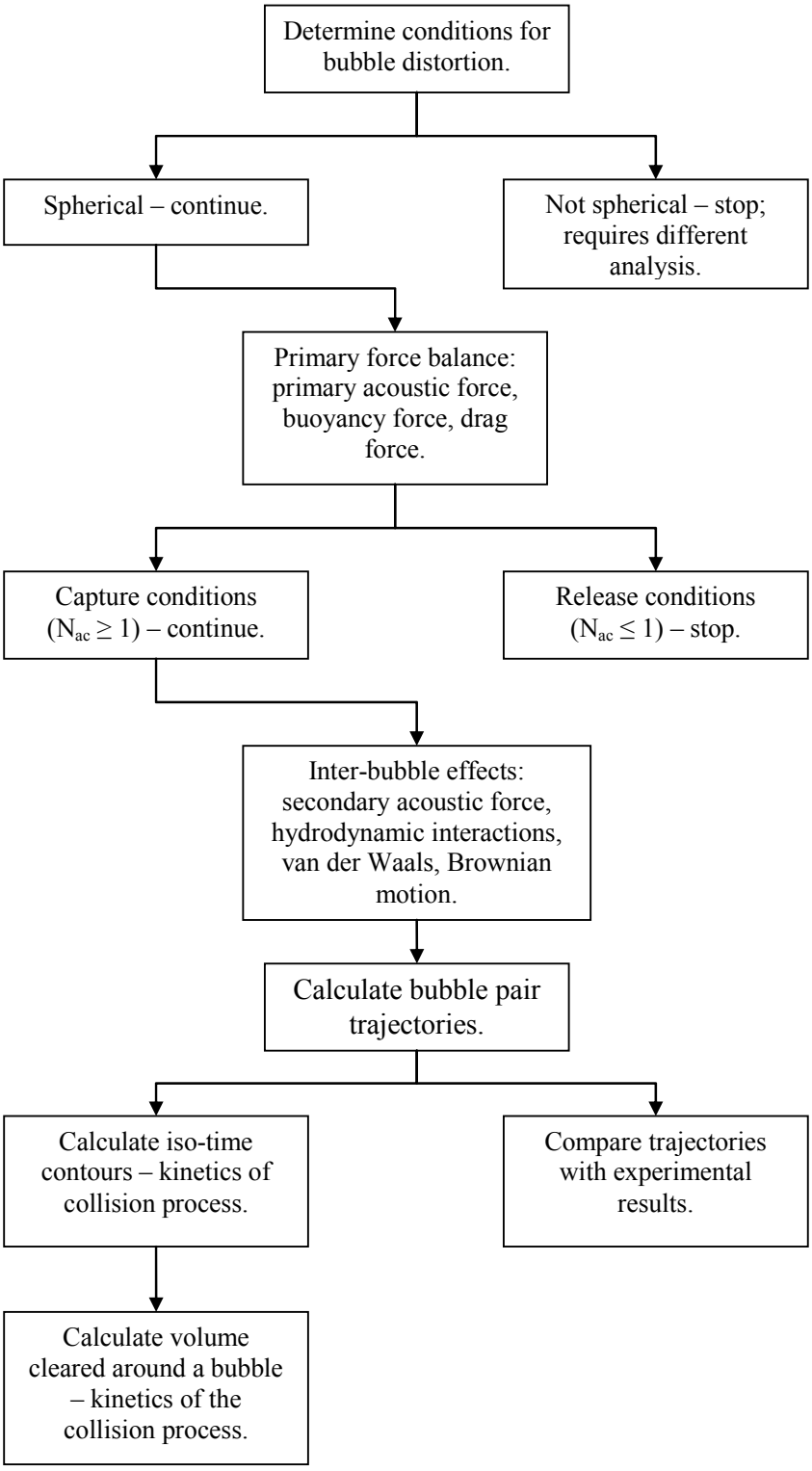

Figure 1: Flow chart of the steps taken to obtain the mathematical and experimental data for this dissertation.

2 Acoustic Force and Literature Survey

The initial definition of sound was anything that could be heard. In other words, the vibrations of air in the frequency range detectible by the human ear. The broader and more scientific definition includes vibrations that travel through all types of matter (gases, liquids, solids, and plasmas) which may or may not be perceivable by the human ear (infrasound and ultrasound). Sound is generated when a medium is dynamically disturbed. A source causes a disturbance in the fluid elements in the surrounding medium; those particles cause a disturbance in the fluid elements surrounding them, and so on. In this way sound energy is transferred through the medium. In fluids, the sound waves are considered longitudinal, i.e. the fluid elements travel in the same direction as the propagation of the sound wave and the disturbance of the medium affects its pressure, density, particle velocity, and temperature. The relationships between these variables determine the wave equation [1, 2, 3, 4].

2.1 Wave Equation

To simplify the derivation of the wave equation, a very small element of volume will be considered. The total pressure of the system consists of the hydrostatic pressure (P_h) and the sound pressure (P_u). Because the hydrostatic pressure is assumed to be constant the derivative of the total pressure is equal to the derivative of the sound pressure [1, 2].

For a small volume of an inviscid fluid, dV, where the pressure on the right side is greater than the left side by $dP = -\left(\frac{\partial P}{\partial x}\right)dx$ there will be a net force to the left, $-\left(\frac{\partial P}{\partial x}\right)dx$, over a unit area. Then using Newton's second law, this force can be shown to accelerate the mass of liquid according to equation (2.1), where ξ_x is the one dimensional displacement of the fluid molecules (assumed to be small). Since the medium is assumed continuous, equation (2.2) can be shown to be true, where V_0 is the initial volume. The equation of state relating the acoustic pressure to the volume change can be used to determine the differential change in pressure, equation (2.3), where γ is the compressibility.

$$-\left(\frac{\partial P}{\partial x}\right)dx = \rho\left(\frac{\partial^2 \xi_x}{\partial t^2}\right)dx \tag{2.1}$$

$$dV = V_0\left(\frac{d\xi_x}{\partial x}\right) \tag{2.2}$$

$$P = -\frac{1}{\gamma}\left(\frac{dV}{V_0}\right) \tag{2.3}$$

Combining equations (2.2) and (2.3) the equation relating the pressure to the displacement is seen in equation (2.4). Using partial differentiation, equations (2.1) and (2.4) can be combined and the relationship in equations (2.5) and (2.6) is found, where c is the speed of sound.

$$P = -\frac{1}{\gamma}\left(\frac{\partial \xi}{\partial x}\right) \tag{2.4}$$

$$\left(\frac{\partial^2 P}{\partial t^2}\right) = c^2\left(\frac{\partial^2 P}{\partial x^2}\right) \tag{2.5}$$

$$\left(\frac{\partial^2 \xi_x}{\partial t^2}\right) = c^2 \left(\frac{\partial^2 \xi}{\partial x^2}\right) \tag{2.6}$$

Assuming simple harmonic motion (equating to the boundary condition of the transducer, which is an oscillating plate with a sinusoidal motion, on one side and the boundary condition of a fixed reflective wall at on the other side), the general solution for equations (2.5) and (2.6) can be written as the sum of two progressive waves moving in opposite directions.

$$P(x,t) = Ae^{-i(\omega t - \kappa x)} + Be^{i(\omega t - \kappa x)} \tag{2.7}$$

For equation (2.7) $i = \sqrt{-1}$, $\omega = 2\pi f$ is the angular frequency, f is the driving frequency of the transducer, $\kappa = \frac{\omega}{c}$ is the wave number and A and B are the maximum amplitudes of the forward and reverse propagating waves, respectively [5]. When $A = B$ this is the solution for a standing wave. If there is no reverse propagating wave, $B = 0$, then equation (2.7) simplifies to equation (2.8). The real form can be expressed as equation (2.9), where φ is the initial phase angle of the pressure wave. If you assume the phase angle is zero (indicating no initial offset in the displacement from a specified reference point) then equation (2.9) can be reduced to equation (2.10) where the spatial and time dependencies are decoupled.

$$P(x,t) = Ae^{i(\omega t - \kappa x)} \tag{2.8}$$

$$P(x,t) = A\cos(\omega t - \kappa x + \varphi) \tag{2.9}$$

$$P(x,t) = A\cos(\kappa x)\cos(\omega t) \tag{2.10}$$

The velocity of the small-volume packet of fluid or gas can be obtained directly from the acoustic pressure. Noting that for simple harmonic motion $\frac{\partial}{\partial t} = i\omega$, the

relationship in equation (2.11) is obtained [29]. Then utilizing equations (2.1) and (2.11), equation (2.12) is acquired.

$$\left(\frac{d^2\xi}{dt^2}\right) = i\omega\left(\frac{\partial\xi}{\partial t}\right) = i\omega v \tag{2.11}$$

$$v(x,t) = -\frac{1}{i\omega\rho}\frac{\partial P(x,t)}{\partial x} \tag{2.12}$$

2.2 Standing Wave Equation

For purposes of this research, the standing wave solution must be utilized because the sound wave is being reflected to introduce a standing sound wave. A standing wave occurs when either the medium is moving in the opposite direction as the wave, or as in this case, when there is interference between two waves of equal wavelength traveling in opposite directions in a stationary medium. With standing waves there is no net propagation of energy. The general solution for the standing wave equation can be seen in equations (2.13) and (2.14), with the velocity equation being the same as that seen in equation (2.12).

$$P(x,t) = Ae^{-i(\omega t-\kappa x)} + Ae^{i(\omega t-\kappa x)} \tag{2.13}$$

$$P(x,t) = 2A\cos(\kappa x)\cos(\omega t) \tag{2.14}$$

The interference of the two plane waves causes a series of parallel displacement nodal planes (minimum displacement) and antinodal planes (maximum displacement). The nodal planes occur at half wavelength intervals with the antinodal planes lying equidistant between them. Displacement and pressure are related in the sense that at points of maximum displacement, there is a minimum pressure variation. At points of

minimum displacement, there is a maximum pressure variation. Figure 2 shows a schematic of this. For the purposes of this dissertation any further references to nodes and antinodes will be indicative of pressure nodes and antinodes, not displacement.

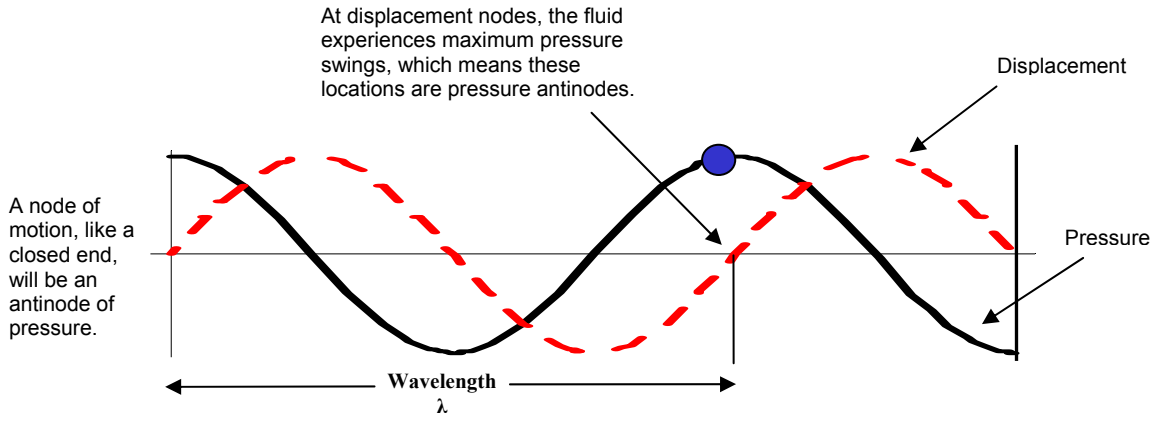

Figure 2: Diagram showing the relationship between pressure and displacement nodes and antinodes. The circle indicates approximate position of bubble collection.

2.3 Acoustic Radiation Force

The forces that act on individual particles, liquid drops, or bubbles interacting only with their processing medium, and not with neighboring particles, liquid drops, or bubbles is known as the primary acoustic force (F_{ac}). Primary acoustic forces tend to induce the migration to specific locations within the suspension [6]. Yosioka and Kawasima calculated the acoustic radiation pressure on a compressible sphere resulting in a primary acoustic force equation for plane stationary waves with uniform amplitude, (2.15) [7, 8].

$$F_{ac} = 4\pi a^3 \kappa E_{ac} F \sin(2\kappa y) \tag{2.15}$$

In equation (2.15) a is the radius, E_{ac} is the average energy density of the acoustic field, y is the distance from the nearest pressure antinode, and F is the acoustic contrast factor. Assuming no secondary interactions, the tendency of a solid drop, liquid drop, or bubble to respond to a resonant standing ultrasonic filed is dependent on the acoustic contrast factor. The acoustic contrast factor for solid particles and liquid drops is different from that of bubbles, but in both cases density and compressibility (or speed of sound) are the important factors. This can be seen in Figure 3. If the acoustic contrast factor is greater than zero, which is the case when the particle is denser than the surrounding fluid, the particle moves to the pressure nodes. If the acoustic contrast factor is less than zero, which is the case when the particle (usually a gas bubble) is less dense than the surrounding fluid, the particle moves to the pressure antinode. This is because the pressure nodes are points of zero pressure variation around ambient, and dense particles have a minimum compressibility so they will move to these areas. Pressure antinodes are areas of maximum pressure variation around ambient, and the less dense bubbles have a larger compressibility so they will move to these areas. This is shown in Figure 4. The particles, droplets, or bubbles move to either the pressure nodes or antinodes because this minimizes the energy of the system. For instance, at pressure antinodes where the pressure swings are the greatest, it takes less energy to compress a bubble than it does to compress a packet of liquid the same size, therefore the bubbles collect at that location. Whereas when particles are being suspended, it takes less energy to compress a packet of liquid than it does a solid particle, so the particles move toward the pressure nodes because they are the points of zero pressure variation.

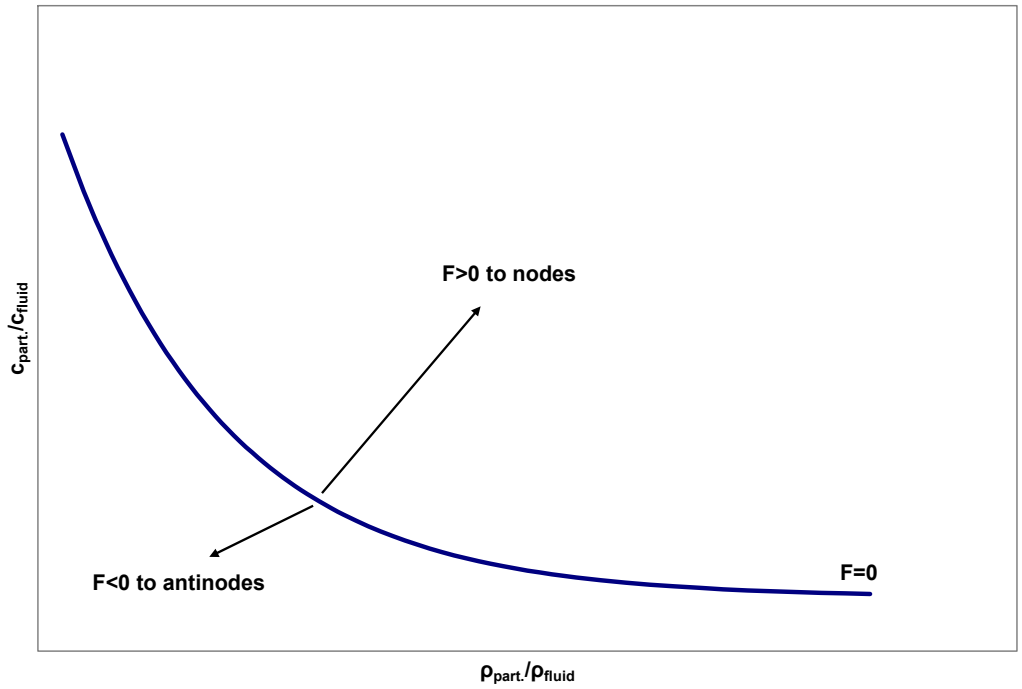

Figure 3: Graph showing the dependence of a particle or liquid drop on density and speed of sound, where F is the acoustic contrast factor. For a bubble there is also a dependence on size.

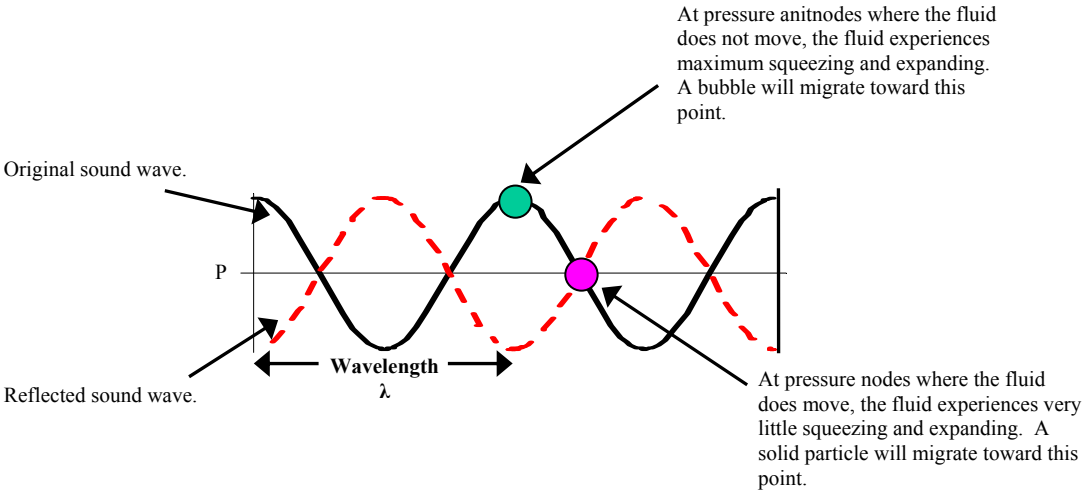

Figure 4: Diagram showing the points at which bubbles (pressure antinodes) and particles (pressure nodes) collect.

The acoustic contrast factor for particles and liquid drops is based solely on density and compressibility, equation (2.16) [7, 8]. For gas bubbles it is also dependent on the radius and frequency, equation (2.17) [7, 8, 9, 10]. This radius and frequency dependency results from the monopole oscillations of the bubble (the breathing mode), which can result in not only a volume change for the bubble but also a resonance frequency variation. Eller developed an expression for the sinusoidal pressure variation [9, 79], but this did not include the effects of radiation damping like the equation obtained by Lee and Wang [9, 10], and like the more general equation obtained by Crum and Prosperetti [9, 78].

$$F = \frac{1}{3}\left[\frac{5\rho_p - 2\rho_l}{2\rho_p + \rho_l} - \frac{\gamma_p}{\gamma_l}\right] = \frac{\hat{\rho} + \frac{2}{3}(\hat{\rho} - 1)}{(1 + 2\hat{\rho})} - \frac{1}{3\hat{\sigma}^2\hat{\rho}} \tag{2.16}$$

$$F = \frac{\left(\frac{1}{\hat{\sigma}^2}\right)\left(3\hat{\rho} - \left(\frac{\kappa a}{\hat{\sigma}}\right)^2\right)}{\hat{\sigma}^2\left(\frac{\kappa a}{\hat{\sigma}}\right)^6 + \left(3\hat{\rho} - \left(\frac{\kappa a}{\hat{\sigma}}\right)^2\right)^2} \tag{2.17}$$

For equations (2.16) and (2.17) ρ_p, c_p, and γ_p are the density of, speed of sound through, and compressibility of the particle; ρ_g and c_g are the density of and speed of sound through the gas bubble; ρ_l, c_l, and γ_l are the density of, speed of sound through, and compressibility of the surrounding liquid; $\hat{\rho} = \frac{\rho_g}{\rho_l} = \frac{\rho_p}{\rho_l}$, and $\hat{\sigma} = \frac{c_g}{c_l} = \frac{c_p}{c_l}$.

Often the assumption of a uniform force is made when in reality there is an arbitrary acoustic field. In other words the assumption of uniform energy density in the system does not always hold. For the case of a standing wave field of non-uniform oscillation-velocity amplitude, the lateral (or transverse) component of the primary

acoustic force may need to be considered, equation (2.18) [11, 12, 13], as well as the axial component which is represented in equation (2.15). This lateral component, which is a primary acoustic force acting perpendicular to the one seen in equation (2.15), most often results from non-uniformities in the transducer.

$$F_{yz} = \frac{4}{3}\pi a^3 \nabla E_{ac}(G_\rho \cos^2[\kappa x] - G_\beta \sin^2[\kappa x]) \tag{2.18}$$

For the lateral component, ∇ is the gradient operator in the lateral (y, z) directions and G_ρ and G_β are the density and compressibility acoustic contrast factors, respectively, defined in equations (2.19) and (2.20).

$$G_\rho = \frac{3(\rho_p - \rho_l)}{\rho_l + 2\rho_p} \tag{2.19}$$

$$G_\beta = 1 - \frac{1}{\hat{\sigma}^2 \hat{\rho}} \tag{2.20}$$

Because the lateral force scales with the gradients of E_{ac}, and the axial force scales directly with E_{ac}, the lateral force is often at least an order of magnitude less than the axial force [12, 13]. The lateral force can cause the particles or bubbles to aggregate to local maxima of E_{ac} once the axial force has induced movement to the pressure nodes or antinodes [5]. These local E_{ac} maxima are often referred to as "hot spots".

2.4 Secondary Acoustic Force

As particles, drops, or bubbles approach each other, secondary forces come into play. These forces dictate how the objects will move toward each other and can possibly help with the understanding of clustering and coalescence. The secondary acoustic force is a time-averaged mutual interaction force of two objects in an acoustically driven liquid.

Once again, the equation used for the case of bubbles, (2.21) [14-18], differs from that used for particles or drops, (2.22) [18, 19]. For the bubble case ω is the angular driving frequency, ω_j is the monopole resonance frequency of a bubble, r is the center to center bubble separation distance, and P_s is the pressure amplitude of the unmodulated standing acoustic wave. For the particle case V_{p1} and V_{p2} are the volumes associated with each particle.

$$F_{ac,2} = \frac{2\pi |P_s|^2 \omega a_1 a_2}{\rho_l r(\omega_1^2 - \omega^2)(\omega_2^2 - \omega^2)} \tag{2.21}$$

$$F_{ac,2} = \frac{\kappa^2 E_{ac}}{2\pi}\left(1 - \frac{\gamma_{p1}}{\gamma_l}\right)\left(1 - \frac{\gamma_{p2}}{\gamma_l}\right)\frac{V_{p2}V_{p1}}{L} \tag{2.22}$$

2.5 Literature Survey

The study of acoustics probably had its beginning with Pythagoras of Samos in the 6th Century BC. His interest in music and his desire to make it more harmonious and less chaotic lead to a series of experiments on the properties of vibrating strings [20, 21]. Though modern acoustics was detailed in the 1877 work *The Theory of Sound* by Lord Rayleigh [22], experiments on high frequency waves did not emerge until the 19th century during World War I. Paul Langevin, a French physicist, used Pierre and Jacques Curie's piezoelectric effect to detect submarines through echo location, though this technology was not operational until after the war [20, 23].

The origins of research on the acoustics of a suspended particle began in 1934 with Louis King who developed the mathematics showing that the time-averaged acoustic radiation pressure on a particle is different than that of the time-averaged

acoustic radiation pressure experienced by the fluid near the particle [24, 25]. Though King's paper didn't account for the compressibility of the spheres, Yoshioka and Kawasima extended the analysis to do so, showing that the density of the spheres compared to that of the surrounding fluid affects whether they move toward pressure nodes or antinodes depending on the sign of the acoustic contrast factor, with less dense spheres moving to the antinodes and more dense spheres moving to the nodes [7].

2.5.1 Ultrasonic Phase Separation – Particles and Droplets

The past two decades have seen a rise in interest in the use of ultrasonics for phase separation processes. Though often times in industry ultrasonics may not be the only technique used for the separation process, it does assist in more convention separation techniques by improving the efficiency and capacity of these presently used separation methods [26]. In the early 1990s research was conducted showing that particles ranging in size from 0.1 to 100 μm in an aqueous suspension could be trapped at nodal zones with half wavelength spacing. Particles of 9 μm were shown to be stable against a continuous flow rate of 5 ml/min (in a cylindrical chamber with a diameter of 2.5 cm and a length of 20 cm) giving a capture efficiency of 80-98%. Removal of particles was accomplished without the aid of fluid flow by repeatedly sweeping the driving frequency over a known range and period, essentially marching the particles to an exist port at one end of the acoustic chamber [27, 28, 29].

Subsequent research focused on fractionation and removal techniques, showing that suspensions could be separated based on particle size or density and compressibility. One method was to utilize thin stream splitters to divide the flow into two product

streams. Particles that responded quickly to the acoustic field moved to one stream, while those that did not moved to the other [31-34].

Another suspension method investigated involved the use of porous mesh. This research utilized a variety of porous mesh, the main types being: unconsolidated beds formed from glass spheres, aluminum foam mesh, and polyester foam mesh. The first two have acoustic impedances an order of magnitude larger than that of the surrounding liquid water, whereas the last has an acoustic impedance much closer to that of the water. All three had pore sizes two to three orders of magnitude larger than that of the particles being collected. Feed suspensions of polystyrene particles (radius 2-30 μm) in deionized water with Triton X were fed through the mesh in the acoustic chamber at rates from 30-60 cm^3/min with particle loadings as high as 1%, and the mesh Single-pass filtration efficiencies from this technique were shown to be as high as 80-90% when using the polyester foam mesh. Numerical results from the modeling associated with this method indicate that the capture of the particles in the mesh is due to the interaction of the incident plane waves with waves reflected from the fiber, also known as secondary acoustic forces [35, 36, 37].

Though much of the research in the field of ultrasonic separations has been conducted with solid particles, in the last few years more investigation has been done on liquid drops in immiscible host liquids. Experiments were done both with and without porous mesh residing in the acoustic chamber. It was shown that the drops residing in a standing acoustic wave field could be induced to coalesce, resulting in a single-pass oil retention efficiency greater than 80% for droplets ranging from 1-15 μm. The filtration efficiency was found to be strongly dependent on both emulsion flow rate and path

length, which implies sensitivity with respect to residence time. Modeling was done to determine the path of droplets being attracted to one another and the time it took for collision and subsequent coalescence [38-41].

2.5.2 Ultrasonic Phase Separation – Bubbles

Although analyzing the effects of acoustic fields on bubbles may seem to be somewhat similar to that for compressible liquid spheres, the possibility of the larger density difference between the gas bubbles and the surrounding liquid and the resonance frequency of the gas bubble can result in a few intrinsic differences. Take, for instance, both the primary and secondary acoustic forces. While the majority of the primary acoustic force equation remains the same, the acoustic contrast factor for with gas bubbles, equation (2.17), is also sensitive to the bubble radius and the frequency at which the system is being driven as well as the density and speed of sound through each fluid [9, 10]. Neither of these effects is significant for liquid droplets. The resonance frequency of the bubble can also affect the location of the bubble within the acoustic chamber. It has been shown that if a bubble is larger than resonance size, or to put it another way if a bubble is being driven above its resonance frequency, it will move to the pressure antinodes in the system. Whereas a bubble smaller than resonance size, or a bubble being driven below its resonance frequency, will move toward the pressure nodes [59, 60, 61]. Khabeev looked at the resonance properties of a soluble gas bubble. He found that at high frequency the behavior of a soluble bubble is the same as that of an insoluble bubble because diffusion is a very slow process relative to the rates of bubble vibration and will only manifest itself at very low frequencies [83].

The secondary acoustic force must also take into account the resonance frequency of the bubbles being considered [14, 47]. The resonance frequency of a bubble is dependent on the radius of that bubble, the density of the surrounding fluid, the pressure inside the bubble, and the polytropic exponent of the gas inside the bubble. It is well recognized that the secondary acoustic force can change signs based on the comparison between the resonance frequency of the bubbles and the driving frequency of the acoustic chamber. Classical Bjerknes theory indicates that two interacting bubbles will repel each other, assuming the driving frequency is between the natural frequency of the two bubbles ($\omega_i<\omega<\omega_j$), otherwise a mutual attraction occurs which should result in coalescence [62]. There have been a variety of papers in the last 10-15 years that refute the simplicity of this theory based on the specific conditions used in the study [65, 66, 67, 68, 75].

In 1944 while doing research on destructive cavitation, Kornfeld and Suvorov observed an attractive force acting between two bubbles, sometimes resulting in coalescence and, when there was a large enough size discrepancy, small bubbles were seen to orbit the larger bubbles in an elliptical pattern. In other instances the bubbles were seen to repel each other [64]. The cases of coalescence and repulsion are, of course another example of the classical Bjerknes theory that indicates the acoustic force is attractive when the bubbles are oscillating in phase with each other and repulsive when the bubbles are oscillating in opposite phase [17]. The orbiting phenomenon is not something commonly investigated, though more recently Barbat and Ashgirz have attempted to explain it [73, 74]. They found that whether bubbles at small separations collide, orbit, or scatter is dependent on the kinetic energy of the pair. It was also found

that the 2-D motion of a non-resonant pair of bubbles changes pattern from hyperbolic trajectories to elliptical orbits and elliptical collision trajectories as the forcing amplitude increases, regardless of the bubble size ratio [74]. Resonant bubble pairs could either move in a pattern of closed orbital trajectories (much like the pictures you drew as a child with a spiral drawing set) or they could move in a pattern of precessing orbits [74]. Harkin *et al.* showed that the pattern of motion for a bubble pair can be dramatically affected by the strength of the acoustic forcing and that the bubble pairs can move in directions opposite of what is predicted from classical and even enhanced Bjerknes theory [77].

Another factor determining whether the secondary acoustic force is attractive or repulsive is the spacing between the bubbles [49, 67, 69, 70]. Doinikov and Zavatrak showed that at small distances, the value of the mutual interaction force varies substantially from that of the classic theory [67, 75]. Zabolotskaya showed that as the bubbles approach each other their resonance frequencies increase, which may cause sign reversals in the secondary acoustic force [65]. Zheng and Apfel showed that the magnitude and direction of the interparticle force depends on the relative orientation of the centerline of the two objects to the traveling direction of the primary plane incident wave [49]. The sign of the secondary acoustic force changes when the center to center distance increases by half a wavelength [49].

Ida has recently suggested that bubbles can invert their own pulsations phases around frequencies other than their resonance frequencies. These are referred to as transition frequencies and are usually defined as the driving frequency at which the phase difference between a bubble's frequency (not necessarily the resonance frequency) and

the external frequency is $\pi/2$ [48, 63]. Assuming negligible damping effects, for an N bubble system there are 2N-1 transition frequencies and only N of those correspond to the resonance frequencies. The claim was made that the sign reversal on the secondary acoustic force takes place at the transition frequencies as well as at the resonance frequencies [48]. So now not only is there a sign reversal in the force for the case of $\omega_i<\omega<\omega_j$, there is an indication that a sign reversal also occurs for $\omega>\omega_i>\omega_j$ [17]. Doinikov showed that for two bubbles with resonance frequencies greater than the driving frequency ($\omega_i>\omega_j>\omega$) there is a mutually attractive force; for the case where one bubble is smaller than resonance size and one bubble is larger ($\omega_i<\omega<\omega_j$) the force may initially be repulsive but at small distances that repulsion changes to attraction; and for the case where both bubbles are larger than resonance size there are two different possibilities depending on the size of the bubbles: coalescence or initial attraction changing to repulsion at small separations [67, 75]. In later papers Doinikov showed that when considering the second harmonic component of the interaction force, small bubbles being driven either above ($\omega>\omega_i>\omega_j$) or below ($\omega_i>\omega_j>\omega$) their resonance frequency can experience a secondary acoustic force which, at small distances, can either cause them to repel each other or form a bound pair with some stable separation [14, 71, 72]. Mettin et al. also showed that as bubbles approach each other the secondary acoustic force can change from attractive to repulsive, and in some cases results in a stable separation distance [76]. This stable separation distance can result in the cluster formation of what is called “bubble grapes” for larger bubbles and “acoustic streamers” for smaller bubbles.

Most of the cases talked about previously are based off of an assumption of an incompressible, non-viscous liquid as the suspending phase. But when adding in the

possibility of viscous effects, the response of bubbles can veer from classical Bjerknes theory once again. The fluid viscosity breaks the conservation of the system of two interacting bubbles, and the interaction force felt by one bubble is no longer equal and opposite to that felt by the second bubble [16]. The secondary acoustic force undergoes dissipative effects in response to losses in the linear pulsations of the bubbles and the acoustic streaming around the bubbles due to the viscosity of the host liquid [65, 81]. Doinikov showed that when very small bubbles (1-20 μm) are driven far below resonance, viscous effects can result in a repulsive interaction force. He conjectured that the vertical motion and acoustic streaming that develops around a bubble can lead to viscous drag forces on the other bubble, reducing or completely negating the attractive force that classical Bjerknes theory predicts [15]. Hitt and Prosperetti considered these viscous forces as they apply to the primary acoustic force. They showed that the viscous drag forces consist of two components. The first is a linear "Stokes-like" drag and the second is a "Basset-like" term that has its physical origin in the interaction of the bubble motion with its own viscous wake. It was determined that these viscous forces had little impact on the bubble motion and final resting point (primary acoustic force) [78, 82]. Devin showed that not only are viscous forces important when determining the resonance frequency of bubbles, but that thermal damping, due to the thermal conduction between the gas in the bubble and the surrounding liquid, and radiation damping, due to the radiation of spherical sound waves, are also important [84].

When considering a bubble in a microgravity environment, the primary force balance becomes a bit easier because the buoyancy and gravitational effects can be neglected. In boiling experiments run under microgravity conditions, Sitter *et al.* showed

that bubbles larger than resonance size moved toward the pressure nodes, and bubbles smaller than resonance size moved toward the pressure antinodes. They also showed that acoustic standing waves can increase the heat transfer rates, especially when the heating element is paced at an acoustic pressure antinode, and that an acoustic standing wave can play the role of the buoyancy force under microgravity conditions [85]. Abe et al. also showed that bubbles larger than resonance size moved toward the pressure nodes, but their final resting point would be slightly above the node. They determined that under reduced gravity the maximum size of bubbles that could be controlled was larger than in normal gravity due to reduced buoyancy effects, and that the bubbles tended to line up horizontally at the same height in reduced gravity, as opposed to agglomerating as seen in normal gravity [86]. Although Hawkes *et al.* didn't do experiments with bubbles in microgravity under the influence of a standing acoustic field, they did investigate particles and determined that there was a more efficient movement of the bands in microgravity than in normal gravity due to the lack of sedimentation. Their observations suggested that the chamber-scale streaming which disrupts the ordered state of smaller particles at normal gravity is driven by temperature gradients rather than acoustic streaming [87].

Surfactants reduce the surface tension of the gas-liquid interface of air bubbles in water. In an acoustic system without a surfactant, there is a greater tendency for bubbles to coalesce because this reduces the surface area and thus reduces the surface energy of the system. When adding a surfactant the surface tension at the gas-liquid interface decreases. It has been shown that the adsorption of the surfactant onto the interface retards the process of bubble coalescence [88]. Crum as well as Ashokkumar *et al.*

determined that a surfactant can increase the growth of small bubbles due to rectified diffusion [89, 90, 101], which is when acoustic energy causes supersaturated gas to be pumped into an existing small bubble, making the bubble increase in size [131]. Asaki and Marston showed that the soluble surfactant Triton X-100 can decrease the size of larger bubbles by enhancing the rate of gas transfer from the bubble to the water [91]. Those authors noted that at low surfactant concentrations the frequency and damping of the bubble exhibit maxima, whereas at high concentrations of surfactant the bubble frequency is reduced, due to surface tension depression, and the damping is further increased. They also point out that not all surfactants can be expected to affect gas transfer rates in the same manner [91] and identify previous experiments with the insoluble surfactant stearic acid which show neutrality toward gas transfer [92]. Sunartio *et al.* measured the bubble volume at different frequencies and concentrations of the surface active solute sodium dodecyl sulfate (SDS) and determined that a lower number of SDS molecules adsorb onto the gas-liquid interface at higher frequencies. This was indicated by a reduced inhibition to coalescence which, they say, equates to a reduction in the steric repulsion of the bubbles [88]. Giribabu and Gosh looked at the effect of two different nonionic surfactants at the gas liquid interface without the addition of acoustics. They showed that between the two, Tween 20 and Triton X-100, Triton X-100 is better at stabilizing bubbles or, in other words, preventing coalescence [93]. Malysa *et al.* discuss the velocity of bubbles with the presence of a variety of different surface active substances, again without the addition of acoustics [94]. They used Frumkin and Levich's adsorption theory to explain the lower velocity of bubbles in surfactant solutions: the molecules of surfactant adsorbed at the top of the bubble are convected by

the surface flow to the bottom where they accumulate and then desorb. This results in surface tension gradients that retard the mobility of the bubble interface thus lowering the bubble terminal velocity [94, 95, 96]. Malysa et al. determined that the minimum adsorption coverage needed to immobilize a bubble surface was less than 10% in the majority of cases of surface active substances studied [94].

Part of the research involving acoustic effects on gas bubbles and their behavior is often times in regard to the cavitation and sonoluminescence phenomena. Cavitation occurs when vapor bubbles or cavities are formed in a liquid when the pressure of the liquid has been reduced to below its vapor pressure [97]. Vapor gases evaporate into the cavities from the surrounding liquid and the low pressure inside the cavitation bubbles will cause the bubbles to begin to collapse due to the higher pressure of the surrounding fluid. The temperature and pressure of the vapor in the bubbles will continue to increase as the bubble volume decreases, and eventually the bubbles will collapse, at which point the gas within the bubbles dissipates into the surrounding fluid in a violent mechanism, see Figure 5, which releases a significant amount of energy in the form of an acoustic shock-wave and sometimes visible light, also referred to as sonoluminescence [98], see Figure 6. Though for sonoluminescence to occur the bubble must contain mainly inert noble gas such as argon [98]. Specifically for an acoustic field, microscopic gas bubbles already present in the liquid will be forced to oscillate, and if the acoustic field intensity is sufficiently high the bubbles will grow in size and then rapidly collapse [98].

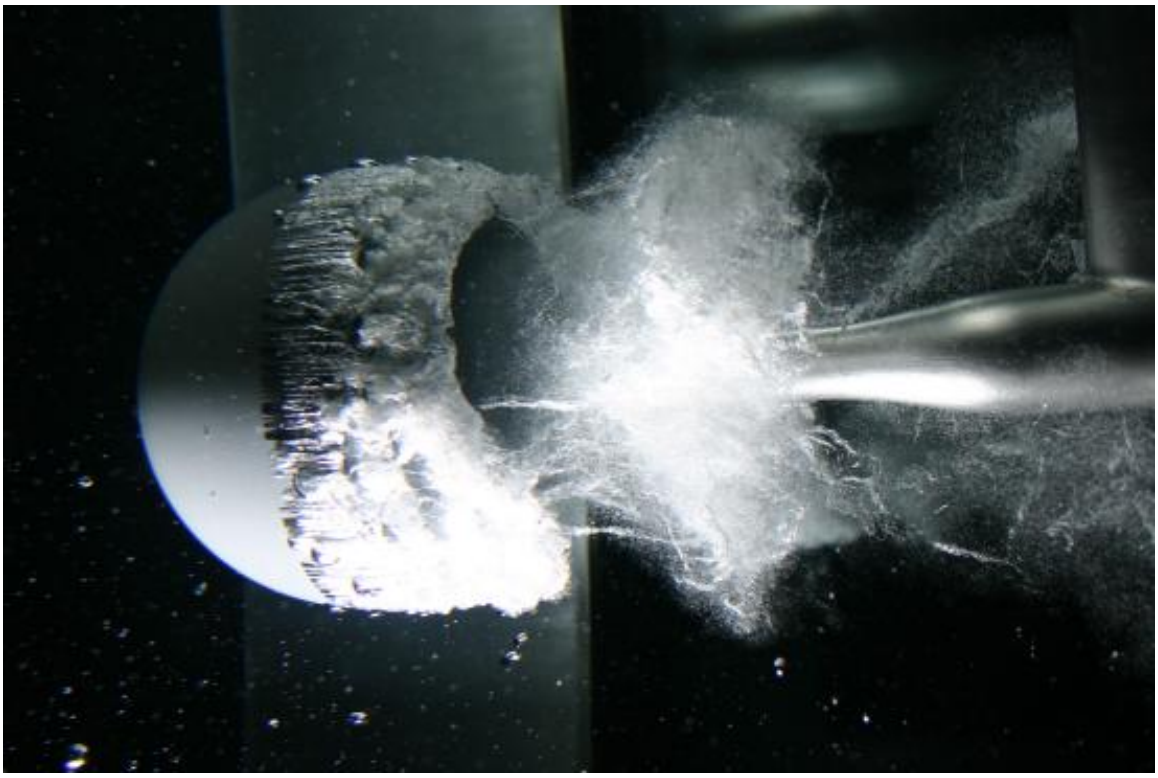

Figure 5: Picture of a cavitation bubble erupting [99]. The size of the bubble was not indicated in the reference.

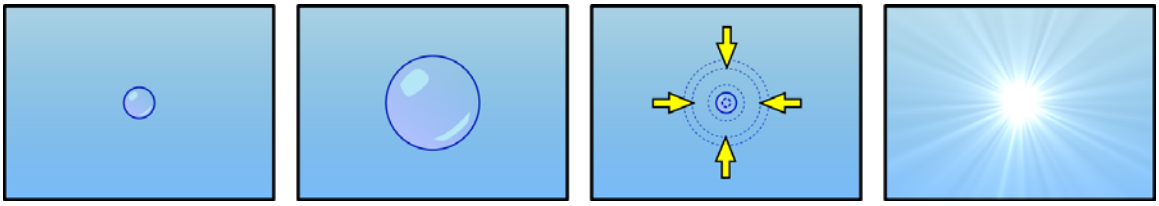

Figure 6: 1) Apparition of bubble, 2) quick expansion, 3) sudden contraction (very short compared to expansion), 4) light produced by the high pressure and high temperatures inside the small bubble [102].

Lauterborn *et al.* showed that free oscillations of a cavitation bubble can be initiated by a focused laser light and forced oscillations by a standing acoustic field. The nonlinear free oscillations are strongly damped by the radiation shock waves upon collapse for the case of the focused laser light. This is also true for a bubble in an

acoustic field, but in this case the energy lost is resupplied by the sound field. It was determined that upon collapse, the resultant light flash scales with the maximum bubble radius, and not with the volume which is proportional to the energy in the bubble [104]. Akhatov *et al.* showed that cavitation bubbles can form acoustic streamers. Negating secondary acoustic forces yields a stable structure, and when adding in the secondary forces the structure becomes more branched and less stable [103]. Lauterborn *et al.* also reported on the filament structure of cavitation bubbles, commenting that when looking at the pattern with the naked eye, the structure seems dense and the dendritic branched structure is pronounced, Figure 7, but when short exposure pictures are taken the structure is much more diluted, Figure 8 [104].

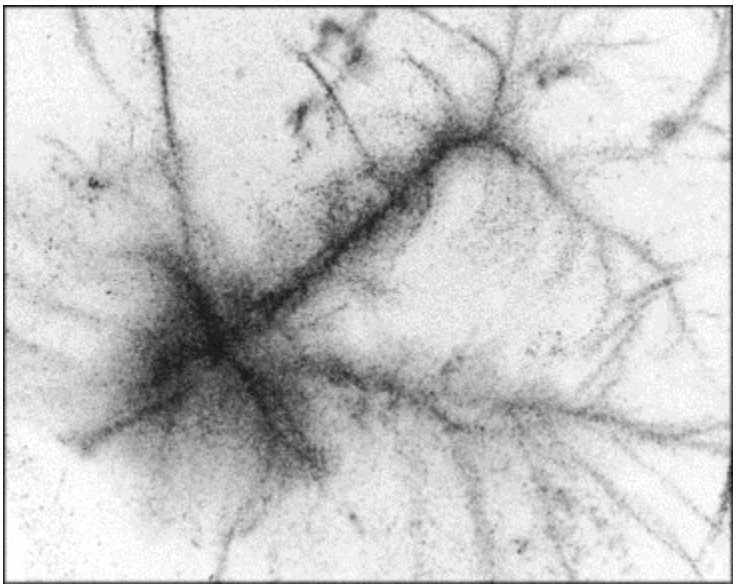

Figure 7: Bubble web in a standing acoustic wave called acoustic Lichtenberg figure, single pressure antinode region, long exposure (several periods of the sound field) [104]. Size of the structure was not provided in the reference.

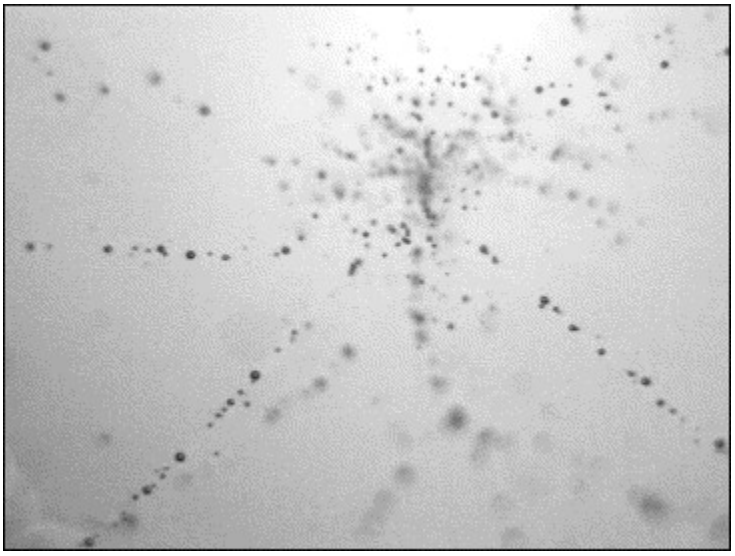

Figure 8: Bubble web in a standing acoustic wave called acoustic Lichtenberg figure, single pressure antinode region, short exposure (approximately 10 ns) [104]. Size of the structure or the bubbles was not provided in the reference.

Hatanaka *et al.* showed that by increasing the voltage supplied to the transducer, larger clusters of bubbles form. The clusters consist of a few large bubbles surrounded by a swarm of small bubbles and they repeatedly coalesce and fragment. This can affect multibubble sonoluminescence (MBSL) because as bubbles cluster, secondary acoustic forces increase and the cluster may begin to move away from the pressure antinode where sonoluminescence occurs [105]. Posakony et al. investigated the use of a second transducer, oriented 90º from the first one, to stabilize a 3-D MBSL bubble pattern [106]. Maisonhaute et al. showed that isonation at 500 kHz can increase the base current of an electrochemical system (0.5 M solution of $Fe(CN)_6^{3-}$) utilizing a 25 μm diameter microelectrode due to an increased flux resulting from acoustic streaming. The occurrence of cavitation in the induced a reduction current indicating that part of the diffusion layer had been removed by the cavitation activity [107].

Though not considered cavitation, another form of bubble breakup is referred to as fragmentation. Leighton showed that in an acoustic field, one bubble approaching another is enough to disturb the sound field and prevent the stationary bubble from oscillating stably. The subsequent violent shape oscillations of the bubble may cause it to break apart into smaller bubbles which disperse rapidly into the surrounding fluid [100]. The acoustic field can also cause gas to be lost from one bubble by generating smaller daughter bubbles due to surface waves on the mother bubble wall. Secondary Bjerknes forces can cause these smaller bubbles to be transferred to a neighbor bubble in a stream to coalesce with the larger bubble. The initial mother bubble is relatively unaffected by this type of fragmentation, unlike the previous example of neighbor-induced fragmentation [100].

There has also been research done on bubble interactions with drops and particles in acoustic fields. Doinikov reports that as a heavy drop, a drop with a density larger than the surrounding fluid, and a bubble approach each other the interaction force changes from positive to negative forming a stable bound structure that remains as long as the sound field remains on. For a light drop, a drop with a density less than the surrounding fluid, he showed that the interaction force changes from repulsion to attraction at very short separations [108]. Doinikov and Zavtrak looked at the mutual interaction force between a particle and bubble in a sound field. For heavy particles, it was shown that the interaction force changed from attraction to repulsion if the driving frequency is slightly above some of the natural frequencies of shape oscillations of the bubble. For light particles it was shown that the interaction force changed from repulsion to attraction at all frequencies [109]. For both heavy particles and light drops it was

observed that a second sign change on the interaction force as a function of separation could occur. For the particle, this means that the force can change from attractive to repulsive to attractive again and vice versa for the drop [108, 109]. These examples considered the secondary acoustic force only, and neglected the primary forces. Gould *et al.* investigated effect of cavitation bubbles on the capture of 9 μm polystyrene spheres. Their results showed that high enough levels of cavitation were disruptive to the captured particles but that the aggregated particles could tolerate some bubble activity. This tolerance was due to the separation of the particle and the bubbles given that the particles were located at the pressure nodes and the bubbles were located at the pressure antinodes[110]. Ata and Jameson observed that in the presence of floatable solids bubble clusters would form held together by silica particle bridges using dodecylamine as a collector, though this was without the benefit of an acoustic field [111].

2.5.3 Other Applications

Ultrasound for use in medical applications initiated with its application in therapy as opposed to diagnosis, and ultrasound-induced tissue heating began to be used in the 1930s and 1940s [112]. Langevin was probably the first to associate ulstrasound to the biological and medical world in 1917 when he noted the ultrasonic destruction of schools of fish in the sea [20, 112]. In the 1940s, William Fry and Russel Meyers used ultrasound to destroy parts of the basal ganglia in patients with Parkinsonism and Peter Lindstrom reported ablation of frontal lobe tissue in moribund patients to alleviate their pain from carcinomatosis [20]. In the late 1940s and early 1950s groups in the United States and Japan began research on the use of ultrasound for medical imaging [20].

Howry showed that tissue interfaces could be detected with ultrasound and Wild showed that cancer tissue structures could be differentiated from benign tissue structures [112, 113-115].

Ter Haar and Wyard found that blood cells exposed to an acoustic standing wave band at half wavelength intervals in the blood vessels [116]. Weiser *et al.* determined that when a large number of cells react to their interparticle forces, the cells lined up perpendicular to the primary acoustic force will experience an attractive force whereas the cells lined up parallel will experience a repulsive force [117]. Zhou et al. investigated the use of ultrasound to enhance a fiber-optic *Salmonella* biosensor. They found that the *Salmonella* cells could be captured by a standing acoustic wave, but the best fluorescence signal intensities were achieved by immobilizing the *Salmonella* antibody on polystyrene microspheres before subjecting the sample to the acoustic field. Acoustic focusing resulted in an eight-fold increase in the peak value of the fluorescence spectrum [118]. Sedimentation ultrasonic filters have been used in biomedical separations. The ultrasonic standing wave is positioned across the outflow of the fermentor so that as the soluble cell product is drawn away, the cells clump and sediment back into the culture to produce more antibodies [119]. This technique has shown a yeast recovery with an efficiency of 99% and an *E. coli* recovery of 82% [120]. Batch systems can also separate cells with a decent efficiency, with whole blood and E. coli separation in excess of 99.5% [34, 121].

Ultrasound has found a wide-spread use in the field of medical imaging, and though traditional medical sonography is common, another technique called contrast-enhanced ultrasound (CEUS) is also being used. In this technique, ultrasound contrast agents, which are gas-filled microbubbles, are used to increase the ultrasonic signal.

Microbubbles have a large ability to reflect ultrasonic waves, also called echogenicity, and the echogenicity difference between the gas in the microbubbles and that of the surrounding tissue is considerable. The microbubble contrast agent enhances the ultrasonic backscatter, and thus allows for a sonogram with increased contrast [122]. This technique was first discovered by Dr. Charles Joiner in the late 1960s. When performing an M-mode echocardiogram he noticed an increase in ultrasonic signal after each injection of indocyanine, which was later found to be a result of small bubbles forming at the catheter tip [123].

There are a variety of other uses for ultrasound. Kim *et al.* used the acoustic emission technique to monitor the crevice corrosion on 304L austenitic stainless steel and found that this technique was in good agreement with both corrosion potential and visual observations [124]. Birkin *et al.* showed that cavitation bubbles can enhance mass transfer, which is associated with forced convection resulting from the bubble collapse [125]. Marmottant and Hilgenfeldt investigated the use of acoustic streaming, resulting from microbubbles in an ultrasonic field, for an alternative means of directional transport in microfluidics, instead of the typical method of transporting small objects through channels by actuation forces such as applied pressure differences or thermocapillary forces [126]. Similarly, Liu *et al.* looked at bubble induced micromixing for use in microfluidics. They found that microbubbles in an acoustic field generated steady circulatory flows and reduced the mixing time for a 22 μl solution from hours (pure diffusion based mixing) to tens of seconds [127]. Pandy *et al.* showed that the use of ultrasound when chemically etching particle tracks into plastic solid state nuclear track detectors can reduce the etching time, result in more conical shaped particle tracks and

better clarity, reduce the surface damage, result in more homogenous etching, and allow for better control of the conditions which results in greater reproducibility [128]. Jyoti and Pandit looked at using ultrasonic cavitation with chemicals such as ozone and hydrogen peroxide for use in water disinfection. Though they found that this increases the cost, ultrasonic cavitation can help decrease the toxic by-product formation, and can reduce the heterotropic plate count bacteria as well as the total coliforms, fecal coliforms, and fecal streptococci (indicators of pollution in drinking water) by as much as 99% when hydrogen peroxide (5 mg/L) shows a maximum reduction of only 28% [129]. Laschimke *et al.* used advanced acoustic emission analysis to show that the tension in the water conducting system of vascular plants is caused by countless minute gas bubbles strongly adhering to the hydrophobic lignin domains of the xylem vessel walls [130]. It is their statement that the transport of the non-metabolic energy from the leaves to the roots, resulting from the cohesive attraction between the bubbles, is the most important precondition of the long-distance water transport in plants [130]. All of this goes to show that the uses of ultrasound are many and pervasive in modern technology.

3 Theory and Equations

The initial analytical portion of this research project aimed to develop a fundamental understanding of the effect of buoyancy versus acoustic forces on the entrapment and coalescence phenomena. Modeling efforts illustrate the relationship between the size of bubbles, their sphericity, acoustic field parameters (frequency and intensity), bubble placement in regards to acoustic pressure antinodes, and the bubble coalescence phenomena.

3.1 Analysis of Bubble Sphericity

Performing experiments with spherical bubbles is most desirable because it allows for the least cumbersome analytical models while still retaining the essential physics of the problem. It also allows modeling results to be checked fairly easily against experimental results. Pressures induced by acoustic fields can distort bubbles from a spherical shape. Therefore knowledge of this practical limit on acoustic field intensity is important. Bubble sphericity was determined based on work by Marston [43, 44], in which he used linear and inviscid theory to approximate the quadrupole projection of the acoustic radiation pressure on a compressible sphere of millimeter size. This can be seen in equation (3.1).

$$P_{20} = \tfrac{1}{2} P_s^2 \gamma_l (5\pi)^{\frac{1}{2}} \left\{ \begin{array}{l} \dfrac{6\sin^2(\kappa y)}{5}\left(d_{1,2}^2 + (\kappa a)^2 \left[\dfrac{d_{1,2}}{5} + \dfrac{\hat{\rho}^2}{d_2^2}\left(1 - \dfrac{1}{\hat{\rho}\hat{\sigma}^2} \right) \right] \right) + \\ \dfrac{2(\kappa a)^2 \cos^2(\kappa y)}{3d_3}\left(\dfrac{5d_{1,3}(2+d_3)}{21} + \hat{\rho} - \dfrac{(2+\hat{\rho})}{3\hat{\rho}\hat{\sigma}^2} \right) + O(\kappa a)^4 \end{array} \right\} \qquad (3.1)$$

In equation (3.1), P_{20} is the static portion of the component of radial projection which is mainly responsible for the deformation. Also, γ_l is the compressibility of the continuous medium (in this case water), κ is the wavenumber, y is the distance of the center of the bubble from a pressure antinode, a is the radius of a sphere that is the same volume as the bubble, and $\hat{\rho} = \frac{\rho_g}{\rho_l}$, $\hat{\sigma} = \frac{c_g}{c_l}$, $d_1 = \hat{\rho} - 1$, $d_2 = 1 + 2\hat{\rho}$, $d_3 = 2 + 3\hat{\rho}$, $d_{1,j} = \frac{d_1}{d_j}$, where ρ_l and c_l are the density and speed of sound through the continuous phase and ρ_g and c_g are the density and speed of sound through the dispersed bubble phase. P_s is the pressure amplitude of the unmodulated standing acoustic wave and is given by $P_s = \sqrt{2\rho_l c_l^2 E_{ac}}$, where E_{ac} is the average energy density of the acoustic field.

By using values for the radial projection of the acoustic stress tensor obtained from equation (3.1) and the surface tension for an air/water interface (73.05 dynes/cm), the shape of the bubble can be determined using equations (3.2) and (3.3) [43, 44].

$$a_{ar}(\theta_d) = a + x(\theta_d) \tag{3.2}$$

$$x(\theta_d) = \left(\frac{5}{16\pi}\right)^{\frac{1}{2}} (3\cos^2(\theta_d) - 1)\left(\frac{a^2}{4\sigma_i}\right) P_{20} \tag{3.3}$$

For these equations σ_i is the interfacial tension between the bubble and the water and θ_d is the polar angle of a point on the drop surface with respect to the vertical axis. From equations (3.2) and (3.3) the maximum bubble radius, corresponding to an angle of 90º, and the minimum bubble radius, corresponding to an angle of 180º, are determined. For the purpose of this study a bubble is assumed spherical provided that its maximum aspect ratio (r_{max}/r_{min}) is no greater than 1.1, the assumption of a spherical bubble can be used.

By fixing the aspect ratio, a variety of parameters can be varied. One of which is the energy density in the fluid within the acoustic chamber. Figure 9 shows a graphical representation of this. For example, a bubble with a 100 μm radius and a frequency of 0.435 MHz, the maximum average energy density that allowed the sphericity criterion to be satisfied was determined to be 0.649 J/m^3. Basically, what Figure 9 shows is a force balance between the primary acoustic force and the surface tension force (actual surface tension remains constant; the force does not). As the energy density increases, the primary acoustic force increases and to keep the two forces balanced, the surface tension force also has to increase. The lowest energy shape for the bubble is spherical, but as the surface tension force increases the bubble is distorted from sphericity. Also, the farther the bubble is from the acoustic pressure antinode, the larger the bubble can be and still allow the spherical assumption to hold.

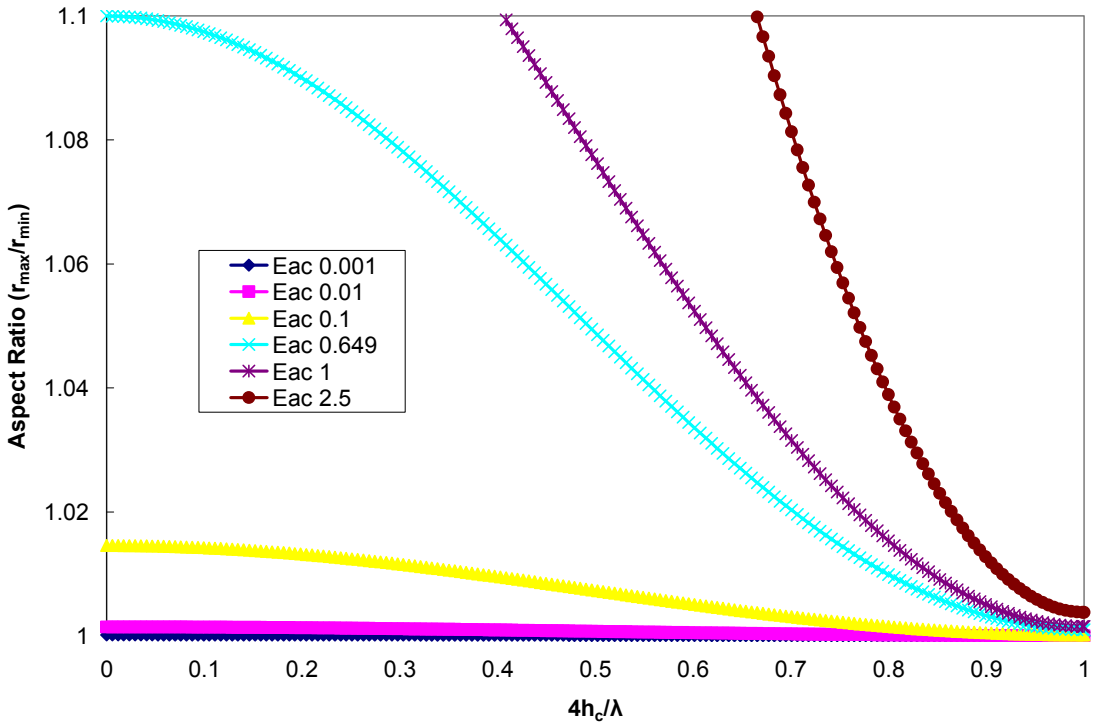

Figure 9: Graph of aspect ratio for varying energy densities in J/m^3 for a bubble with a radius of 100 µm.

3.2 Analysis of Bubble Entrapment

The physical effects referred to as body forces determine whether bubble entrapment will occur. The body forces consist of gravity, buoyancy, drag, and the primary acoustic force. Assuming the bubbles are widely spaced and there are no bubble-bubble interactions, these are the forces which determine not only the likelihood of bubble entrapment, but the position and velocity of the bubble as well. Though some of these equations were presented in previous chapters, they will be revisited here for the sake of continuity. The primary acoustic force is given by equation (3.4) [7], and the buoyancy and gravitational forces are given by equation (3.6). The drag force is given by the Hadamard-Rybczynski formula (3.7) [42] which assumes a slip condition at the

boundary (resulting in the 4π), and which reduces to equation (3.8) for the case of an air bubble in water because the term inside the parenthesis is approximately one.

$$F_{1,ac} = 4\pi a^3 \kappa E_{ac} F \sin(2\kappa y) \tag{3.4}$$

$$F = \frac{\frac{1}{\hat{\sigma}^2}[3\hat{\rho} - (\frac{\kappa a}{\hat{\sigma}})^2]}{\hat{\sigma}^2(\frac{\kappa a}{\hat{\sigma}})^6 + [3\hat{\rho} - (\frac{\kappa a}{\hat{\sigma}})^2]^2} \tag{3.5}$$

$$F_b = \tfrac{4}{3}\pi a^3(\rho_l - \rho_g)g \tag{3.6}$$

$$F_d = -4\pi\left(\frac{1+\frac{3\hat{\mu}}{2}}{1+\hat{\mu}}\right)\mu_l a V^0 \tag{3.7}$$

$$F_d = -4\pi\mu_l a V^0 \tag{3.8}$$

In Equations (3.4)-(3.8), κ is the wavenumber, a is the radius of the bubble, E_{ac} is the average energy density in the continuous liquid phase, y is the distance of the bubble from a pressure antinode, F is the acoustic contrast factor defined in equation (3.5) specifically for a gas bubble (F = -28.9 for the air/water system with a bubble of 100 μm radius and a frequency of 0.435 MHz), $\hat{\mu} = \frac{\mu_g}{\mu_l}$, and V^0 is the velocity of the moving bubble. It should be noted that the bubble will move to the acoustic pressure antinode because the acoustic contrast factor is negative. For the equation represented above, equation (3.5), and the previously defined system, the sign on the acoustic contrast factor will always be negative for a varying bubble radius (the limit of F as a approaches infinity is zero). Balancing these forces and solving for V^0 results in equation (3.9). The force balance can then be used to solve for the position and the velocity of the bubble.

$$V^0 = \frac{a^2}{\mu_l}\left(\frac{1}{3}(\rho_l - \rho_g)g + \kappa E_{ac} F \sin(2\kappa y)\right) \tag{3.9}$$

The velocity term, V^0, can be replaced by the derivative, $\frac{dy}{dt}$, and the resulting first order ordinary differential equation can be solved analytically to obtain the bubble position, y, as a function of time. The differentiation of that expression with respect to times gives the velocity due to the body forces as a function of time for a given bubble. These equations were derived for two different circumstances: bubble entrapment and bubble release.

3.2.1 Bubble Release

The capture or release of a bubble is determined by a dimensionless number that is the ratio of the magnitude of the primary acoustic force to the relative gravitational effects, and will be referred to as N_{ac} from now on. When the absolute value of this ratio is one or greater the bubble is captured. Conversely, when the absolute value of this ratio is less than one the bubble is not captured.

Beginning with equation (3.9), the velocity term, V^0, can be replaced by the derivative, $\frac{dy}{dt}$ as seen in equation (3.10). There are two different integrals that can result from this equation. The following derivation is specifically for the case when N_{ac} is less than one.

$$dt = \frac{dy}{\frac{a^2}{\mu_l}\left(\frac{1}{3}(\rho_l - \rho_g)g + \kappa E_{ac} F \sin[2\kappa y]\right)} \tag{3.10}$$

$$\int_0^t dt = \int_{y=y_0}^{y} \frac{dy}{p + q\sin[\alpha y]} = \frac{1}{\alpha\sqrt{p^2 - q^2}} \tan^{-1}\left[\frac{p\tan\left[\frac{1}{2}\alpha y\right] + q}{\sqrt{p^2 - q^2}}\right] \tag{3.11}$$

$$p = \frac{a^2(\rho_l - \rho_g)g}{3\mu_l} \tag{3.12}$$

$$q = \frac{a^2 \kappa E_{ac} F}{3\mu_l} \tag{3.13}$$

$$\alpha = 2\kappa \tag{3.14}$$

Evaluating equation (3.11) using Mathematica, and subsequent solving for y gives equation (3.15) where y_0 is the bubble position at $t = 0$.

$$y = \frac{2}{\alpha}\tan^{-1}\left[\frac{-q + \sqrt{p^2 - q^2}\,\tan\left[\frac{1}{2}\alpha t\sqrt{p^2 - q^2} + \tan^{-1}\left[\frac{q + p\tan\left[\frac{\alpha y_0}{2}\right]}{\sqrt{p^2 - q^2}}\right]\right]}{p}\right] \tag{3.15}$$

To get the velocity due to the body forces as a function of time for a given bubble equation (3.15) is differentiated, giving the rather long equation (3.16).

$$V^0 = \frac{p(p^2 - q^2)}{p^2 + q^2\cos\left[\alpha t\sqrt{p^2 - q^2} + 2\tan^{-1}\left[\frac{q + p\tan\left[\frac{\alpha y_0}{2}\right]}{\sqrt{p^2 - q^2}}\right]\right] - q\sqrt{p^2 - q^2}\,\sin\left[\alpha t\sqrt{p^2 - q^2} + 2\tan^{-1}\left[\frac{q + p\tan\left[\frac{\alpha y_0}{2}\right]}{\sqrt{p^2 - q^2}}\right]\right]} \tag{3.16}$$

After inputting p, q, and α (equations (3.12) - (3.14)) into equations (3.15) and (3.16), they become a bit unwieldy. Three numbers are defined to facilitate manageability of these equations, as well as to provide basic information about the system. The first is a dimensionless number which is the ratio of the magnitude of the primary acoustic force to the relative gravitational effects which was mentioned before, equation (3.17). The second number is the ratio of the gravitational force to the drag force divided by the velocity term, and is the velocity at which the bubble would travel if there was no acoustic force acting on it, equation (3.18). The third is another

dimensionless number and is given in equation (3.19). Equation (3.20) shows a simplification that is used throughout equations (3.15) and (3.16).

$$N_{ac} = \frac{q}{p} = \frac{3\kappa E_{ac} F}{(\rho_l - \rho_g) g} \tag{3.17}$$

$$M = p = \frac{a^2 (\rho_l - \rho_g) g}{3\mu_l} \tag{3.18}$$

$$\Gamma = \kappa M t \sqrt{1 - N_{ac}^2} + \tan^{-1}\left(\frac{N_{ac} + \tan[\kappa y_0]}{\sqrt{1 - N_{ac}^2}} \right) \tag{3.19}$$

$$p^2 - q^2 = p^2 \left(1 - \frac{q^2}{p^2} \right) = p^2 (1 - N_{ac}^2) = M^2 (1 - N_{ac}^2) \tag{3.20}$$

The final reduced equation for the velocity due to the body forces as a function of time for a given bubble is seen in equation (3.21).

$$V^0 = \frac{M(1 - N_{ac}^2)}{1 + N_{ac}^2 \cos[2\Gamma] - N_{ac} \sqrt{1 - N_{ac}^2} \sin[2\Gamma]} \tag{3.21}$$

Using this same reduction method, the position equation can be written as seen in equation (3.22).

$$y = \frac{1}{\kappa} \tan^{-1}\left[-N_{ac} + \sqrt{1 - N_{ac}^2} \tan[\Gamma] \right] \tag{3.22}$$

Figure 10 shows a position versus time graph predicted for the bubble release case, for various initial bubble positions for a bubble with a radius of 100 μm. The energy density for this case is 0.05 J/m^3, which is too low to induce capture. From the primary force balance for a 100 μm bubble it was determined the lowest energy density to result in capture is 0.062 J/m^3 (this is the lowest allowable energy density to result in an $|N_{ac}| \geq 1$). The positions of the pressure antinodes based on half wavelength

calculations are also shown in Figure 10. Figure 11 shows the velocity versus time data for the same conditions.

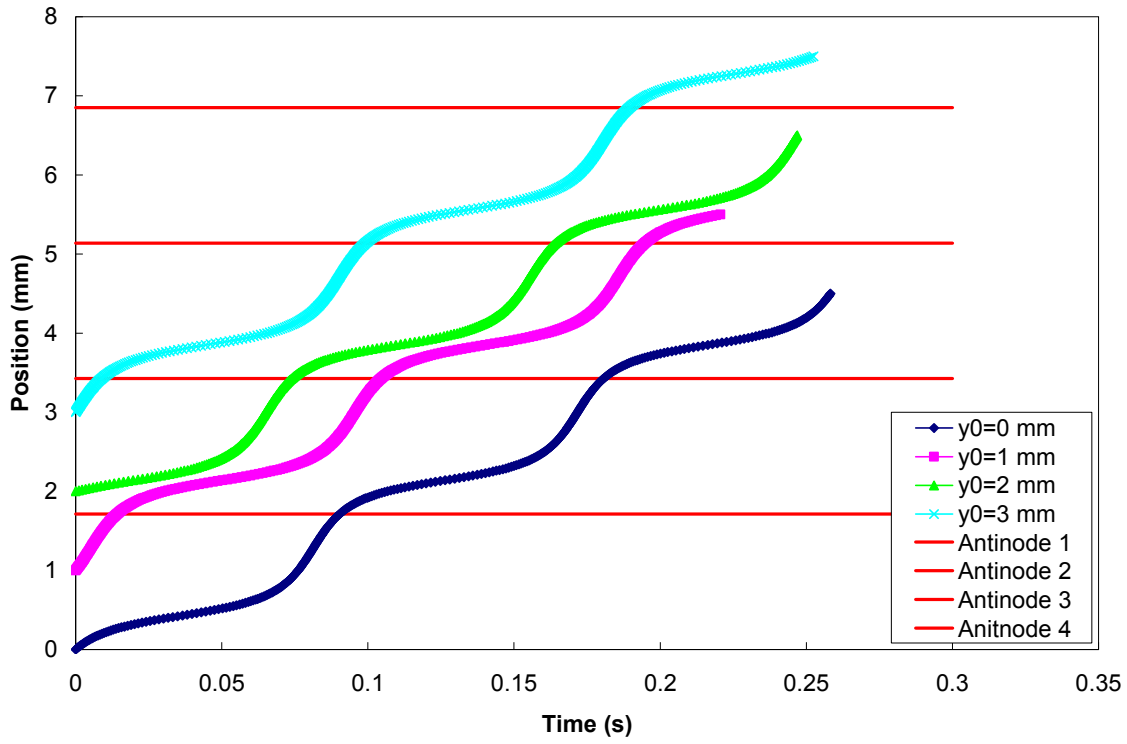

Figure 10: Position versus time graph of bubble for the release case, with varying initial position of the bubble with the transducer at the zero position. Antinode positions are also marked. The bubble radius is 100 µm and Eac is 0.5 J/m^3 and Nac is -0.813.

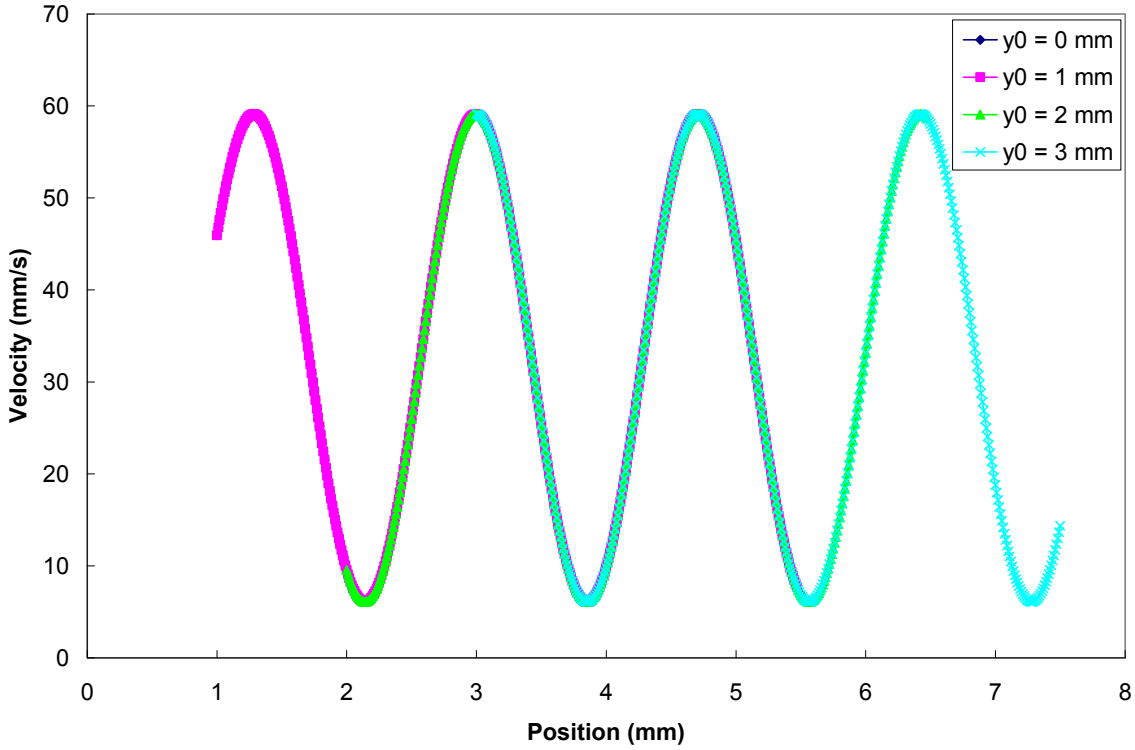

Figure 11: Velocity versus time graph of bubble for the release case, with varying initial position of the bubble with the transducer at the zero position. The bubble radius is 100 µm and Eac is 0.5 J/m^3 and Nac is -0.813.

3.2.2 Bubble Capture

For an air bubble to be captured in water within the acoustic chamber, $|N_{ac}| \geq 1$. The solution to this problem closely follows that of the bubble release example, except the solution to the integral of $\frac{dy}{dt}$ is slightly different, which can be seen in equation (3.23).

$$\int_0^t dt = \int_{y=y_0}^{y} \frac{dy}{p+q\sin[\alpha y]} = \frac{1}{\alpha\sqrt{q^2-p^2}} \ln\left[\frac{p\tan\left[\frac{1}{2}\alpha y\right]+q-\sqrt{q^2-p^2}}{p\tan\left[\frac{1}{2}\alpha y\right]+q+\sqrt{q^2-p^2}}\right] \tag{3.23}$$

Again using Mathematica to solve for y, equation (3.23) becomes equation (3.24) where q, p, and α are as seen in equations (3.12) - (3.14).

$$y = \frac{2}{\alpha}\tan^{-1}\left[\frac{-p(q+p\sin[\alpha y_0])+q\cosh\left[\alpha t\sqrt{q^2-p^2}\right](p+q\sin[\alpha y_0])+\sqrt{q^2-p^2}\,(p+q\sin[\alpha y_0])\sinh\left[\alpha t\sqrt{q^2-p^2}\right]}{q^2+(q^2-p^2)\cos[\alpha y_0]-p^2\cosh\left[\alpha t\sqrt{q^2-p^2}\right]-2pq\sin[\alpha y_0]\sinh\left[\frac{\alpha t}{2}\sqrt{q^2-p^2}\right]^2}\right] \tag{3.24}$$

To get the velocity due to the body forces as a function of time for a given bubble equation (3.24) is differentiated. Because the velocity equation is so long, it has been broken up into three pieces. The numerator is given in equation (3.25). Two parts of the denominator are given in equations (3.26) and (3.27), and the equation using these three pieces is seen in equation (3.28).

$$V_{p1}^0 = 2(p^2-q^2)(p+q\sin[\alpha y_0])\left(\begin{array}{l} p(p+q\sin[\alpha y_0])-\cosh\left[\alpha t\sqrt{q^2-p^2}\right]\left[(q^2-p^2)\cos[\alpha y_0]+q(q+p\sin[\alpha y_0])\right] \\ -\sqrt{q^2-p^2}\,(q+q\cos[\alpha y_0]+p\sin[\alpha y_0])\sinh\left[\alpha t\sqrt{q^2-p^2}\right] \end{array}\right) \tag{3.25}$$

$$V_{p2}^0 = \left(q^2+(q^2-p^2)\cos[\alpha y_0]-p^2\cosh\left[\alpha t\sqrt{q^2-p^2}\right]-2pq\sin[\alpha y_0]\sinh\left[\tfrac{1}{2}\alpha t\sqrt{q^2-p^2}\right]^2\right)^2 \tag{3.26}$$

$$V_{p3}^0 = \left(-p(q+p\sin[\alpha y_0])+q\cosh\left[\alpha t\sqrt{q^2-p^2}\right](p+q\sin[\alpha y_0])+\sqrt{q^2-p^2}\,(p+q\sin[\alpha y_0])\sinh\left[\alpha t\sqrt{q^2-p^2}\right]\right)^2 \tag{3.27}$$

$$V^0 = \frac{V_{p1}^0}{V_{p2}^0\left(1+\dfrac{V_{p3}^0}{V_{p2}^0}\right)} \tag{3.28}$$

Using two of the three dimensionless numbers defined previously, equations (3.17) and (3.18), and a new simplifying term, equation (3.29), the position and velocity equations

can be slightly simplified. The position can be determined from equation (3.30). The velocity can be determined from equation (3.31).

$$\Psi = \alpha t M \sqrt{N_{ac}^2 - 1} = 2\kappa t M \sqrt{N_{ac}^2 - 1} \tag{3.29}$$

$$y = \frac{1}{\kappa} \tan^{-1} \left[\frac{-N_{ac} - \sin[2\kappa y_0] + (1 + N_{ac} \sin[2\kappa y_0])(N_{ac} \cosh[\Psi] + \sqrt{N_{ac}^2 - 1} \sinh[\Psi])}{N_{ac}^2 + (N_{ac}^2 - 1)\cos[2\kappa y_0] - \cosh[\Psi] - 2N_{ac} \sin[2\kappa y_0] \sinh\left[\frac{\Psi}{2}\right]^2} \right] \tag{3.30}$$

$$V^0 = \frac{2M(N_{ac}^2 - 1)(1 + N_{ac}\sin[2\kappa y_0]) \begin{bmatrix} (1 + N_{ac}\sin[2\kappa y_0]) - \cosh[\Psi]\left[(N_{ac} - 1)\cos[2\kappa y_0] + N_{ac}(N_{ac} + \sin[2\kappa y_0])\right] \\ -\sqrt{N_{ac}^2 - 1}(N_{ac} + N_{ac}\cos[2\kappa y_0] + \sin[2\kappa y_0])\sinh[\Psi] \end{bmatrix}}{\left(\begin{bmatrix} N_{ac}^2 + (N_{ac}^2 - 1)\cos[2\kappa y_0] - \cosh[\Psi] - 2N_{ac}\sin[2\kappa y_0]\sinh[\frac{\Psi}{2}]^2 \end{bmatrix}^2 + \left[-N_{ac} - \sin[2\kappa y_0] + (1 + N_{ac}\sin[2\kappa y_0])(N_{ac}\cosh[\Psi] + \sqrt{N_{ac}^2 - 1}\sinh[\Psi]) \right]^2 \right)} \tag{3.31}$$

Figure 12 shows a position versus time graph predicted for the bubble entrapment case, with variable initial bubble positions. The energy density for this case is 0.649 J/m^3, which induces bubble capture fairly quickly. This value was chosen as a result of the bubble sphericity calculations which showed that for a bubble with a 100 μm, 0.649 J/m^3 is the maximum energy density that can be used which still allows for an aspect ration of 1.1 or less, equating to a spherical bubble. Figure 13 shows the velocity versus time graphs for this case. Figure 14 and Figure 15 show the position and velocity versus time for the case of and energy density of 0.062 J/m^3. In both of these instances the transducer is located at the zero position.

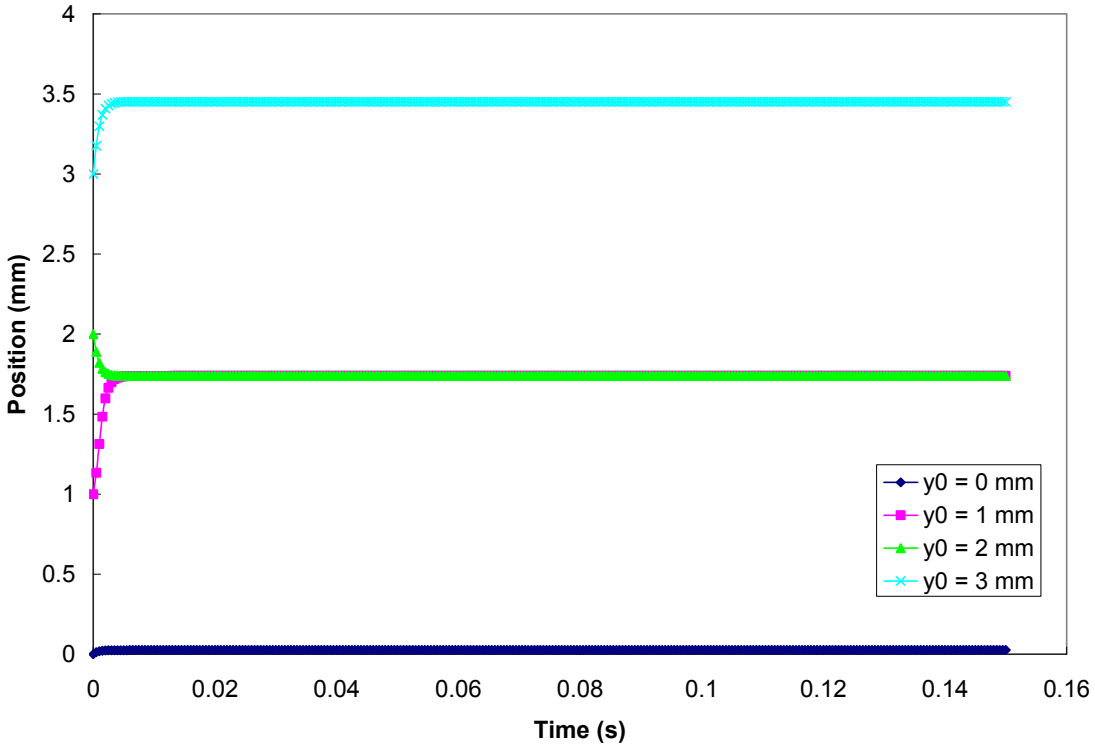

Figure 12: Position versus time graph of a bubble for entrapment case with an energy density of 0.649 J/m^3, with varying initial position of the bubble with the transducer at the zero position. The bubble radius is 100 µm and Nac is -10.557.

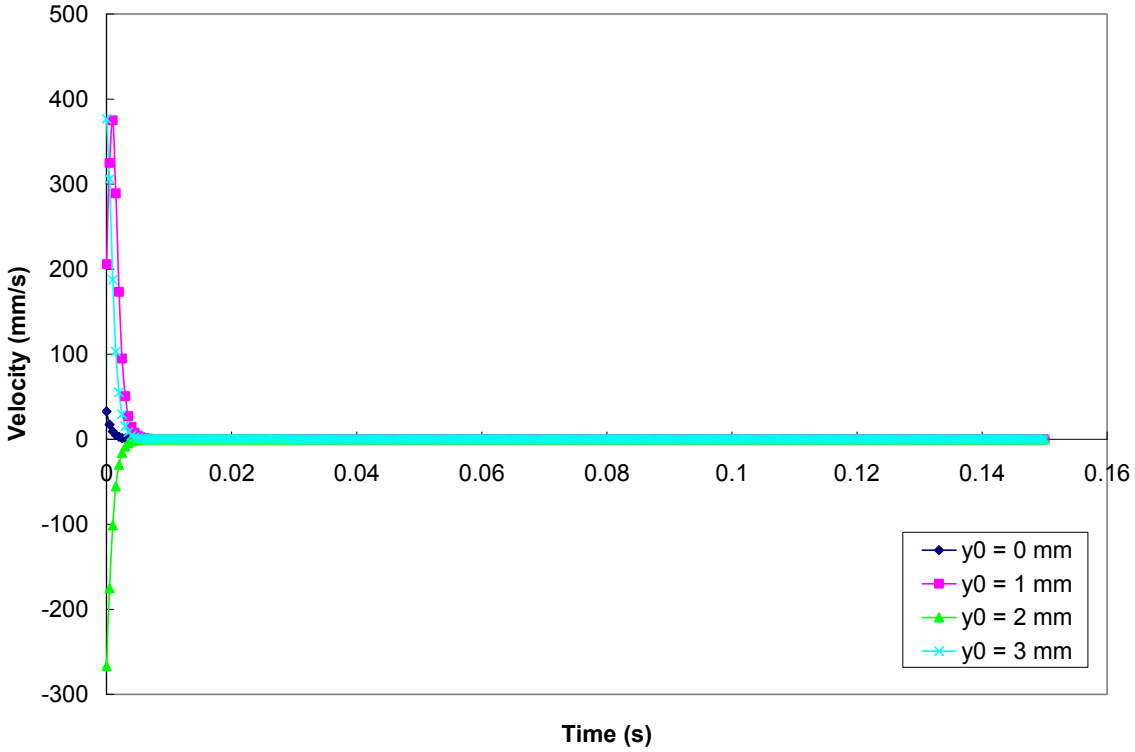

Figure 13: Velocity versus time graph of a bubble for entrapment case with an energy density of 0.649 J/m^3, with varying initial position of the bubble with the transducer at the zero position. The bubble radius is 100 µm and Nac is -10.557.

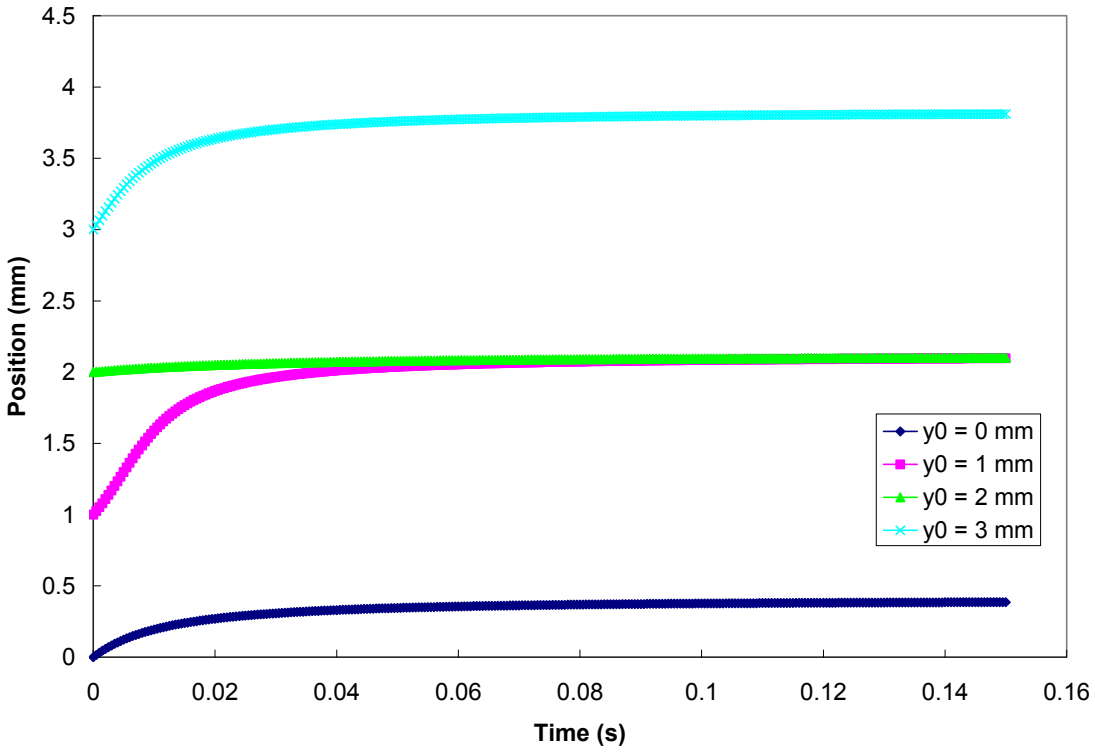

Figure 14: Position versus time graph of a bubble for entrapment case with an energy density of 0.062 J/m^3, with varying initial position of the bubble with the transducer at the zero position. The bubble radius is 100 µm and Nac is -1.008.

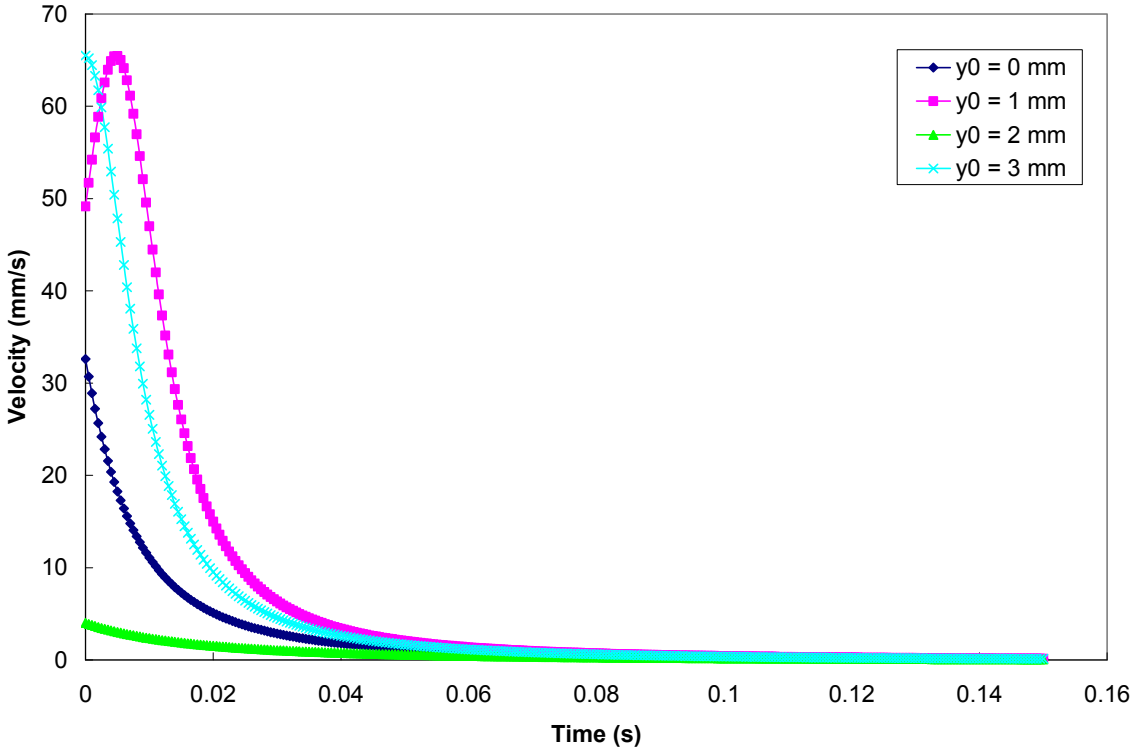

Figure 15: Velocity versus time graph of a bubble for entrapment case with an energy density of 0.062 J/m^3, with varying initial position of the bubble with the transducer at the zero position. The bubble radius is 100 µm and Nac is -1.008.

It can be seen that there is at least an order of magnitude difference in the time it takes a 100 µm bubble to reach its equilibrium position between the maximum energy density case (0.649 J/m^3) and the minimum energy density case (0.062 J/m^3). The distance the bubble rests above the pressure antinode is also affected by the magnitude of the energy density. In Figure 12, where the energy density is 0.649 J/m^3, the bubbles sit approximately 0.03 mm above the antinode, with the bubbles sitting at 0.026 mm, 1.74 mm, and 3.45 mm. From the half wavelength calculations the bubbles should sit at 0 mm, 1.71 mm, and 3.42 mm. In Figure 14, where the energy density is 0.062 J/m^3, the

bubbles sit approximately 0.38 mm above the antinode, with the bubbles sitting at 0.38 mm, 2.09 mm, and 3.8 mm.

Using the primary force balance the minimum energy density needed to capture bubbles of varying radii was calculated. Using the bubble sphericity equations the maximum allowable energy density to still assume sphericity was calculated for bubbles of varying radii. Figure 16 shows this data plotted as two separate curves. The intersecting point was found to be approximately at a bubble radius of 160 μm. This indicates that a bubble with a radius of 160 μm is the largest bubble that can both be captured by the primary acoustic field and can be assumed spherical. Figure 16 shows that a bubble with a radius falling within the shaded area can be assumed spherical and will be captured at an acoustic pressure antinode.

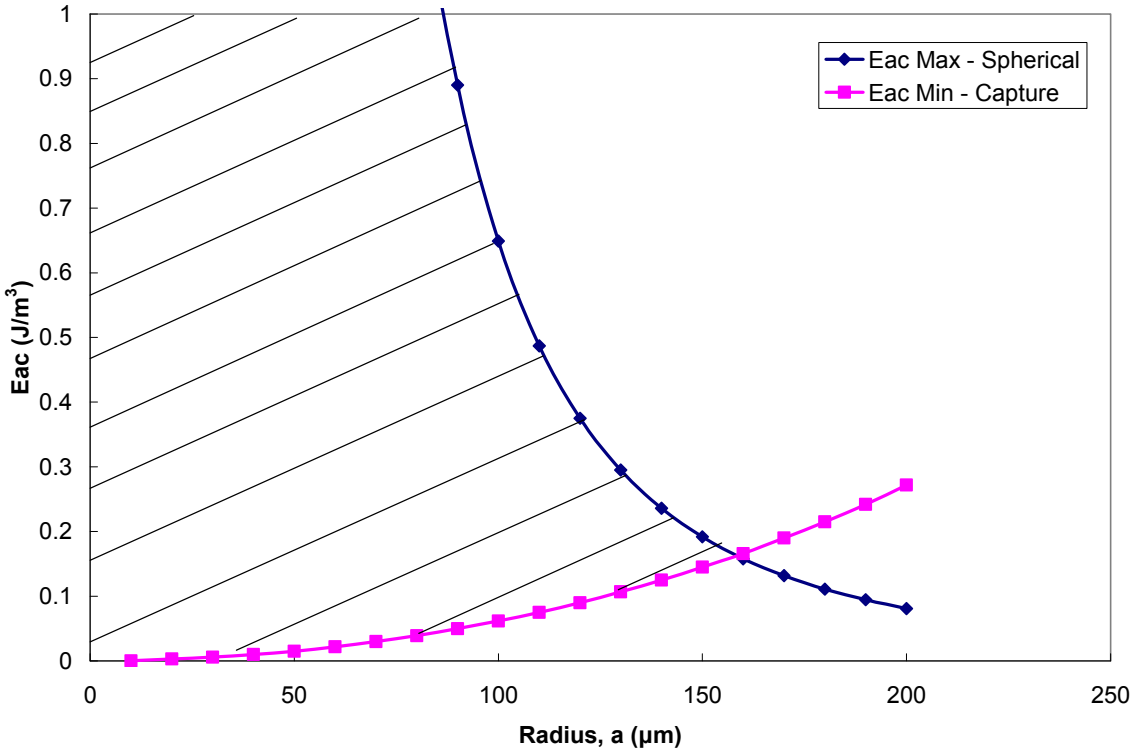

Figure 16: Energy density (J/m^3) versus radius (µm). The bottom curve represents the minimum energy density needed to capture a bubble of the indicated size. The top curve represents the maximum energy density allowed for the spherical bubble assumption to still hold. Any bubble with a radius falling within the shaded area can be assumed spherical and will be captured near a pressure antinode.

3.3 Inter-Bubble Forces

Inter-bubble forces are fundamentally different from primary forces because they are constantly changing as the bubbles approach one another. These inter-bubble forces become more significant as the bubbles get closer, and can induce collision and possibly coalescence during or after bubble migration toward the pressure antinodes.

3.3.1 Secondary Acoustic Force

The secondary acoustic force is also known as the secondary Bjerknes force, and was first studied by V.F.K. Bjerknes and his son C.A. Bjerknes. It is a time-averaged mutual interaction force of two pulsating gas bubbles in an acoustically driven liquid [14]. This force is produced by a secondary ultrasonic wave from an oscillating bubble [45], and the magnitude of this secondary force is often far exceeded in magnitude by the primary acoustic force [67]. The secondary acoustic force for two bubbles can be seen in Equation (3.32) derived by Doinikov to allow numerical evaluation of the interaction force through a cutoff approximation of an infinite series using recurrence formulas for its coefficients [14, 51]. For the secondary acoustic force ω is the angular driving frequency, ω_j is the monopole resonance frequency of a bubble seen in Equation (3.33) [14] with a newer version including an added correction factor for bubbles close to resonance size in Equation (3.34) [47], r is the center to center bubble separation distance, η is polytrophic exponent of the gas (for the case of air, a diatomic gas, 1.4 [46]), and P_{j0} is the equilibrium gas pressure inside the bubble. P_{j0} was derived assuming a spherical bubble with an outside pressure of 1 atm (101,325 Pa) $\left(P_{j0} = \frac{2\sigma_i}{a_{j0}} + P_{atm} \right)$.

Figure 17 shows the secondary acoustic force versus bubble separation distance. In this example, the bubbles are being driven at a frequency above their resonance frequency. From the literature [14, 17, 47-51], this is an indication that the secondary acoustic force will be an attractive force. This can be backed up by the graph which shows that as the bubbles approach each other, the secondary acoustic force increases exponentially.

$$F_{ac,2} = \frac{2\pi |P_s|^2 \omega a_1 a_2}{\rho_l r^2 (\omega_1^2 - \omega^2)(\omega_2^2 - \omega^2)} \tag{3.32}$$

$$\omega_j = \frac{1}{a_{j0}} \left(\frac{3\eta P_{j0}}{\rho_l} - \frac{2\sigma_i}{\rho_l a_{j0}} \right)^{1/2} \tag{3.33}$$

$$\omega_j = \frac{1}{a_{j0}} \left(\frac{3\eta P_{j0}}{\rho_l} - \frac{(3\eta - 1)2\sigma_i}{\rho_l a_{j0}} \right)^{1/2} \tag{3.34}$$

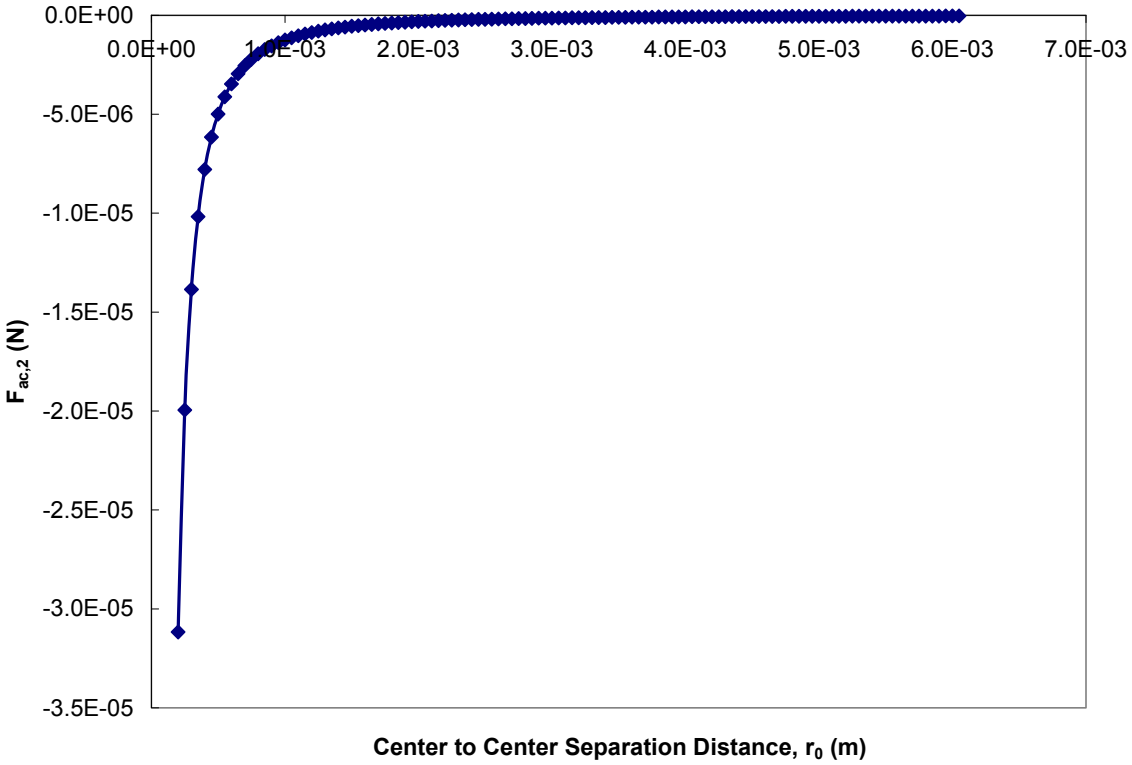

Figure 17: Secondary acoustic force versus center to center bubble separation distance. Both bubble radii are 100 µm and Eac is 0.5 J/m^3.

3.3.2 van der Waals Force

The van der Waals interaction potential energy seen in equation (3.35) [52] also needs to be considered. By taking the derivative of equation (3.35) with respect to bubble separation distance, the actual van der Waals force can be derived, (3.36). Figure 18 shows a graph of the van der Waals force versus the bubble separation distance.

$$V_{vdW} = -\frac{A}{6}\left[\left(\frac{8\hat{a}}{(s^2-4)(1+\hat{a})^2}+\frac{8\hat{a}}{s^2(1+\hat{a})^2-4(1-\hat{a})^2}\right)+\ln\left(\frac{(s^2-4)(1+\hat{a})^2}{s^2(1+\hat{a})^2-4(1-\hat{a})^2}\right)\right] \quad (3.35)$$

$$F_{vdW} = -\frac{4096A\hat{a}^3 s}{3(a_1+a_2)(1+\hat{a})^2(s^2-4)^2(-4(\hat{a}-1)^2+(\hat{a}+1)^2 s^2)^2} \quad (3.36)$$

In equations (3.35) and (3.36) A is the Hamaker constant ($3.7\bullet10^{-20}$ J for two air bubbles separated by water [53]), $s = \frac{2r}{a_1+a_2}$, and $\hat{a} = \frac{a_2}{a_1}$.

To determine the relevance of the van der Waals force in the total inter-bubble effects the relative size of the van der Waals force $\left(\frac{4096A}{3a_1}\right)$ is compared to the value of the secondary acoustic force at the point of collision (s = 2). The approximate value of the relative magnitude of the van der Waals force is $5\bullet10^{-13}$ N for a_1 = 100 μm, and the value of the magnitude of the secondary acoustic force is approximately $3.1\bullet10^{-5}$ N for $a_1 = a_2$ = 100 μm. The eight orders of magnitude difference indicates that the van der Waals force will contribute negligibly compared to the secondary acoustic force.

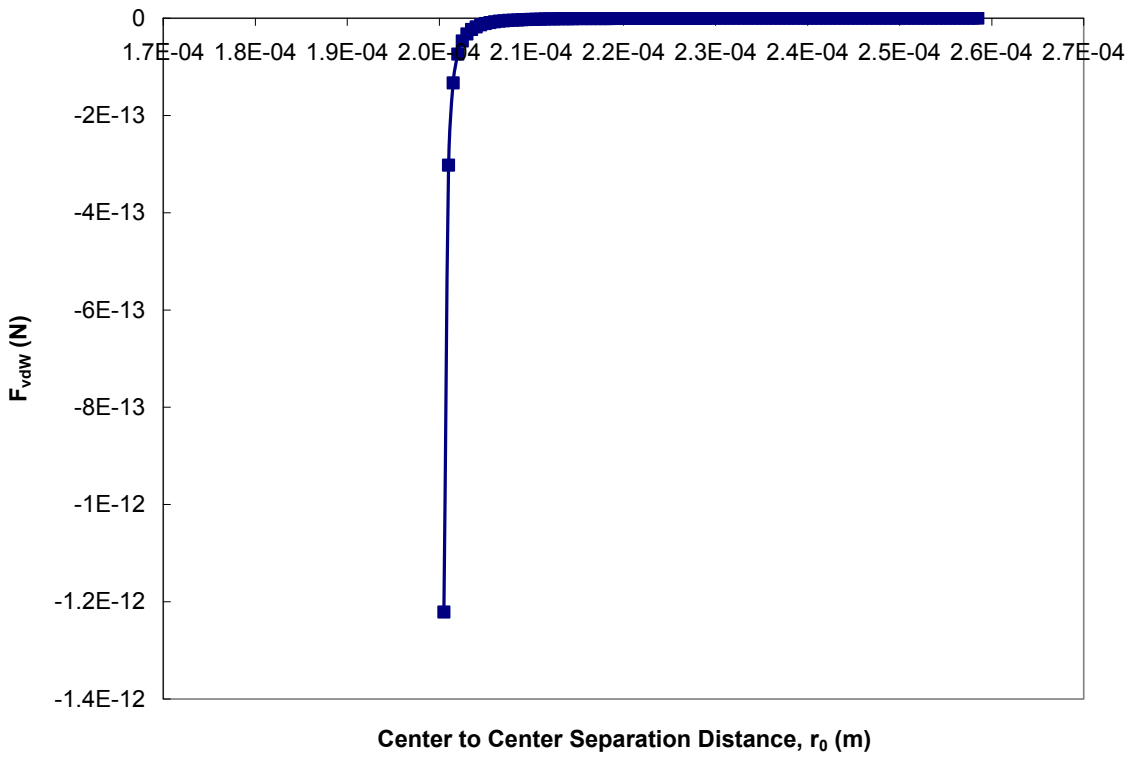

Figure 18: Van der Waals force versus center to center bubble separation distance. Both bubble radii are 100 µm and Eac is 0.5 J/m^3.

3.3.3 Relative Brownian Diffusivity

Another inter-bubble force that has to be considered arises from Brownian motion. The relative diffusivity due to Brownian motion for two widely separated drops can be seen in equation (3.37) [52].

$$D_{12}^{0} = \frac{kT(\hat{\mu}+1)(1+\hat{a}^{-1})}{2\pi\mu_l(3\hat{\mu}+2)a_1} \tag{3.37}$$

For Equation (3.37) k is the Boltzmann constant, T is the absolute temperature, and $\hat{\mu} = \frac{\mu_g}{\mu_l}$. For this system and a bubble radius of 100 µm, the relative Brownian diffusivity is $6.24 \cdot 10^{-15}$ m^2/s. Following a similar analysis as that done for the van der

Waals force, the relative magnitude of the Brownian effects $\left(\frac{kT}{2\pi a_1}\right)$ is approximately $6 \bullet 10^{-18}$ N. This compared to the magnitude of the secondary acoustic force at collision ($3.1 \bullet 10^{-5}$ N) shows a 13 order of magnitude difference, which indicates that the Brownian motion can be neglected in the overall model.

3.3.4 Hydrodynamic Forces

When two bubbles are in close proximity, within several radii, hydrodynamic interactions inhibit their movement toward each other resulting in bubbles flowing around each other [52]. Once they are sufficiently close an attractive van der Waals force, or in this case an attractive secondary acoustic force, comes into play pulling the bubbles together. The hydrodynamic interaction between two non-rigid spheres is determined by calculating their relative mobility functions. When calculating the hydrodynamic interactions both axisymmetric (resulting from forces felt equally by both bubbles) and asymmetric (resulting from the interaction of the bubbles) motion of the two bubbles must be considered. Haber, Hestroni, and Solan as well as Rushton and Davies derived exact solutions for the quasi steady-state creeping flow internal and external to two spherical droplets moving along their lines of center (axisymmetric motion) [54, 55]. Zinchenko derived exact solutions for two spherical droplets moving normal to their lines of centers (asymmetric motion) [56]. Zhang and Davis used these analyses to derive far-field and near-field expressions for both axisymmetric (*L(s)*, *G(s)*) and asymmetric (*M(s)*, *H(s)*) relative mobility functions as a function of $\hat{\mu} = \frac{\mu_g}{\mu_l}$, $\hat{a} = \frac{a_2}{a_1}$ (where a_1 is the radius

of the larger bubbles and a_2 is the radius of the smaller bubble), and the dimensionless separation distance, $s = \frac{2r}{a_1 + a_2}$ (where r is the surface to surface separation distance of the two bubbles) [52]. Equations for the far field mobility functions can be seen in equations (3.38) – (3.41). All the mobility function information is as detailed by Zhang and Davis [52]. To allow the use of these equations for the case of $\hat{a} = \frac{a_2}{a_1} = 1$ the numerators and denominators are multiplied out giving equations (3.42) – (3.44) (H(s) is not used for these calculations; this will be explained later).

$$L(s) = 1 - \frac{2+3\hat{\mu}}{1+\hat{\mu}} \frac{\hat{a}^3 - 1}{(1+\hat{a})(\hat{a}^2 - 1)} \frac{1}{s} + 4 \frac{\hat{\mu}}{1+\hat{\mu}} \frac{(\hat{a}^3 - 1)(\hat{a}^2 + 1)}{(1+\hat{a})^3 (\hat{a}^2 - 1)} \frac{1}{s^3} + O\left(\frac{1}{s^6}\right) \tag{3.38}$$

$$G(s) = 1 - 2\frac{2+3\hat{\mu}}{1+\hat{\mu}} \frac{\hat{a}}{(1+\hat{a})^2} \frac{1}{s} + 8 \frac{\hat{\mu}}{1+\hat{\mu}} \frac{\hat{a}(\hat{a}^2+1)}{(1+\hat{a})^4} \frac{1}{s^3} - 4 \frac{(2+5\hat{\mu})(2+3\hat{\mu})}{(1+\hat{\mu})^2} \frac{\hat{a}(\hat{a}^3+1)}{(1+\hat{a})^5} \frac{1}{s^4} + O\left(\frac{1}{s^6}\right)$$

(3.39)

$$M(s) = 1 - \frac{2+3\hat{\mu}}{2(\hat{\mu}+1)} \frac{\hat{a}^3 - 1}{(1+\hat{a})(\hat{a}^2 - 1)} \frac{1}{s} - 2 \frac{\hat{\mu}}{1+\hat{\mu}} \frac{(\hat{a}^3 - 1)(\hat{a}^2 + 1)}{(1+\hat{a})^3 (\hat{a}^2 - 1)} \frac{1}{s^3} + O\left(\frac{1}{s^6}\right) \tag{3.40}$$

$$H(s) = 1 - \frac{2+3\hat{\mu}}{\hat{\mu}+1} \frac{\hat{a}}{(1+\hat{a})^2} \frac{1}{s} - 2 \frac{\hat{\mu}}{1+\hat{\mu}} \frac{\hat{a}^3 - \hat{a}}{(1+\hat{a})^2} \frac{1}{s^3} + O\left(\frac{1}{s^6}\right) \tag{3.41}$$

$$L(s) = 1 - \frac{2+3\hat{\mu}}{1+\hat{\mu}} \frac{(\hat{a}^2 + \hat{a} + 1)}{(1+\hat{a})^2} \frac{1}{s} + 4 \frac{\hat{\mu}}{1+\hat{\mu}} \frac{(\hat{a}^2 + \hat{a} + 1)(\hat{a}^2 + 1)}{(1+\hat{a})^3 (\hat{a}+1)} \frac{1}{s^3} + O\left(\frac{1}{s^6}\right) \tag{3.42}$$

$$G(s) = 1 - 2\frac{2+3\hat{\mu}}{1+\hat{\mu}} \frac{\hat{a}^3}{(1+\hat{a})^2} \frac{1}{s} + 8 \frac{\hat{\mu}}{1+\hat{\mu}} \frac{\hat{a}(\hat{a}^2+1)}{(1+\hat{a})^4} \frac{1}{s^3} - 4 \frac{(2+5\hat{\mu})(2+3\hat{\mu})}{(1+\hat{\mu})^2} \frac{\hat{a}(\hat{a}^3+1)}{(1+\hat{a})^5} \frac{1}{s^4} + O\left(\frac{1}{s^6}\right)$$

(3.43)

$$M(s) = 1 - \frac{2+3\hat{\mu}}{2(\hat{\mu}+1)} \frac{(\hat{a}^2 + \hat{a} + 1)}{(1+\hat{a})^2} \frac{1}{s} - 2 \frac{\hat{\mu}}{1+\hat{\mu}} \frac{(\hat{a}^2 + \hat{a} + 1)(\hat{a}^2 + 1)}{(1+\hat{a})^3 (\hat{a}+1)} \frac{1}{s^3} + O\left(\frac{1}{s^6}\right) \tag{3.44}$$

The near field axisymmetric mobility functions, *L(ξ)* and *G(ξ)*, can be seen in equations (3.45) and (3.46). These have been reduced for the bubble case where $\xi = s - 2 \ll 1$ and $m = \frac{(a_m / L)^{1/2}}{\hat{\mu}} \gg 1$, where $a_m = \frac{a_1 a_2}{(a_1 + a_2)}$ and $L = r - (a_1 + a_2)$. The parameter m describes the mobility of the interfaces. When $m \ll 1$ the spheres behave as if they are rigid. When $m \gg 1$ the spheres have fully mobile interfaces and offer relatively little resistance to the drop relative motion.

$$L(\xi) = \frac{(\hat{a}^2 \beta_1 - \beta_2)\frac{3\hat{\mu}+2}{3\hat{\mu}+3}}{(\hat{a}^2 - 1)\left[\Lambda\left(\beta_2 + \frac{1}{\hat{a}}\beta_1\right) - \frac{1}{\hat{a}}\beta_1^2 \frac{3\hat{\mu}+2}{3\hat{\mu}+3}\right]} \tag{3.45}$$

$$G(\xi) = \frac{(\beta_1 - \hat{a}\beta_2)\frac{3\hat{\mu}+2}{3\hat{\mu}+3}}{(1+\hat{a})\left[\Lambda\left(\beta_2 + \frac{1}{\hat{a}}\beta_2\right) - \frac{1}{\hat{a}}\beta_1^2 \frac{3\hat{\mu}+2}{3\hat{\mu}+3}\right]} \tag{3.46}$$

$$\Lambda(\xi) = \frac{\pi^2\sqrt{2}\hat{\mu}}{16\left(1+\frac{1}{\hat{a}}\right)^{3/2}}\left(\frac{2}{\xi(1+\hat{a})}\right)^{1/2} + \frac{\hat{a}}{3(1+\hat{a})}\left(1 - \frac{\hat{\mu}^2}{3}\right)\ln\left(\xi\frac{(1+\hat{a})}{2}\right)^{-1} + C_0 \tag{3.47}$$

$$\beta_1 = \beta_2 = 0.98826 + (-0.52509)\exp\left(\frac{-(\hat{a}+0.50433)}{1.81706}\right) + (-1.76884)\exp\left(\frac{-(\hat{a}+0.50433)}{0.45213}\right) \tag{3.48}$$

$$C_0 = 0.6565 + \frac{-0.01729}{1+\exp\left(\frac{\hat{a}-0.38931}{0.14521}\right)} \tag{3.49}$$

In equations (3.45) and (3.46) the values for C_0, β_1, and β_2 are determined from equations extracted from graphed tabulated data from Zhang and Davis [52]. For this case, β_1 and β_2 are equal since it is assumed that all the gas bubbles the same species. The fit data for

C_0, β_1, and β_2 were obtained by using a non-linear curve fit in Origin 7.5, and are seen in equations (3.48) and (3.49). These values are specific for the case of $\hat{\mu} = 0$ which most approximates a gas bubble in water. The graph of these can be seen in Figure 19 and Figure 20.

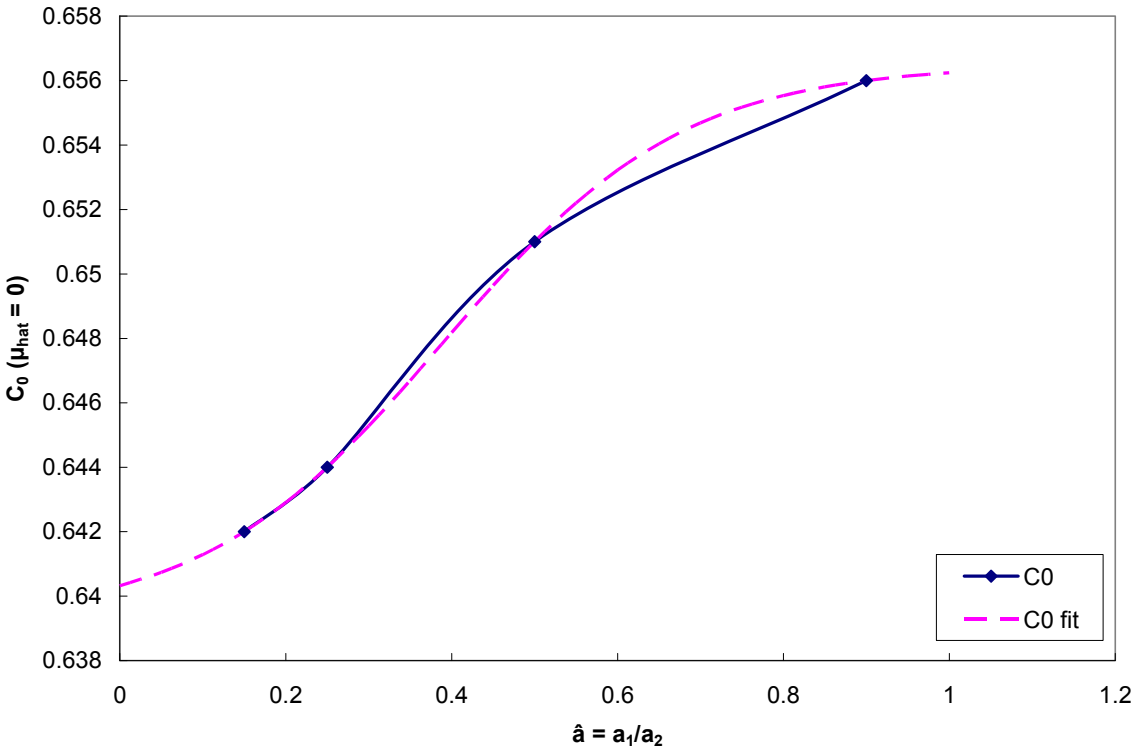

Figure 19: Graphical representation of tabulated data from Zhang and Davis [52] for C_0 values and the fit data obtained from Origin 7.5.

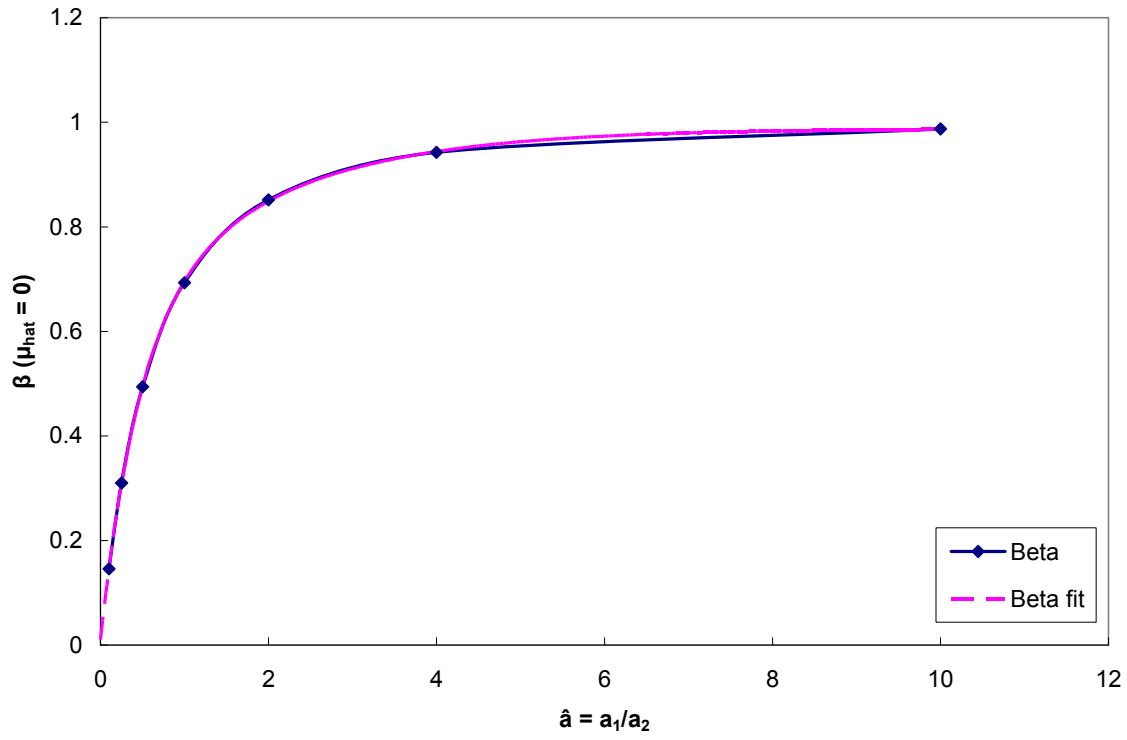

Figure 20: Graphical representation of tabulated data from Zhang and Davis [52] for $\beta_1 = \beta_2$ values and the fit data obtained from Origin 7.5.

The near field asymmetric mobility function, *M(ξ)*, can be seen in equation (3.50). The terms M_1 and M_2 are determined from equations extracted from graphed tabulated data from Zhang and Davis [52]. The fit data for M_1 and M_2 were obtained by using a non-linear curve fit in Origin 7.5. These values are specific for the case of $\hat{\mu} = 0$. The graph of both M_1 and M_2 can be seen in Figure 21 and Figure 22.

$$M(\xi) = M_0 + M_1\xi + O(\xi^2) \tag{3.50}$$

$$M_0 = 0.62188 - (0.12435)0.01584^{\hat{a}} \tag{3.51}$$

$$M_1 = (4.0849)\exp\left(\frac{-\hat{a}}{0.09166}\right) + 0.17953 \tag{3.52}$$

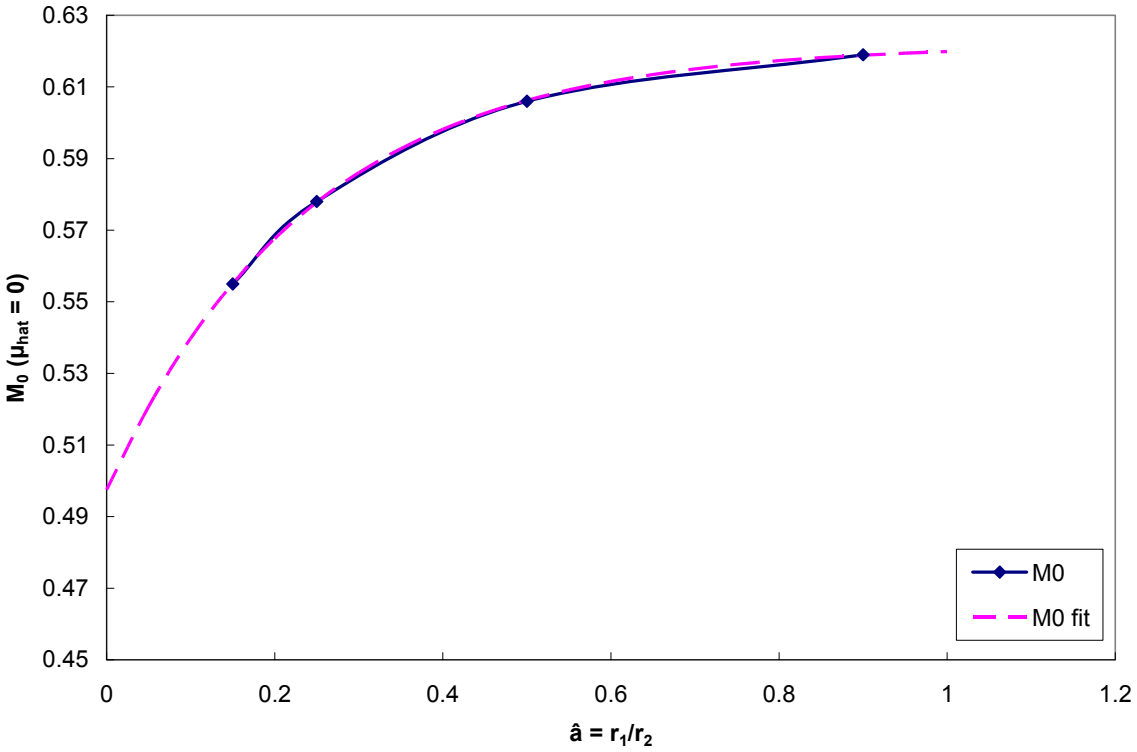

Figure 21: Graphical representation of tabulated data from Zhang and Davis [52] for M_0 values and the fit data obtained from Origin 7.5.

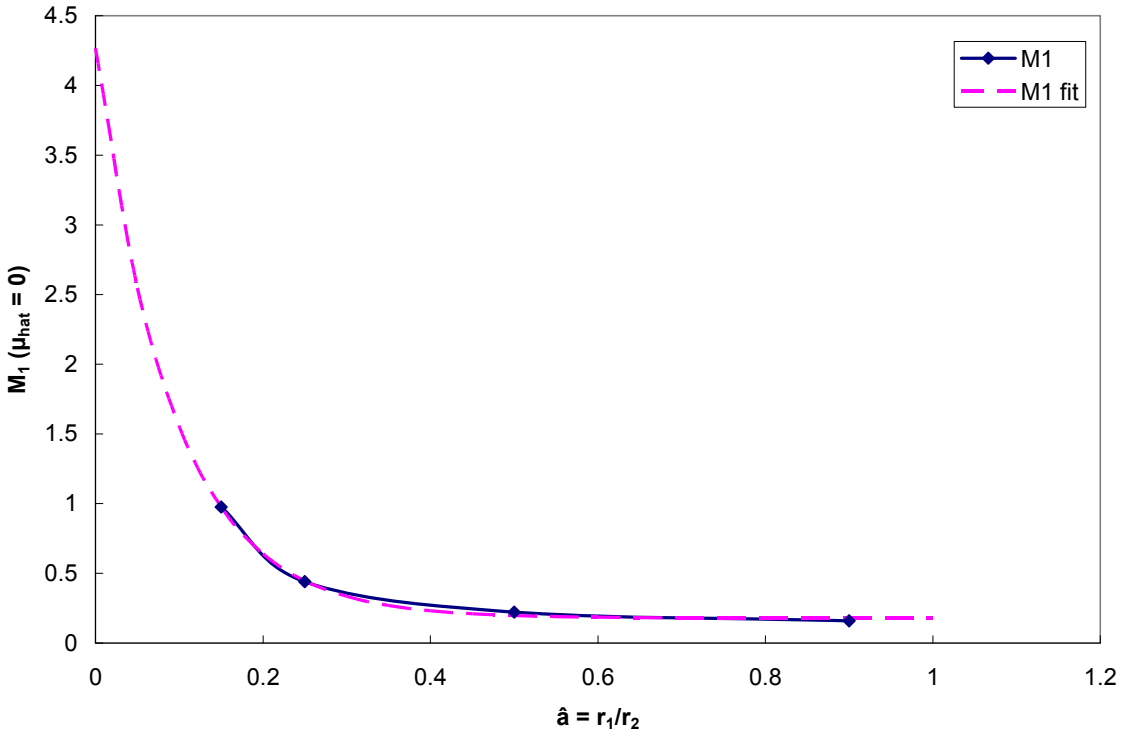

Figure 22: Graphical representation of tabulated data from Zhang and Davis [52] for M_1 values and the fit data obtained from Origin 7.5

Once the near field and far field mobility functions have been calculated, it must be determined at what range each solution is valid. A test case using the mobility function G is given where $\hat{a} = 0.909$ and $\hat{\mu} = 0.0173 \approx 0$. The near field and far field mobility functions are graphed in Figure 23. The two graphs overlap at approximately *s* = 2.00004668, which can be seen in Figure 24 which is a close up of this intersection.

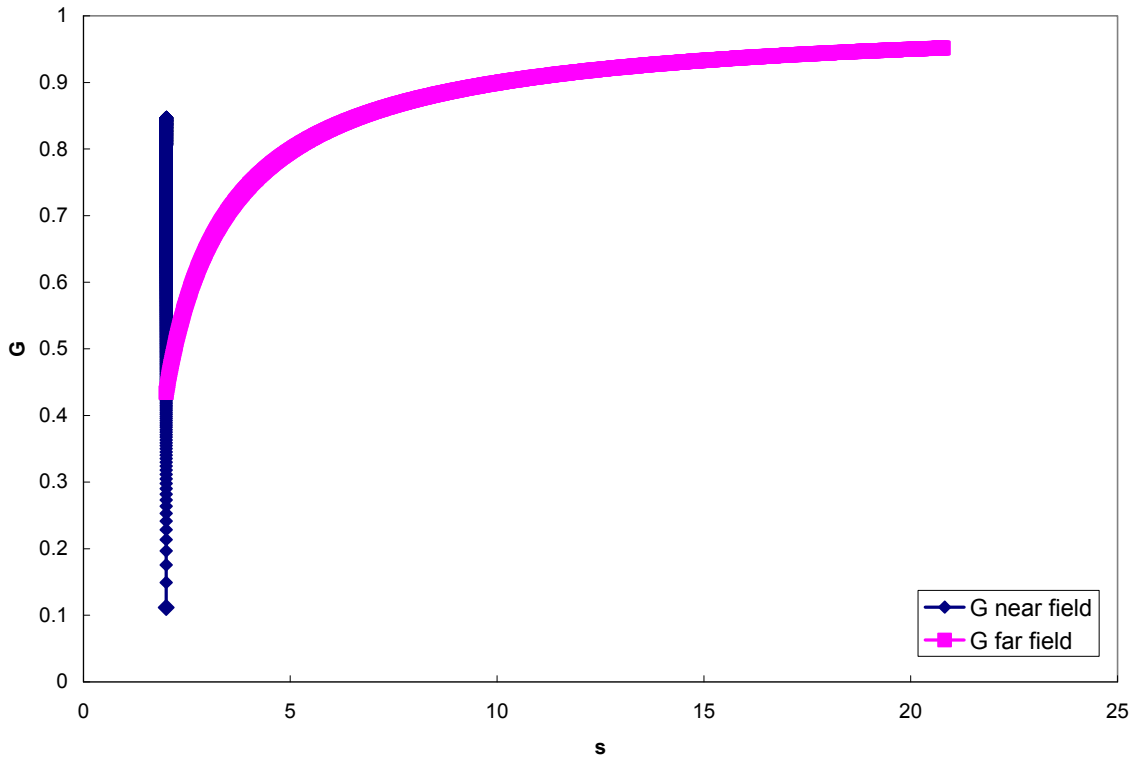

Figure 23: Graph of the near field mobility function G(ξ) and the far field mobility function G(s) where $\hat{a} = 0.909$ (a_1=110 µm and a_2=100µm) and $\hat{\mu} = 0.0173 \approx 0$.

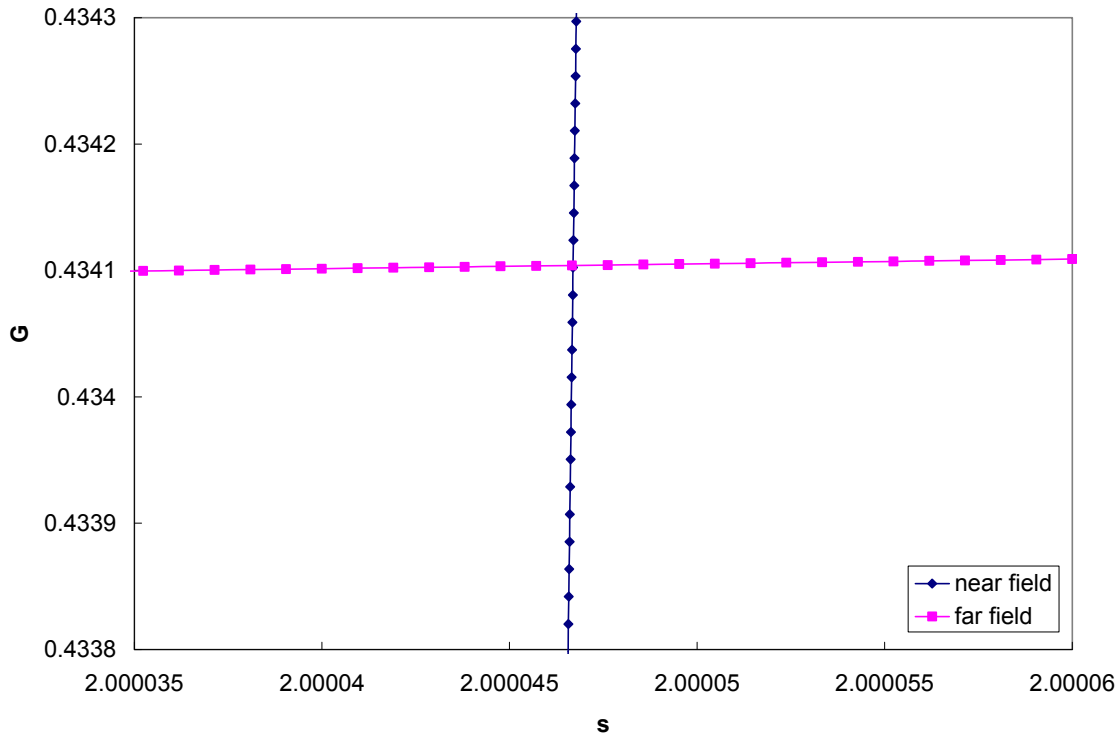

Figure 24: Close up of the intersection of the near field mobility function G(ξ) and the far field mobility function G(s) where $\hat{a} = 0.909$ (a_1=110 µm and a_2=100µm) and $\hat{\mu} = 0.0173 \approx 0$.

It was decided to choose the near field form to be valid up to $s = 2.00004$ and the far field to be valid from $s = 2.0002$. To close the gap between the two curves, a spline was used. After trying a few different spline techniques, the best fit was shown to be achieved with a cubic spline interpolation [168]. The details of this method can be seen in (3.53) – (3.57) using Q as a general term for the variety of mobility functions.

$$Q_{\text{modified}} = \hat{A} Q_{near}\Big|_{s_{near}} + \hat{B} Q_{far}\Big|_{s_{far}} + \hat{C} Q''_{near}\Big|_{s_{near}} + \hat{D} Q''_{far}\Big|_{s_{far}} \tag{3.53}$$

$$\hat{A} = \frac{s_{far} - s}{s_{far} - s_{near}} \tag{3.54}$$

$$\hat{B} = 1 - \hat{A} = \frac{s - s_{near}}{s_{far} - s_{near}} \tag{3.55}$$

$$\hat{C} = \frac{1}{6}(\hat{A}^3 - \hat{A})(s_{far} - s_{near})^2 \tag{3.56}$$

$$\hat{D} = \frac{1}{6}(\hat{B}^3 - \hat{B})(s_{far} - s_{near})^2 \tag{3.57}$$

Mathematica 6 was utilized to do these calculations. A detailed print out of the Mathematica code can be seen in Appendix A1. Due to round off error incurred in Excel, the graphical results are presented in Mathematica format and are seen in Figure 25 with the origin being shown as (2, 0). This is again data for the near field mobility function G with $\hat{a} = 0.909$ and $\hat{\mu} = 0.0173 \approx 0$.

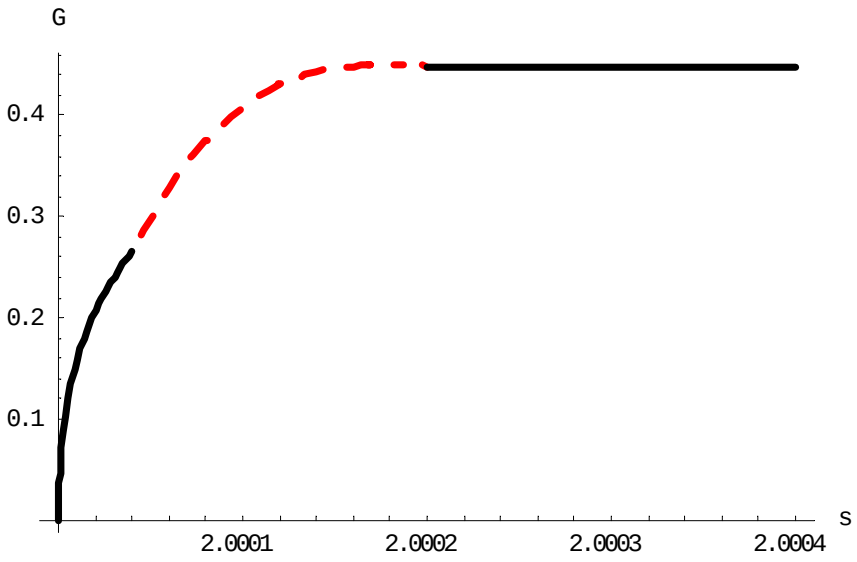

Figure 25: Mathematica graph showing the near field mobility function G(ξ) up to s = 2.00004 and the far field mobility function G(s) from s = 2.0002 with the cubic spline interpolation (red dotted line) connecting the two curves.

After closer inspection it was decided that because the far field mobility function, *G(s)*, appears to be valid down to *s* = 2.00004668 the entire mobility function could be approximated as the far field. This is a consistent trend with the other mobility functions.

3.3.5 Relative Bubble Motion

Using the coordinate system seen in Figure 26, equation (3.58) [52, 80] gives the relative velocity for spherical bubbles.

$$V_{12}(\bar{r}) = V_{12}^{0} \bullet \left[\frac{\overline{rr}}{r^2} L(s) + \left(\bar{I} - \frac{\overline{rr}}{r^2} \right) M(s) \right] - \frac{D_{12}^{0}}{kT} \left[\frac{\overline{rr}}{r^2} G(s) + \left(\bar{I} - \frac{\overline{rr}}{r^2} \right) H(s) \right] \bullet \nabla(\Phi_{12}) \\ - D_{12}^{0} \left[\frac{\overline{rr}}{r^2} G(s) + \left(\bar{I} - \frac{\overline{rr}}{r^2} \right) H(s) \right] \bullet \nabla(\ln p_{12}(\bar{r})) \tag{3.58}$$

In equation (3.58) V_{12}^{0} is the difference between the velocities of the two bubbles as if they were acted upon individually by the primary forces, $\bar{r}$ is the center to center distance vector from the smaller bubble (2) to the larger bubble (1), $\bar{I}$ is the unit second-order tensor, and Φ_{12} is the total inter-bubble force potential. The equation can basically be broken down into three different pieces. The first term represents the relative motion due to primary forces; primary acoustic, buoyancy, and drag forces. The second term represents the relative motion due to inter-bubble forces, secondary acoustic and van der Waals forces. In this term $\Phi_{12}(\bar{r})$ is the potential function that describes the inter-bubble force. The third term represents Brownian motion. It this term $p_{12}(\bar{r})$ is the pair distribution function and represents the probability that bubble one is at position $\bar{r}$ relative to bubble two normalized such that $p_{12} \to 1$ as $\bar{r} \to \infty$. Because Brownian diffusivity is negligible, as discussed earlier, for a system with $a_1 = a_2 = 100$ μm ($\hat{a} = 1$)

and $\hat{\mu} = 0.0173 \approx 0$ at a temperature of 300 K, giving a value of $D_{12}^0 = 6.24 \bullet 10^{-15}$ m^2/s, the third term of equation (3.58) can be neglected giving equation (3.59) [5]. If the bubbles being dealt with were on the order of nanometers, the Brownian diffusivity would play a more important role.

$$V_{12}(\bar{r}) = V_{12}^0 \bullet \left[\frac{\overline{rr}}{r^2} L(s) + \left(\bar{I} - \frac{\overline{rr}}{r^2} \right) M(s) \right] - \frac{D_{12}^0}{kT} \left[\frac{\overline{rr}}{r^2} G(s) + \left(\bar{I} - \frac{\overline{rr}}{r^2} \right) H(s) \right] \bullet \nabla(\Phi_{12}) \qquad (3.59)$$

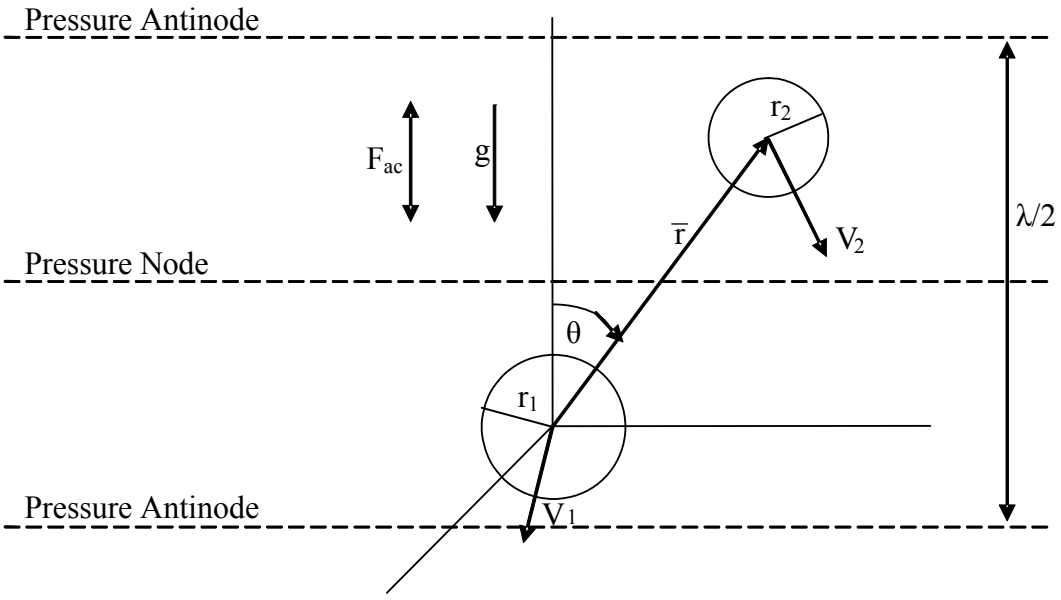

Figure 26: Schematic of the coordinate system for the relative motion of two drops in an acoustic field. Reproduced from a schematic by Zhang and Davis [52].

After the relative velocity has been derived and simplified, the equation can be altered for use in the case of a bubble pair interacting in an acoustic field, resulting in equation (3.60) [5, 52].

$$V_{12}(\bar{r}) = V_{12}^{0}\left(-L(s)\cos\theta\hat{e}_r + M(s)\sin\theta\hat{e}_\theta\right) - \left[\frac{D_{12}^{0}}{kT}G(s)\left(\frac{2A}{(a_1+a_2)}\frac{dV_{vdW}^{*}}{ds} + \frac{4\alpha_{ac}}{(a_1+a_2)^2}\frac{1}{s^2}\right)\right]\hat{e}_r \tag{3.60}$$

In equation (3.60) e_r and e_θ are the unit vectors in the radial and tangential directions, respectively, V_{12}^{0} is the relative velocity due to body forces, and V_{vdW}^{*} is the van der Waals potential made dimensionless by dividing by the Hamaker constant, A. The term α_{ac} expresses the strength of secondary acoustic forces, and can be seen in equation (3.61), where ω is the angular driving frequency, ω_1 and ω_2 are the monopole resonance frequencies of the bubbles, and $P_s = \sqrt{2\rho_l c_l^2 E_{ac}}$ is the complex pressure amplitude of the incident acoustic field [14].

$$\alpha_{ac} = \frac{2\pi\left|P_s\right|^2\omega^2 a_1 a_2}{\rho_l(\omega_1^2-\omega^2)(\omega_2^2-\omega^2)} = F_{2,ac}r^2 \tag{3.61}$$

Again, the first term in equation (3.60) represents the body forces, the second term represents the van der Waals attractive force, and the third term represents the secondary acoustic force.

To determine the relative motion of a pair bubbles, it is of benefit to separate equation (3.60) into its radial and tangential components. This can be done by assuming starting positions of the bubbles within the half wavelength region between two pressure antinodes (see Figure 26). By doing this, two ordinary differential equations can be obtained, (3.62) and (3.63). These equations were simultaneously solved numerically using Mathematica 6 to determine the time it took for two bubbles to reach $s = 2$, indicating collision. The Mathematica code for this can be seen in Appendix A2.

$$\frac{ds}{dt} = -\frac{2V_{12}^{0}L(s)\cos[\theta]}{a_1+a_2} - \frac{4D_{12}^{0}}{kT(a_1+a_2)^2}G(s)\left(A\frac{dV_{vdW}}{ds} + \frac{2\alpha_{ac}}{(a_1+a_2)}\frac{1}{s^2}\right) \tag{3.62}$$

$$\frac{d\theta}{dt} = \frac{2V_{12}^{0}M(s)\sin[\theta]}{s(a_1 + a_2)} \tag{3.63}$$

The Mathematica output for two bubbles with radii of 100 µm, an initial separation of 1 cm (s = 102), an initial separation angle of 90º, and both with starting positions at an acoustic pressure antinode (1.71 mm based of a frequency of 0.435 MHz) can be seen in Figure 27 and Figure 28. Figure 27 shows the dimensionless separation as a function of time. The graph shows an initial slower approach followed by a faster approach followed by collision of the two bubbles when s = 2. This can be seen a bit better in Figure 29 which shows the relative velocity as a function of time.

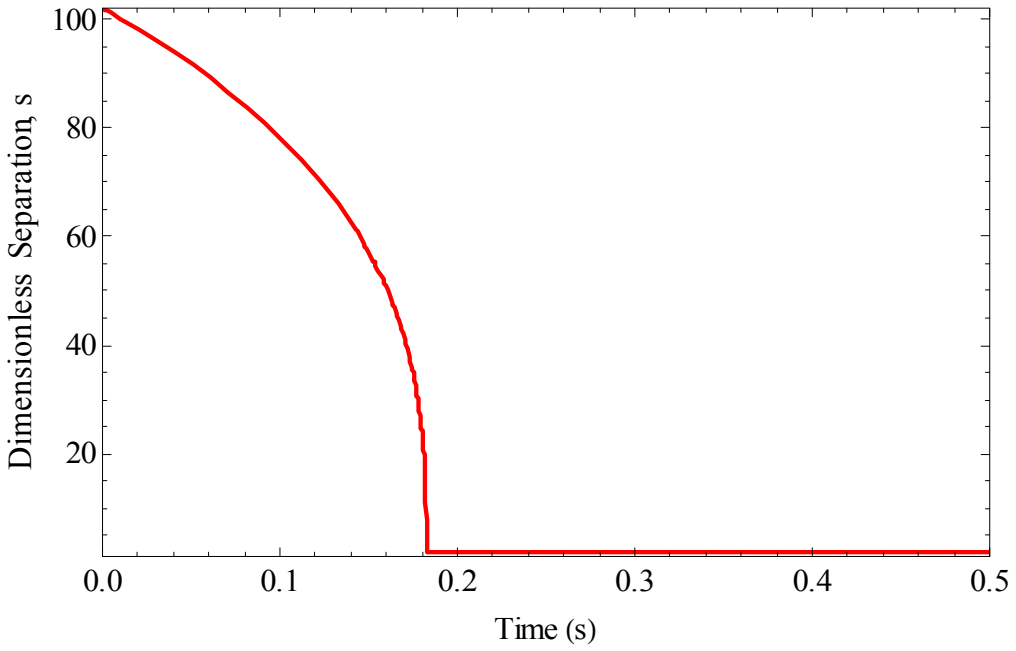

Figure 27: Dimensionless separation distance, s, as a function of time for two bubbles with radii of 100 µm, initial separation distance of 1 cm (s = 102), initial separation angle of 90º, and initial starting positions at a pressure antinode (1.71 mm). The value of Nac for these conditions is -8.134.

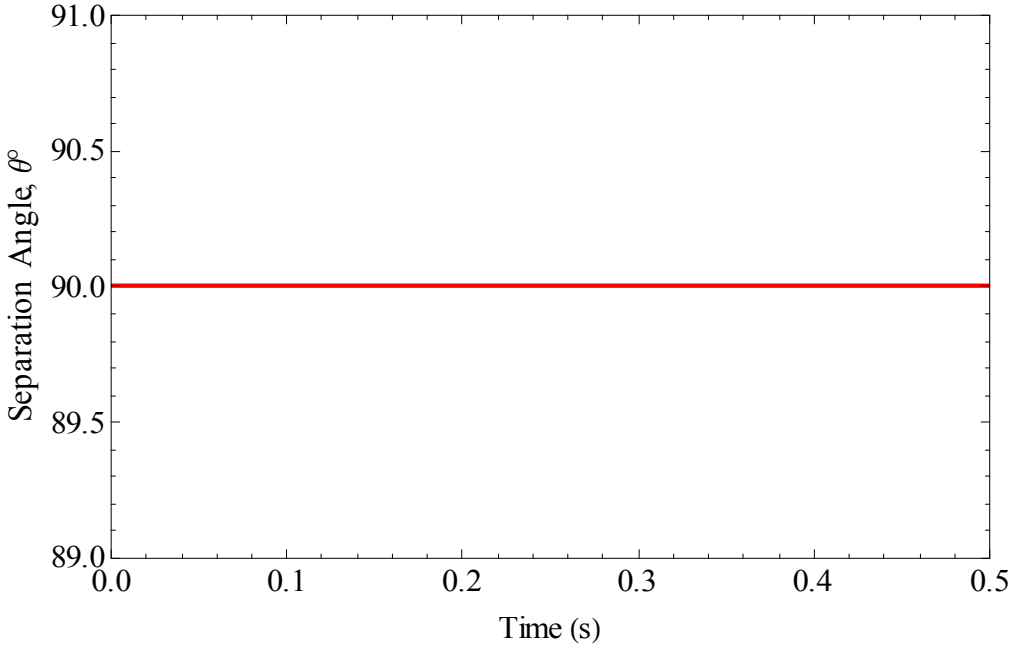

Figure 28: Separation angle, θ, as a function of time for two bubbles with radii of 100 µm, initial separation distance of 1 cm (s = 102), initial separation angle of 90º, and initial starting positions at a pressure antinode (1.71 mm). The value of Nac for these conditions is -8.134.

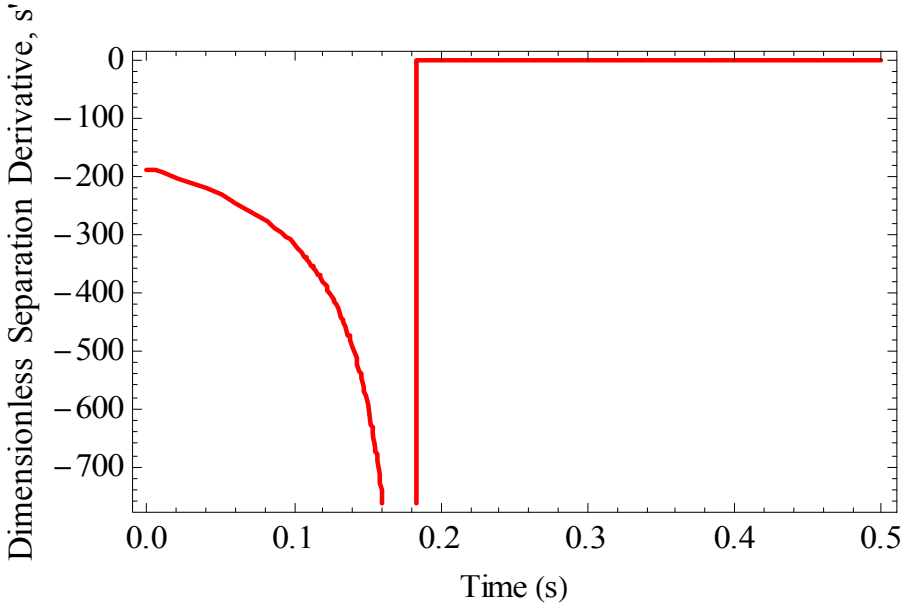

Figure 29: Relative velocity, s', as a function of time for two bubbles with radii of 100 µm, initial separation distance of 1 cm (s = 102), initial separation angle of 90º, and initial starting positions at a pressure antinode (1.71 mm). The value of Nac for these conditions is -8.134.

To plot the path of bubble two toward bubble one, s and θ can be used to calculate the x and y coordinates, equations (3.64) and (3.65). These values are made dimensionless by dividing by $\lambda/4$. Figure 30 and Figure 31 show the dimensionless x and y coordinates versus time and Figure 32 shows the relative trajectory of bubble two with respect to bubble one. For all of these cases the conditions are the same as previously mentioned, except the initial position of the bubble in the acoustic field is 1.746 mm, which is the equilibrium resting point for a 100 μm bubble in an acoustic field with an energy density of 0.5 J/m^3 based on the primary force balance. Figure 33 is the same as Figure 32 except with an initial separation angle of 225º and an initial position of bubble two at -5.466 mm. Figure 34 also has the same conditions except the bubbles have an initial separation angle of 135º and an initial separation distance of 0.5 cm giving bubble two an initial position of 1.598 mm. Figure 34 shows that as the second bubble approaches it reaches a certain separation distance and then begins to move around the first bubble. This is most likely due to the second bubble being driven to its equilibrium resting position in respect to the pressure antinode, which is calculated from the primary force balance.

$$\Delta x = r\sin[\theta] \tag{3.64}$$

$$\Delta y = r\cos[\theta] \tag{3.65}$$

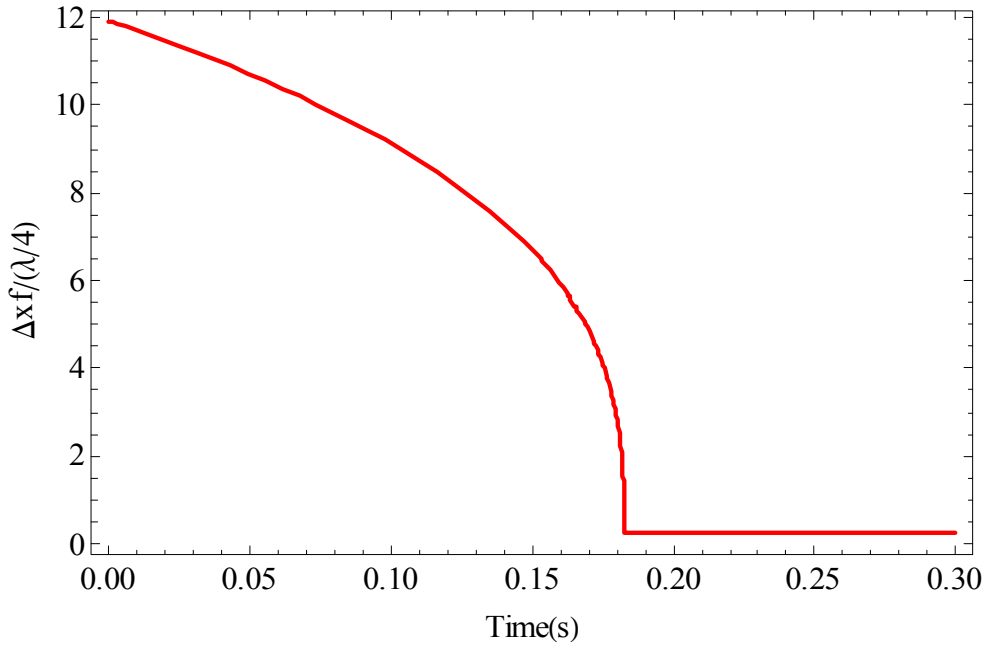

Figure 30: Dimensionless x position vs. time for two bubbles with radii of 100 µm, initial separation distance of 1 cm (s = 102), initial separation angle of 90º, and initial starting positions at their equilibrium resting position of 1.746 mm (based on the primary force balance). The value of Nac for these conditions is -8.134.

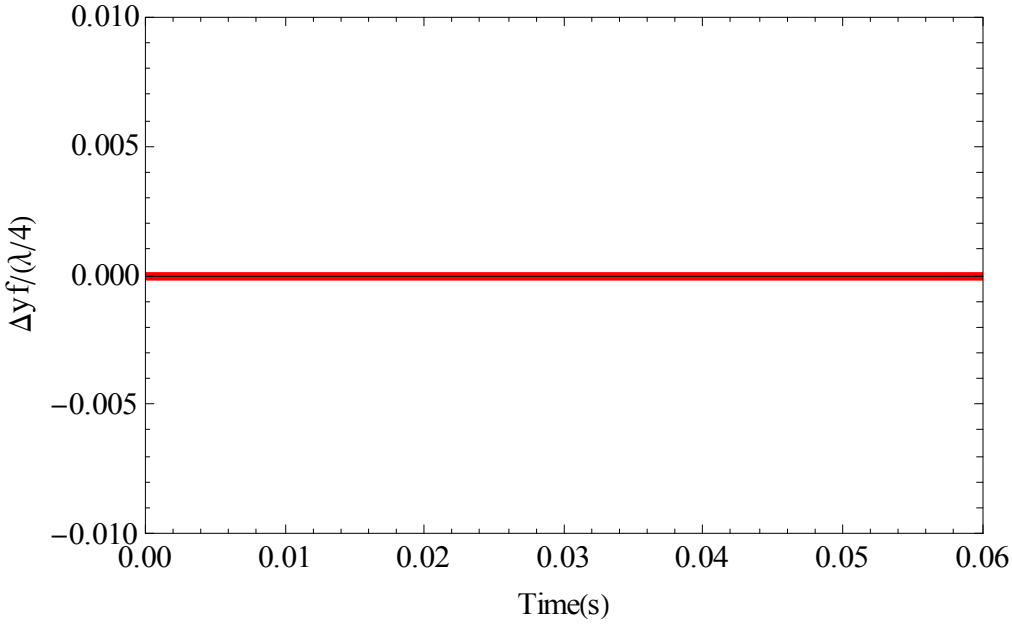

Figure 31: Dimensionless y position vs. time for two bubbles with radii of 100 µm, initial separation distance of 1 cm (s = 102), initial separation angle of 90º, and initial starting positions at their equilibrium resting position of 1.746 mm (based on the primary force balance). The value of Nac for these conditions is -8.134.

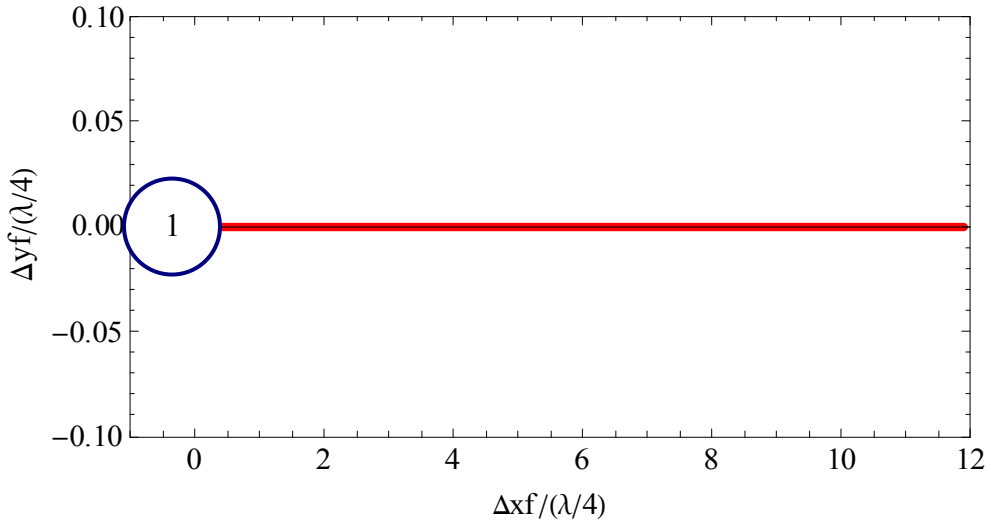

Figure 32: Relative trajectory of bubble two with respect to bubble one (shown). The graph is for two bubbles with radii of 100 µm, initial separation distance of 1 cm (s = 102), initial separation angle of 90°, and initial starting positions at their equilibrium resting position of 1.746 mm (based on the primary force balance). The value of Nac for these conditions is -8.134.

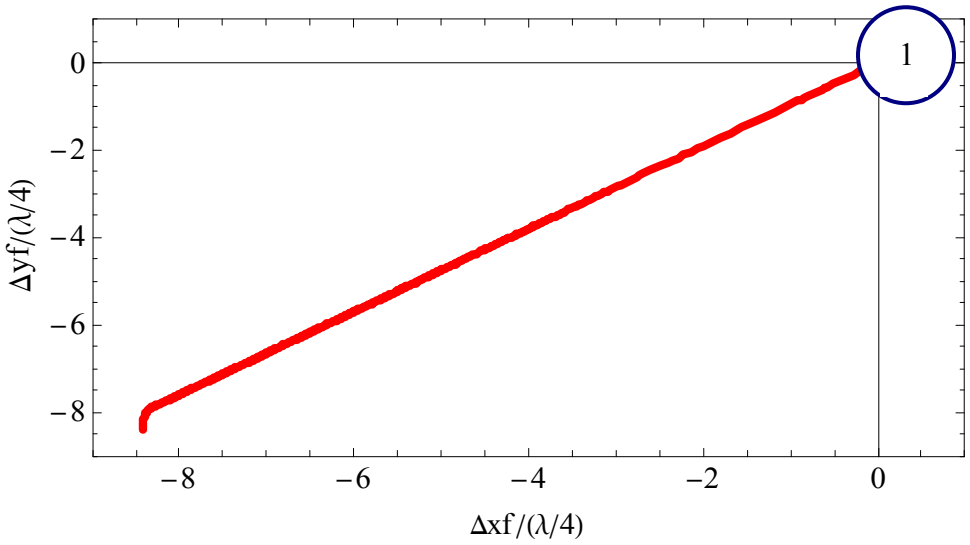

Figure 33: Relative trajectory of bubble two with respect to bubble one (shown). The graph is for two bubbles with radii of 100 µm, initial separation distance of 1 cm (s = 102), initial separation angle of 225°, and an initial starting position for bubble one at its equilibrium resting position of 1.746 mm and for bubble two -5.466 mm(based on the primary force balance). The value of Nac for these conditions is -8.134.

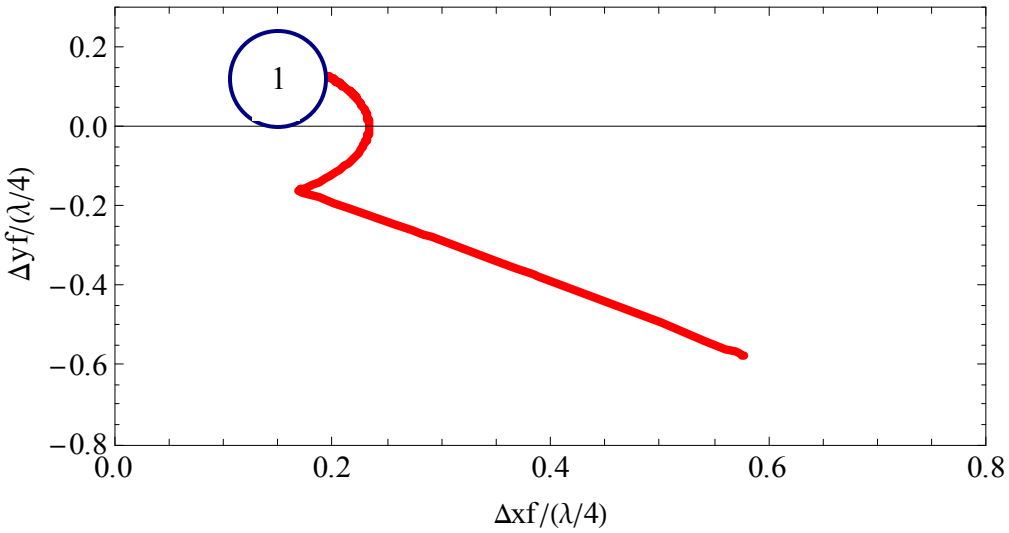

Figure 34: Relative trajectory of bubble two with respect to bubble one (shown). The graph is for two bubbles with radii of 100 µm, initial separation distance of 0.5 cm (s = 7), initial separation angle of 135º, and an initial starting position for bubble one at its equilibrium resting position of 1.746 mm and for bubble two 1.598 mm (based on the primary force balance). The value of Nac for these conditions is -8.134.

It may seem initially counterintuitive that the second bubble can work its way through several pressure nodes and antinodes to reach the first bubble. This depends on how large the secondary acoustic force is compared to the difference between primary acoustic force and the buoyancy force. In other words, if the secondary acoustic force can overcome the difference between the primary acoustic and buoyancy forces, then the second bubble will be pulled across the pressure antinodes that separate it from the first bubble. Calculating the primary acoustic force, equation (3.4), at the first pressure node (y = 0.856 mm), which is the location where the force is the greatest, a value of $5.12 \cdot 10^{-8}$ N is obtained (θ = 90º, f = 0.435 MHz, Eac = 0.5 J/m^3, a = 100 µm). The buoyancy force for the same system, equation (3.6), is calculated to be $4.09 \cdot 10^{-8}$ N. The maximum center to center separation between the two bubbles ($a_1 = a_2$ = 100 µm), r, can be found at a secondary acoustic force value equal to the difference between the primary acoustic force

and buoyancy force ($1.02 \bullet 10^{-8}$ N). This maximum separation for this system is 1.1 cm, assuming a separation angle of 180 º. The value will change based on that separation angle and can be calculated according to equation (3.65).

Figure 35 shows the time to collision as a function of the initial surface to surface separation of the two bubbles, with the radius of bubble one at 100 μm and the radius of bubble two varying ($a_{hat} = a_2/a_1$). There is an initial separation that ranges from $1.0 \bullet 10^{-7}$ m to 0.01 m, an initial separation angle of 90º, and both bubbles have starting positions at an acoustic pressure antinode (1.71 mm based of a frequency of 0.435 MHz). The initial separation distance of $1.0 \bullet 10^{-7}$ was chosen based on the hydrodynamic mobility functions. Previously it was decided that the far field mobility functions were a sufficient approximation without the near field mobility functions could be disregarded, and it was found that the far field mobility functions were accurate down to an *s* value of 2.00004668. This *s* value was used to calculate an L_0 value of about $4.5 \bullet 10^{-8}$ (assuming $a_1 = a_2 = 100$ μm). From this it was decided that a minimum initial separation of $1.0 \bullet 10^{-7}$ was sufficiently small. Figure 35 shows that the time to collision increases as the radius of bubble two increases.

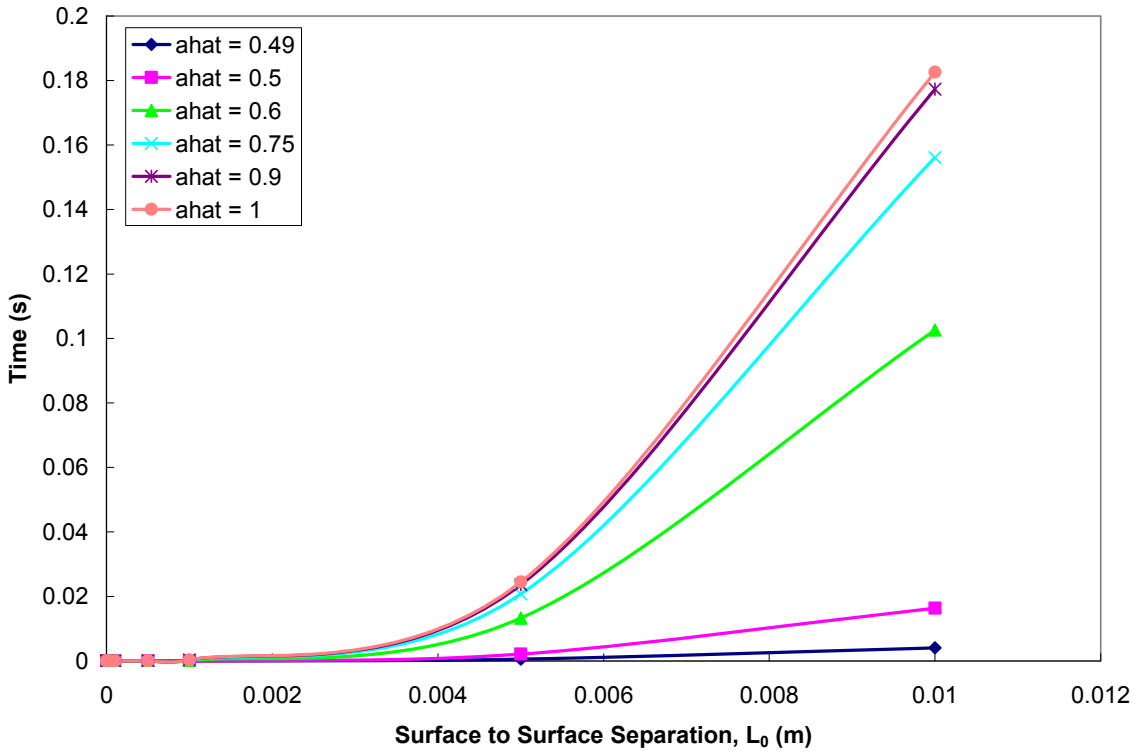

Figure 35: Time to collision based on initial surface to surface separations. The radius of bubble one is 100 µm with the radius of bubble two varying for each curve ($a_{hat}=a_2/a_1$). The initial angle between the two bubbles is 90° and the initial starting position for both bubbles is at a pressure antinode (1.71 mm). The value of Nac for bubble one at these conditions is -8.134.

Subsequent analogous calculations were done for a_1 = 260 µm, which is the largest bubble that can be captured (though at this size the spherical assumption does not hold). Again, the radius of bubble two was varied and the same conditions apply as for Figure 35. Figure 36 shows the time to collision as a function of initial surface to surface separation. Though it may be slightly difficult to make out on the graph, the curve for a_{hat} = 0.75 overlaps the curve for a_{hat} = 0.4. This indicates that the time to collision decreases once a_{hat} hits a certain limit. This can be better seen in Figure 37 which shows the time to collision as a function of a_{hat} for an initial surface to surface separation distance of 1 cm.

The separation of 1 cm was chosen because this trend does not appear at closer initial separations.

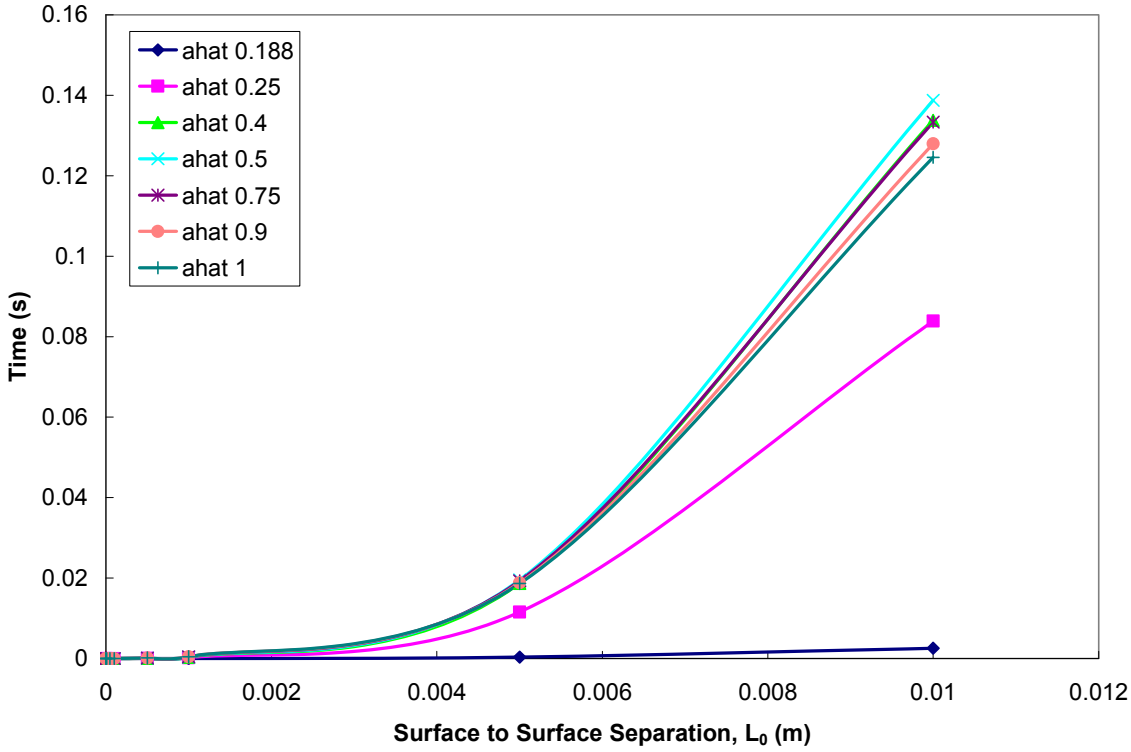

Figure 36: Time to collision based on initial surface to surface separations. The radius of bubble one is 260 µm with the radius of bubble two varying for each curve ($a_{hat}=a_2/a_1$). The initial angle between the two bubbles is 90° and the initial starting position for both bubbles is at a pressure antinode (1.71 mm). The value of Nac for bubble one at these conditions is -1.008.

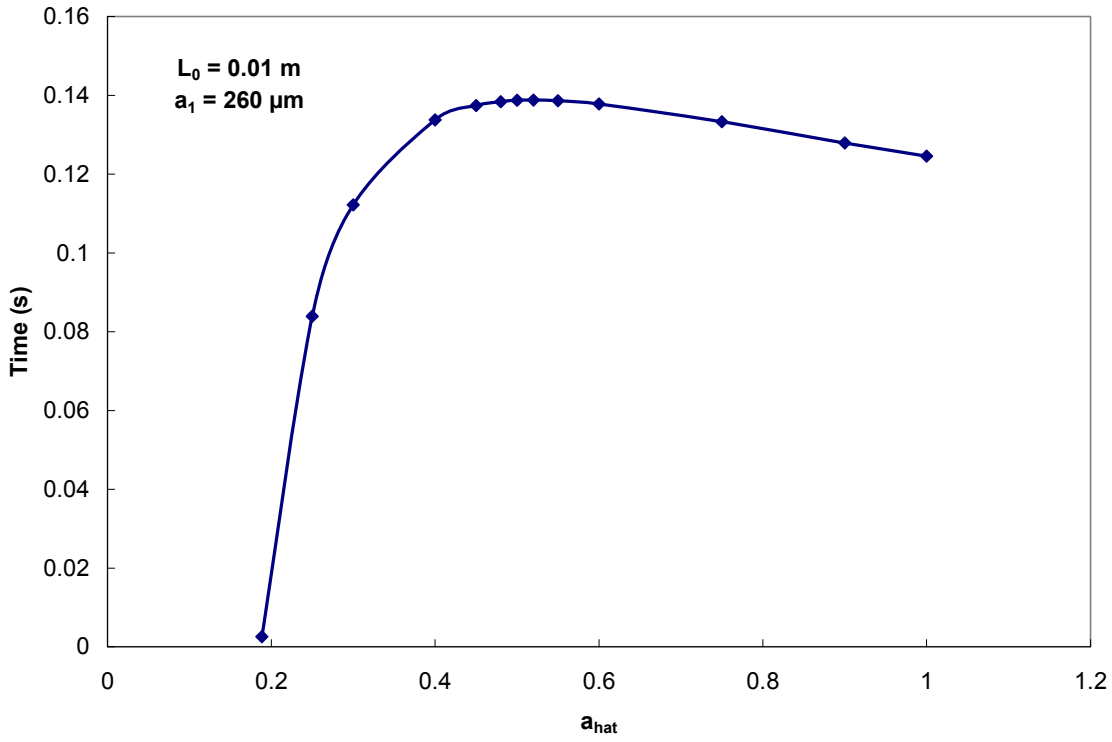

Figure 37: Time to collision versus a_{hat} for two bubbles with an initial surface to surface separation of 1 cm. The radius of bubble one is 260 µm with the radius of bubble two varying for each curve ($a_{hat}=a_2/a_1$). The initial angle between the two bubbles is 90° and the initial starting position for both bubbles is at a pressure antinode (1.71 mm). The value of Nac for bubble one at these conditions is -1.008.

After this trend appeared for the case of a_1 = 260 µm it was decided to investigate whether this trend was seen for other values of a_1. Figure 38 and Figure 39 show the same calculations for a_1 = 200 µm and a_1 = 150 µm, respectively. It can be seen that in both of these subsequent cases the time to collision also peaks at an a_{hat} value not equal to one. For a_1 = 260 the collision time peaks at about a_{hat} = 0.52, for a_1 = 200 µm the collision time peaks at about a_{hat} = 0.65, and for a_1 = 150 µm the collision time peaks at about a_{hat} = 0.85. Though the graph is not shown here, the case of a_1 = 110 µm seems to be about as large as a_1 can become before the collision time stops peaking at a_{hat} = 1.

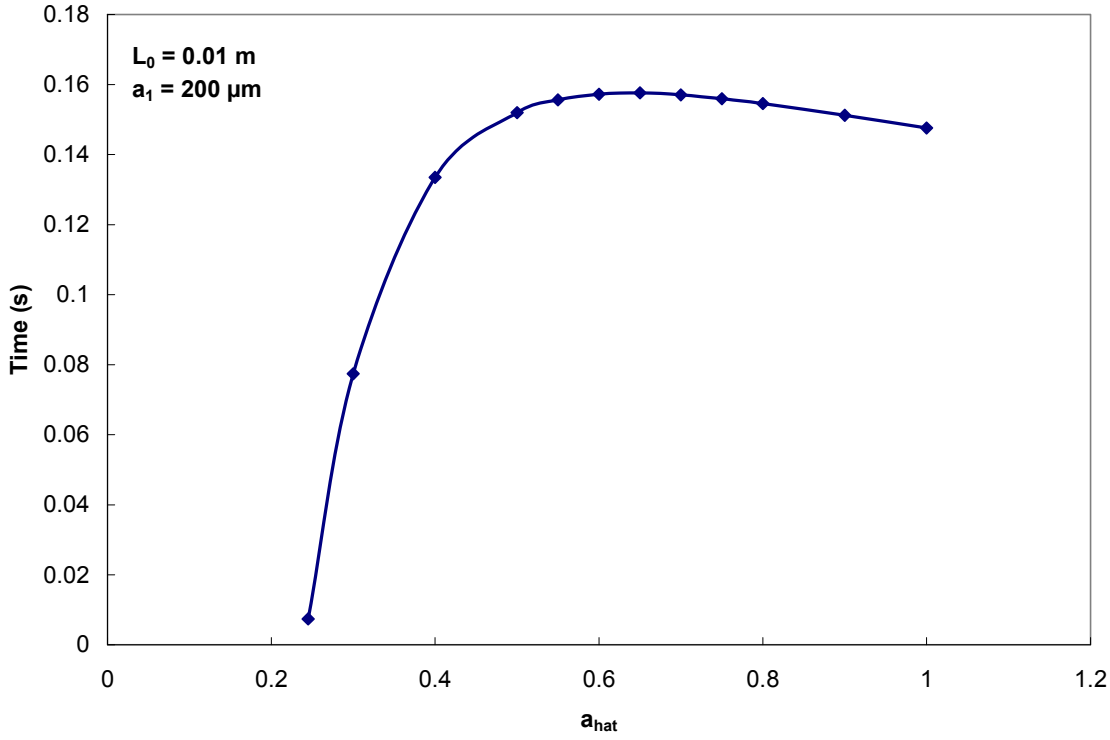

Figure 38: Time to collision versus a_{hat} for two bubbles with an initial surface to surface separation of 1 cm. The radius of bubble one is 200 µm with the radius of bubble two varying for each curve ($a_{hat}=a_2/a_1$). The initial angle between the two bubbles is 90° and the initial starting position for both bubbles is at a pressure antinode (1.71 mm). The value of Nac for bubble one at these conditions is -1.844.

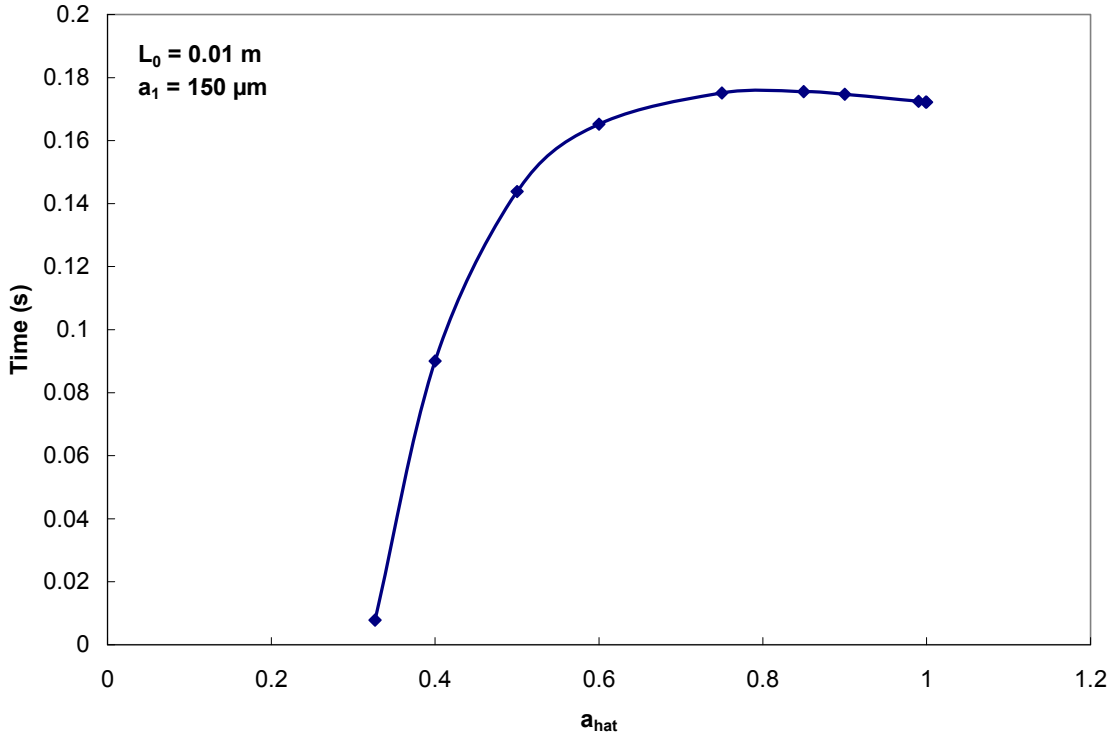

Figure 39: Time to collision versus a_{hat} for two bubbles with an initial surface to surface separation of 1 cm. The radius of bubble one is 150 µm with the radius of bubble two varying for each curve ($a_{hat}=a_2/a_1$). The initial angle between the two bubbles is 90° and the initial starting position for both bubbles is at a pressure antinode (1.71 mm). The value of Nac for bubble one at these conditions is -3.462.

The decreasing time to collision after a_{hat} reaches a certain value most likely results from the dependence of the forces on the radii of the bubbles. The dependence of the primary and secondary acoustic forces on the bubble radius is a bit complicated due to the acoustic contrast factor and monopole resonance frequency. A subsequent calculation was run where both bubbles' initial vertical positions were located at their respective equilibrium resting spot. These values were calculated from the primary force balance for each bubble size. This was done to determine if the primary acoustic force was having a large effect on the collision time and to see if the tapering off and decrease

of the collision time was due in part to the bubbles obtaining their equilibrium position along the *y*-axis. Figure 40 shows the comparison of this curve to that of the bubbles starting at an acoustic pressure antinode (1.71 mm). There is no discernable difference between the two. This indicates that the small distance the bubbles had to move vertically to sit at their equilibrium positions did not have a significant influence on the collision time reversal effect and that this phenomena is most likely due to the secondary acoustic forces.

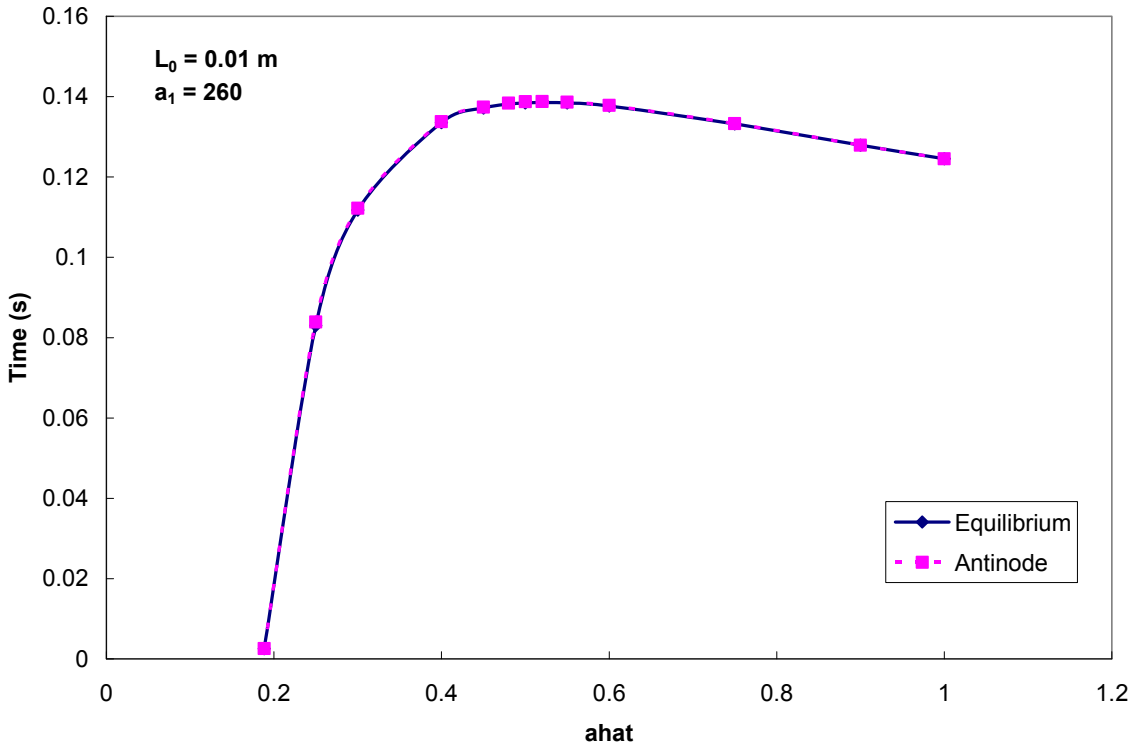

Figure 40: Time to collision versus a_{hat} for two bubbles with an initial surface to surface separation of 1 cm. The radius of bubble one is 260 µm with the radius of bubble two varying for each curve ($a_{hat}=a_2/a_1$). The initial angle between the two bubbles is 90° and the initial starting position for both bubbles are at their respect equilibrium positions based on the primary force balance for the "equilibrium" curve and at the pressure antinode for the "antinode" curve (1.71 mm). The value of Nac for bubble one at these conditions is -1.008.

Calculations similar to those done for Figure 35 and Figure 36 were done for the case of $a_1 = a_2 = 100$ µm and variable energy density. Figure 41 shows time versus initial surface to surface separation for these cases. As is expected, as energy density decreases time to collision increases.

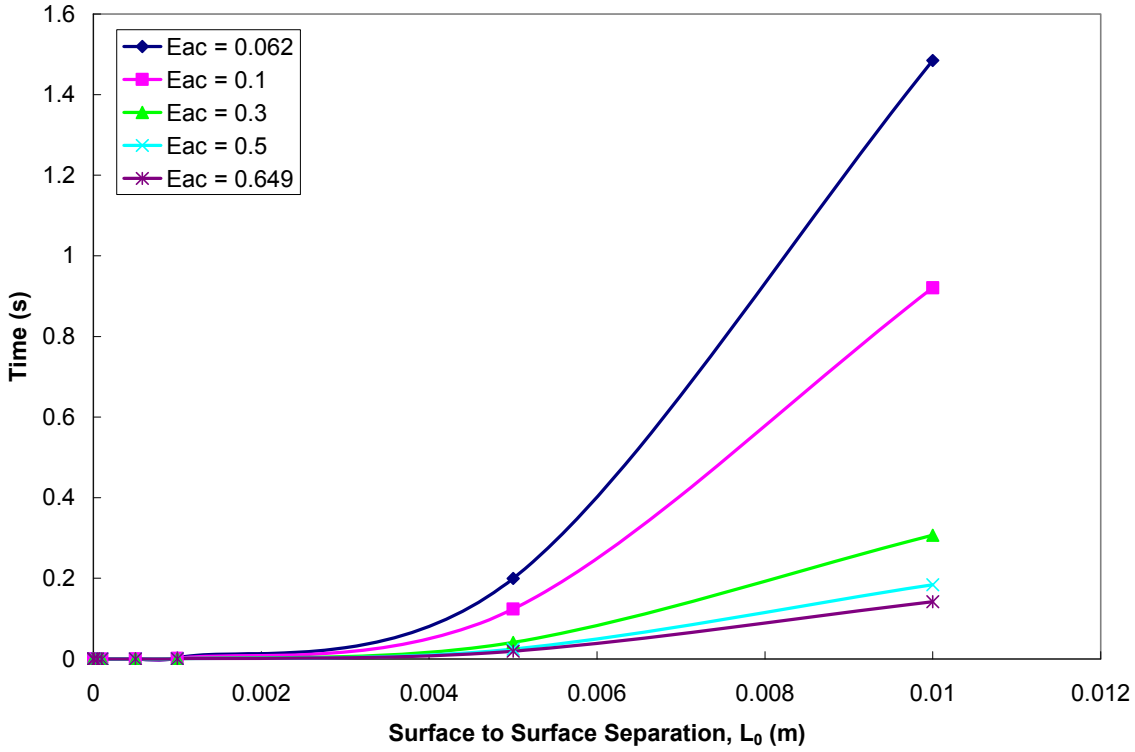

Figure 41: Time to collision based on initial surface to surface separations. The radii of bubble one and bubble two are 100 µm with the energy density (J/m^3) varying for each curve. The initial angle between the two bubbles is 90º and the initial starting position for both bubbles is at a pressure antinode (1.71 mm). The value of Nac for bubble one at these conditions ranges from -1.008 to -10.557.

Another useful concept for describing the kinetics of the collision process is that of iso-time contours. Two bubbles located within the same half-wavelength between two pressure nodes will collide due to primary and inter-bubble forces, assuming that the two

bubbles are both being driven above their resonance frequency. The critical factor is then the time to collision. To determine the collision time the location of bubble one (a_1 = 100 μm) within the acoustic chamber was held constant at its equilibrium y-position of 1.746 mm and an x-position of 0 mm. The y-position of the second bubble (a_2 = 50 μm) was also held constant, approximately at a pressure node (either 0.856 mm for $\theta \leq 90^\circ$ or 2.568 for $\theta \geq 90^\circ$). The value of θ was then varied ($1^\circ \leq \theta \leq 179^\circ$). The x-position of the second bubble was allowed to vary with θ (this also caused r to vary). Mathematica was used to calculate s and θ as a function of time, and thus the x and y coordinates for those times. The time at which the iso-time contour was desired was subtracted from the collision time to obtain the time at which the x and y coordinates were needed. Linear interpolation was then used to calculate those x and y coordinates at the desired times based on the output of Mathematica. Each curve represents the time it would take for a bubble located at the position to collide with a bubble located at its equilibrium position, slightly above the pressure antinode. The graph of this can be seen in Figure 42.

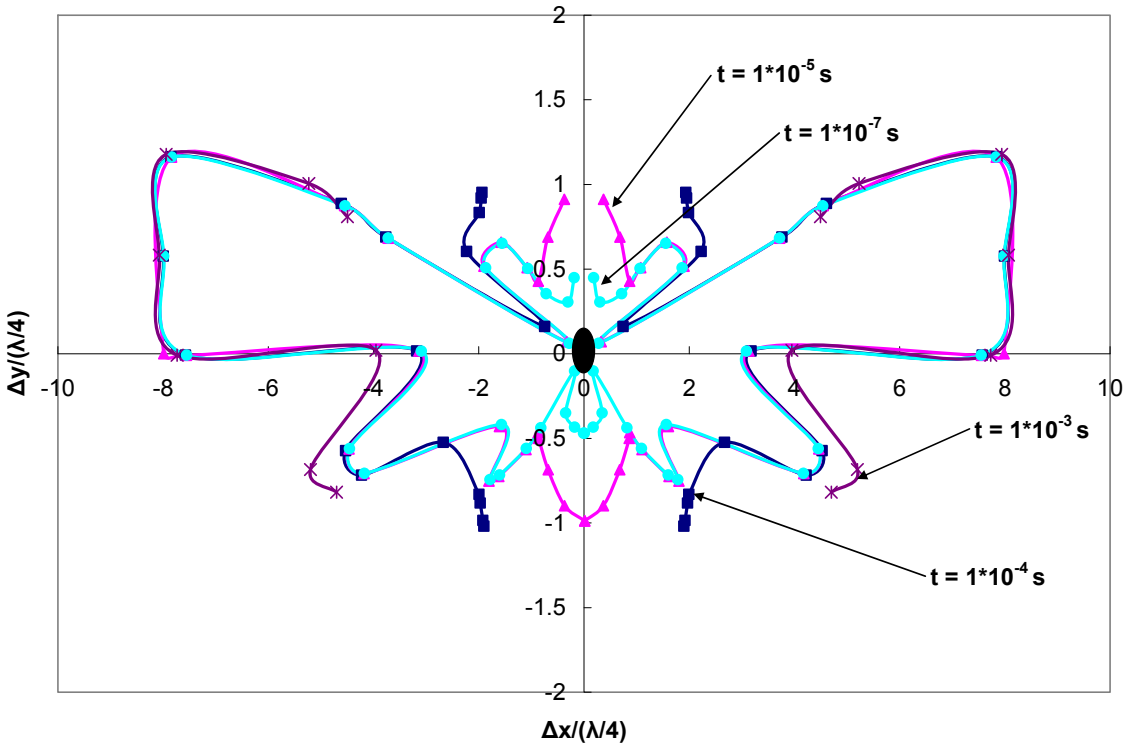

Figure 42: Iso-time contours for a_1 = 100 µm and a_2 = 50 µm. Bubble one (indicated by the black center) is at its equilibrium position slightly above a pressure antinode.

"Is it supposed to look like a butterfly?" you ask. Well, no actually. It turns out that because the collision times are so small, and because of the way the program was written, jumps in time that Mathematica may perceive as small may actually not be that small and can cause rather large discrepancies in output values. At least it's a pretty interesting looking mistake.

To counteract these issues, a collision surface was defined (at $s = 2.1$) which holds r constant for a particular set of bubbles. The initial position of bubble one was once again held constant and the position of bubble two was calculated for varying θ-values. The s and θ-position of the bubble was tracked outward, integrating backward in time to

one second ($s(t = 0) = 2.1$). Using this method, Mathematica was used to obtain x and y-values at a chosen time. These points formed the contour lines for that particular time and the curves are symmetrical across the y-axis. As can be seen in Figure 43, the iso-time contours are easier to interpret using this method.

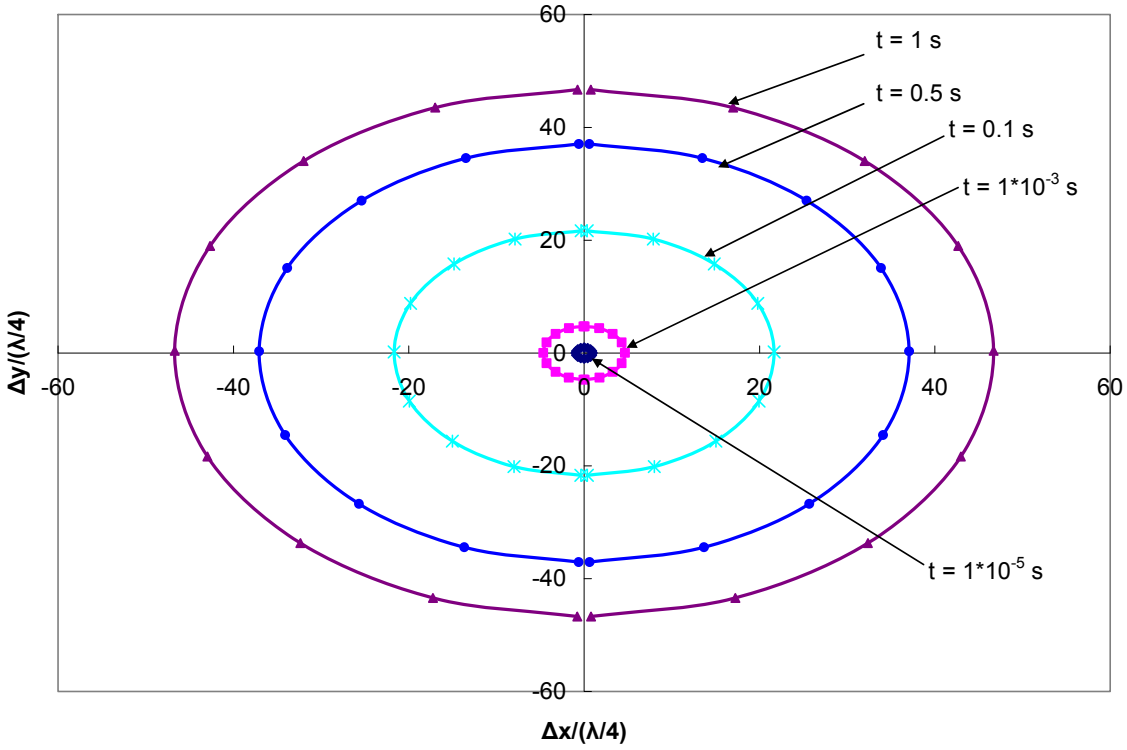

Figure 43: Iso-time contours for $a_1 = 100$ µm and $a_2 = 50$ µm. Bubble one is at its equilibrium position slightly above a pressure antinode. The value of Nac for bubble one at these conditions is -8.134.

Once again analogous calculations were run for a variety of energy densities and radii ratios. To represent all of this data together, each circle/ellipse (as seen in Figure 43) is rotated about the y-axis to obtain a sphere/ellipsoid. A basic volume integral is then completed for each sphere/ellipsoid by the disk method. Each is divided into slices

Δy thick and the area of each slice is calculated by πa^2, where a is the radius of the slice. The areas of the slices are added and the sum is multiplied by Δy to get the volume. This volume represents the volume cleared of bubbles around a particular center point; in this case bubble one. Each one of these volumes represents a point on the curves seen in Figure 44 (the dimensionless volume scales with $(\lambda/4)^3$). Each curve corresponds to a different energy density, ranging from 0.062 J/m^3 (the minimum needed to capture a bubble with a radius of 100 μm) to 0.649 J/m^3 (the maximum allowed to still assume sphericity for a bubble with a radius of 100 μm). Figure 44 shows that as energy density decreases, so does the dimensionless volume cleared, which is the expected trend. The linear nature of the curves in Figure 44 was deemed of interest. From calculations it was determined that the secondary acoustic force was most likely ruling the inter-bubble interactions. To test this theory in conjunction with the linearity of the curves, the majority of the variables in the secondary acoustic force equation were held constant, which equates to evaluating a single curve on Figure 44. Reducing it thusly results in a proportionality of the secondary acoustic to the inverse of the initial center to center separation squared, r^2. Since the secondary acoustic force is also proportional to the velocity (see equation (3.60)), the velocity can be related to the inverse of r^2. Breaking it down further shows the velocity to be approximated as the center to center separation divided by time (r/t). This leads to the time to collision being proportional to the center to center separation cubed ($t \propto r^3$). This dependency indicates a linear trend as seen in Figure 44 which signifies that the secondary acoustic force is the overriding factor in the bubble pair trajectory model, and is consistent with earlier scaling that shows van der Waals and Brownian effects to be unimportant. To make sure the linearity seen in Figure

44 wasn't only a result of the short time the previous calculations were run to, the case of a_1 = 100 μm and a_2 = 50 μm and E_{ac} = 0.5 J/m^3 was extended to a time of 10,000 seconds (approximately 2.8 hours). Once again it was shown that the trend remained linear, as seen in Figure 45. Continuing on in this theme, the dimensionless volume was graphed for very short times (correlating to small separations using the method of negative time steps described earlier) for the system of E_{ac} = 0.5 J/m^3 and $a_1 = a_2$ = 100 μm (theses radii value were chosen because hydrodynamic effects are more pronounced for larger a_2). It was shown that for small times the dimensionless volume was not linear. To represent this with the data taken out to 10,000 s, a log-log plot was produced, Figure 46. The nonlinearity at small separations shows the influence of the retarding hydrodynamic effects. The equation in Figure 46 represents a curve fit obtained from Origin 7.5, and has difficulty explaining the curve of the line at small times, but returned an R^2 value of 0.99894. Because the nonlinearity of the curve occurs for such short times, the majority of the volume cleared data can be considered linear.

It was decided to run the same calculations for the case of lower energy density (0.062 J/m^3) to determine if there was a point where primary forces and hydrodynamic effects could overtake the secondary force. Figure 47 shows an iso-time contour plot for the reduced energy density and $a_1 = a_2$ = 100 μm. Slight jogs in the curves can be seen which indicates areas where the primary acoustic force partially counteracts the secondary acoustic force. Figure 48 shows the log-log comparison plot for the two energy densities. As expected, the lower the energy density, the less the dimensionless volume cleared for a particular time.

Origin 7.5 was then used to obtain a curve fit for each line of Figure 44. The curves were fit linearly, and the lowest R^2 value returned from any of the fits was 0.99999, indicating good accuracy. The slope from each fit was plotted versus the energy density for each curve and the resultant graph is seen in Figure 49. This slope represents type of collision rate constant as a function of energy density for the case of a_1 = 100 μm and a_2 = 50 μm. By fitting this curve, the equation can be used to help find the volume cleared for other values of the energy density. The linearity of this equation is also expected. Following the same thought pattern as before, except this time both the center to center separation, *r*, and the energy density are allowed to vary. Therefore the secondary acoustic force is proportional to the energy density divided by the separation squared (E_{ac}/r^2). The proportionality of the secondary acoustic force to the velocity, and then to *r/t* results in the energy density being proportional to the center to center separation cubed over time ($Eac \; \alpha \; r^3/t$) which accounts for the linear trend in Figure 49.

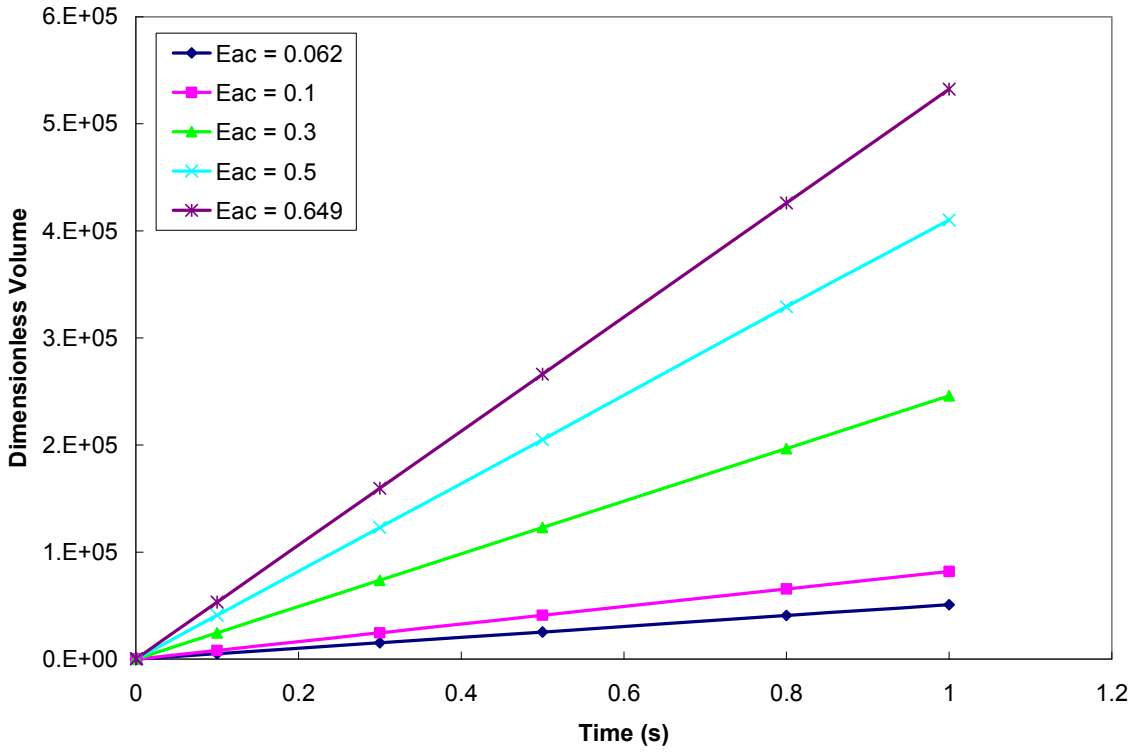

Figure 44: Dimensionless volume versus the time to clear that volume for variable energy densities (J/m^3). For this system a_1 = 100 µm and a_2 = 50 µm and dimensionless volume scales with $(\lambda/4)^3$. The value of Nac for bubble one at these conditions ranges from -1.008 to -10.557.

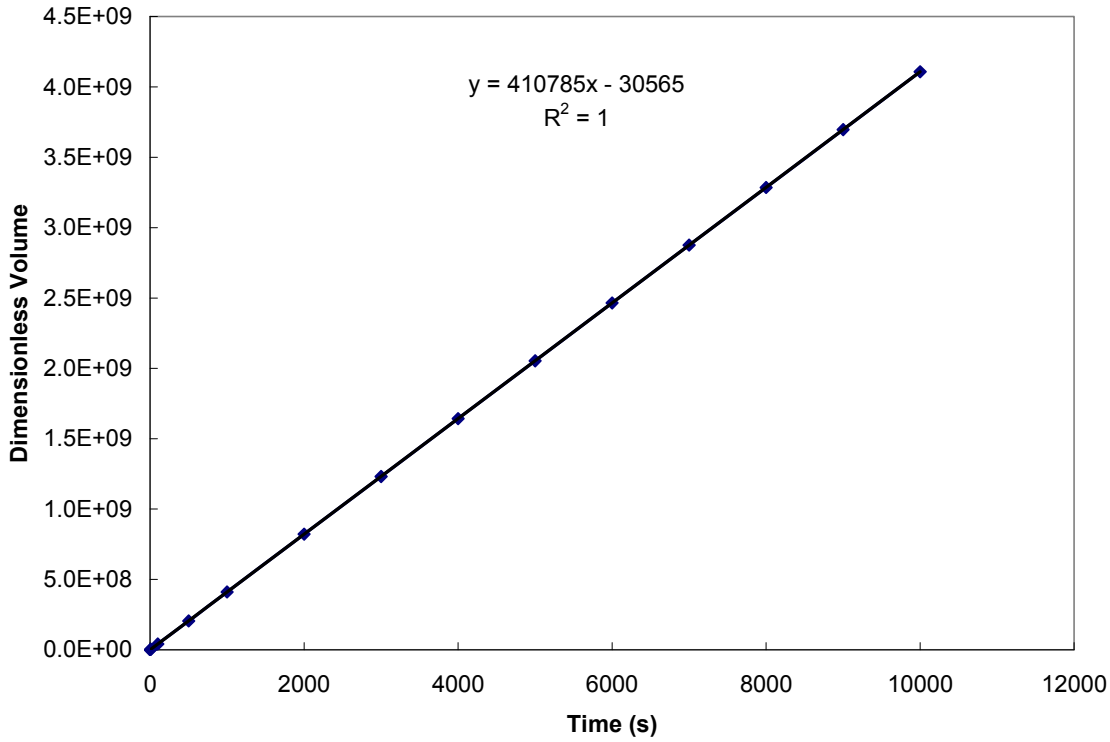

Figure 45: Dimensionless volume versus the time to clear that volume for an energy density of 0.5 J/m^3 (an extended time example for Figure 44). For this system a_1 = 100 µm and a_2 = 50 µm and dimensionless volume scales with $(\lambda/4)^3$.

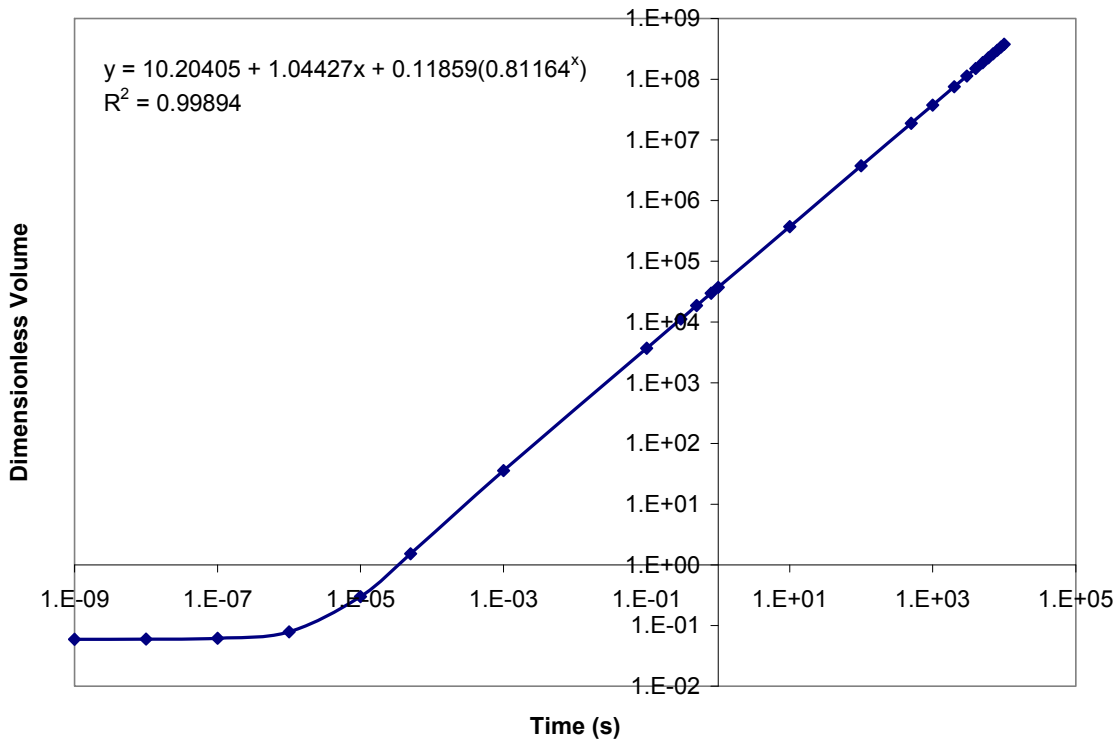

Figure 46: Log-log plot of the dimensionless volume versus time for a system with Eac = 0.5 J/m^3 and $a_1 = a_2 = 100$ µm run to 10,000 s. This shows a nonlinear behavior for small separations (small time values) resulting from hydrodynamic interactions.

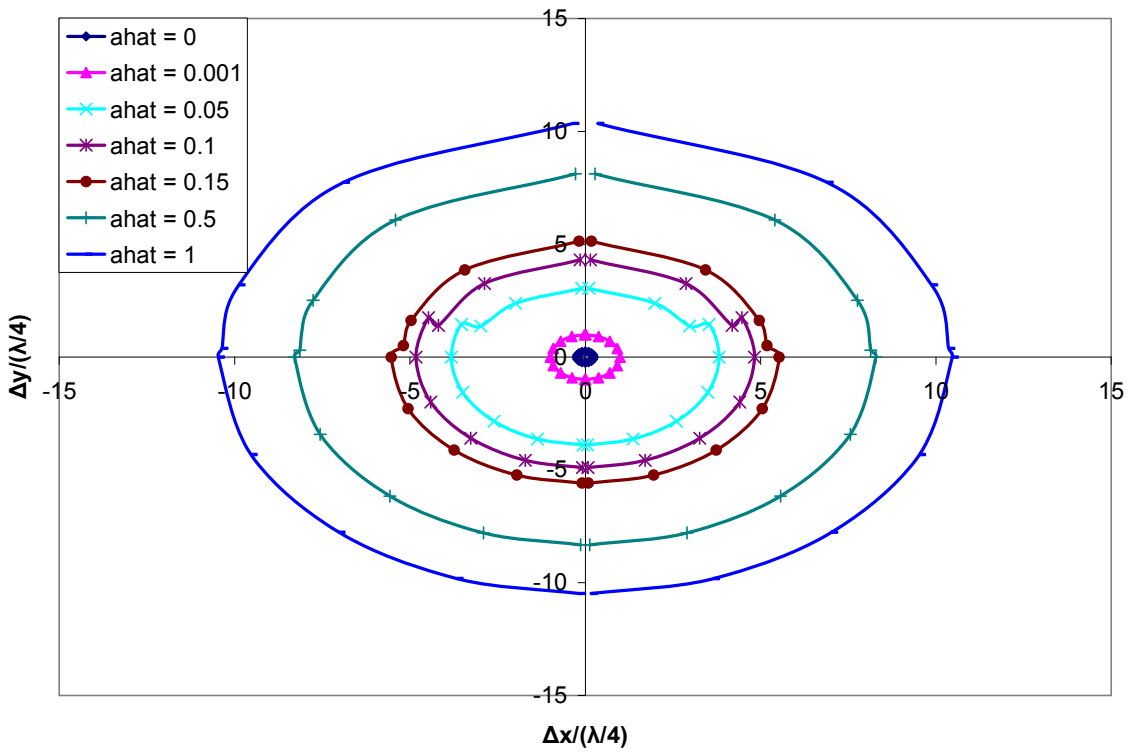

Figure 47: Iso-time contours for $a_1 = 100$, varying a_2, and Eac = 0.062 J/m^3. Bubble one is at its equilibrium position at the center. The little jogs in the curves show areas where the primary acoustic force is partially counteracting the secondary acoustic forced. The value of Nac for bubble one at these conditions is -1.008.

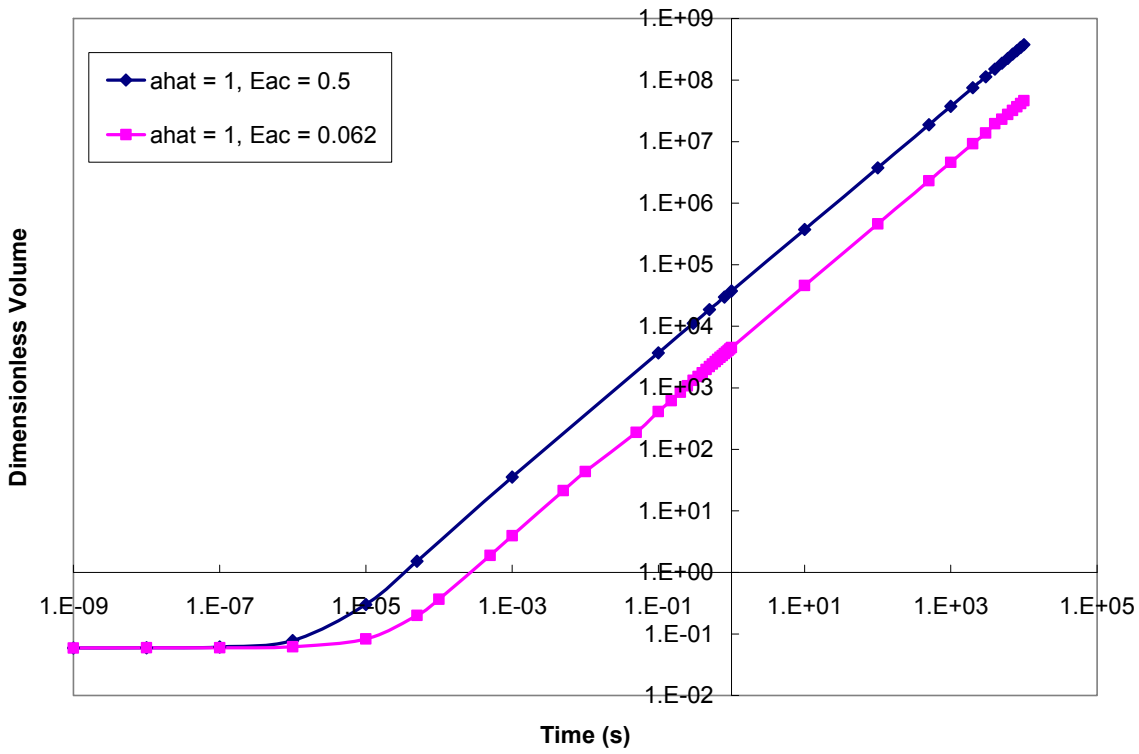

Figure 48: Log-log plot of the dimensionless volume versus time for a system with Eac = 0.5 J/m^3 or Eac = 0.062 J/m^3 and $a_1 = a_2 = 100$ µm run to 10,000 s. This shows a nonlinear behavior for small separations (small time values) resulting from hydrodynamic interactions.

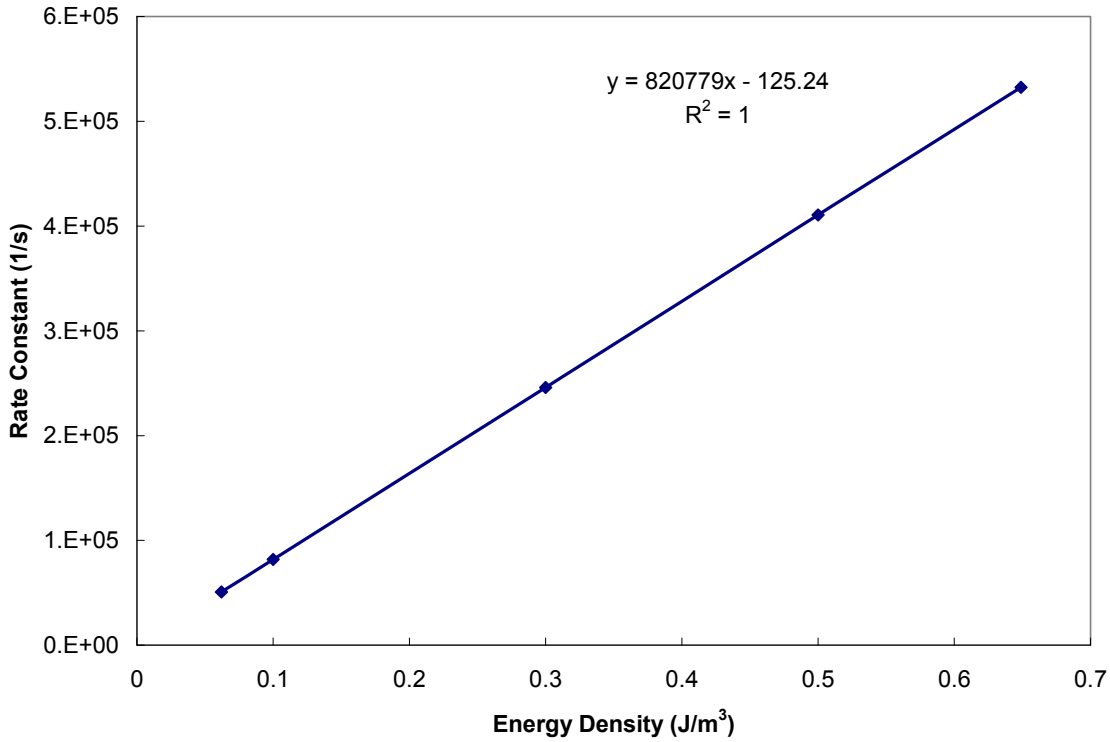

Figure 49: Slopes (1/s) from curves in Figure 44 versus energy density (J/m^3). Values on the y-axis represent a type of collision rate constant for each energy density. The value of Nac for bubble one at these conditions ranges from -1.008 to -10.557.

The graphs for the variable radii ratios were prepared in much the same way as those for the variable energy densities. Each a_{hat} was run for an energy density of 0.5 J/m^3. The radius for bubble one is 100 µm and the radius for bubble two varies from 50 µm to 100 µm. Figure 50 shows the dimensionless volume cleared versus time for variable radii ratios. The dimensionless volume cleared increases with decreasing a_{hat}, which is expected since it is easier for the larger bubble to draw other bubbles to it if they are small. The same analysis of the linear trend was considered for the variable radii ratio as it was for the variable energy density. Once again calculation run to 10,000 s showed no variation (for the case of $a_1 = a_2 = 100$ µm and $E_{ac} = 0.5$ J/m^3).

Figure 51 shows the slope from each Origin curve fit for the data in Figure 50 plotted versus the radii ratio for each curve. This slope represents type of collision rate constant as a function of a_{hat} for the case of E_{ac} = 0.5 J/m^3, a_1 = 100 μm, and variable a_2. By fitting this curve, the equation can be used to help find the volume cleared for other values of a_{hat}. Figure 52 shows the actually Origin fit graph for the curve in Figure 51 with 95% confidence bands. Though this fit isn't the best, it is the best that could be obtained from Origin's built in functions. The exponential nature of the curve indicates that though the dimensionless volume cleared decreases with increasing bubble two radius, that the trend slows with increasing bubble size. Calculating the actual dependence of the secondary acoustic force on the ratio of the radii is fairly complicated, mainly due to the monopole resonance frequency dependence on the bubble size. Hopefully the following explanations will cover the trend without becoming too specific in regards to the direct proportionality of the secondary acoustic force to other parameters. The asymptotic characteristic of the curve as the bubble approaches its resonance size is expected from the dependence of the secondary acoustic force on the monopole resonance frequency of the two bubbles and how close that frequency is to the driving frequency of the chamber ($F_{ac,2} \propto \frac{\omega}{(\omega_1^2 - \omega^2)(\omega_2^2 - \omega^2)}$). For the given conditions, the resonance radius of the bubble is approximately 48 μm. Bubbles that are closer to their resonance frequency may have a faster collision rate in part because of a correction factor included in the bubble resonance frequency calculation which correlates to a more rapid breathing mode of the bubble. This can be seen in Figure 53 for the case of E_{ac} = 0.5 J/m^3, a_1 = 100 μm, and a_2 = 100 μm. As the radius of bubble two increases, the gap between the curve with the correction factor and the curve without rapidly decreases.

Therefore the smaller bubbles have quicker collision time than larger bubbles not only because of the smaller size, but also because of the proximity of the bubble to its resonance frequency.

For both cases run to 10,000 s ((1) a_1 = 100 μm and a_2 = 50 μm and E_{ac} = 0.5 J/m^3, (2) $a_1 = a_2$ = 100 μm and E_{ac} = 0.5 J/m^3) the hydrodynamic mobility functions were also calculated. It was shown that for both cases the mobility functions (*L(s)*, *G(s)*, and *M(s)*) varied up until approximately a time of 0.2 s (which equates to short separations for calculations using a negative time step) and then all three leveled to a value of one. For the case of a_{hat} = 0.5, $0.89 \leq L(s) \leq 1$, $0.98 \leq G(s) \leq 1$, and $0.94 \leq M(s) \leq 1$. For the case of a_{hat} = 1, $0.66 \leq L(s) \leq 1$, $0.78 \leq G(s) \leq 1$, and $0.84 \leq M(s) \leq 1$. This indicates that the retarding effects of the hydrodynamic interactions are larger when the bubbles are larger, also contributing to the exponential nature of the curve in Figure 52.

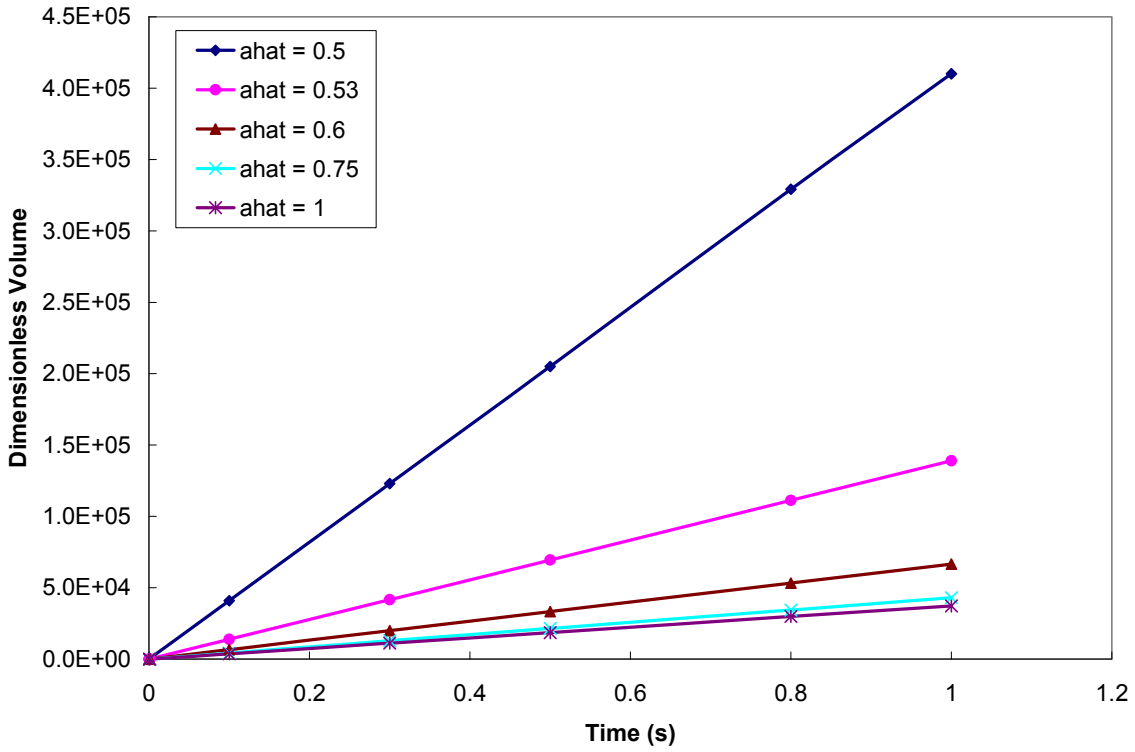

Figure 50: Dimensionless volume versus the time to clear that volume for variable radii ratios. For this system a_1 = 100 µm and a_2 varies and the energy density is 0.5 J/m^3. The value of Nac for bubble one at these conditions is -8.134.

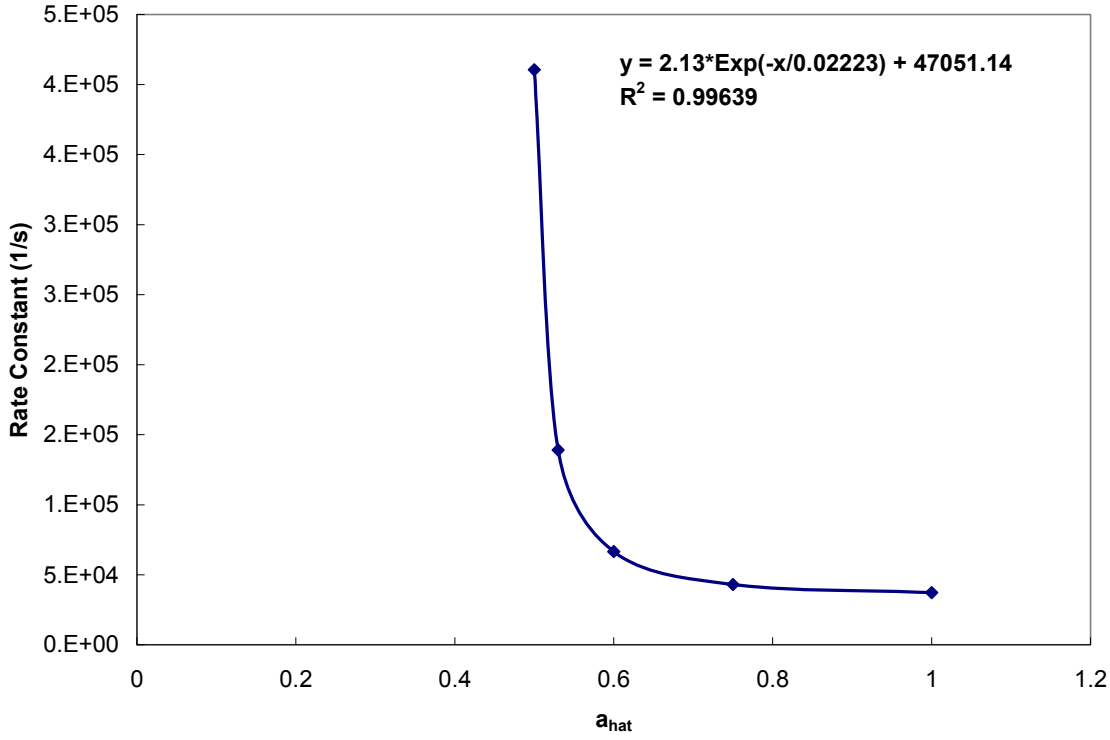

Figure 51: Slopes (1/s) from curves in Figure 50 versus a_{hat} ($a_{hat} = a_2/a_1$). Values on the y-axis represent a type of collision rate constant for each a_{hat}.

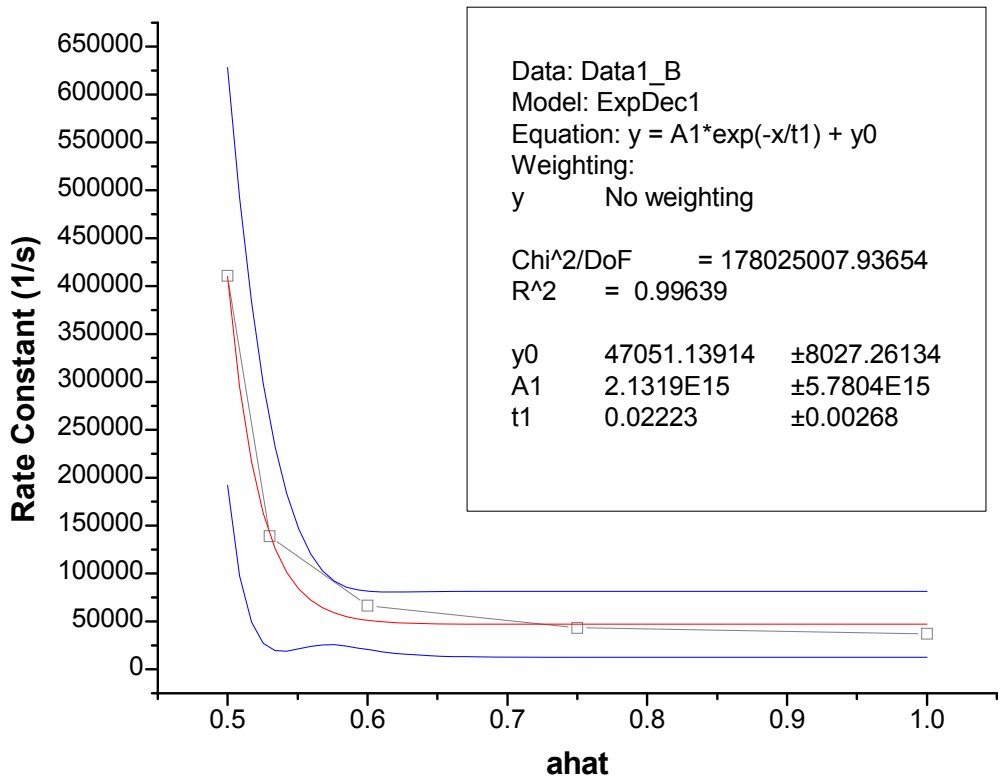

Figure 52: Origin fit graph for Figure 51 showing the original data set (black), the fit curve (red), and the 95% confidence bands (blue).

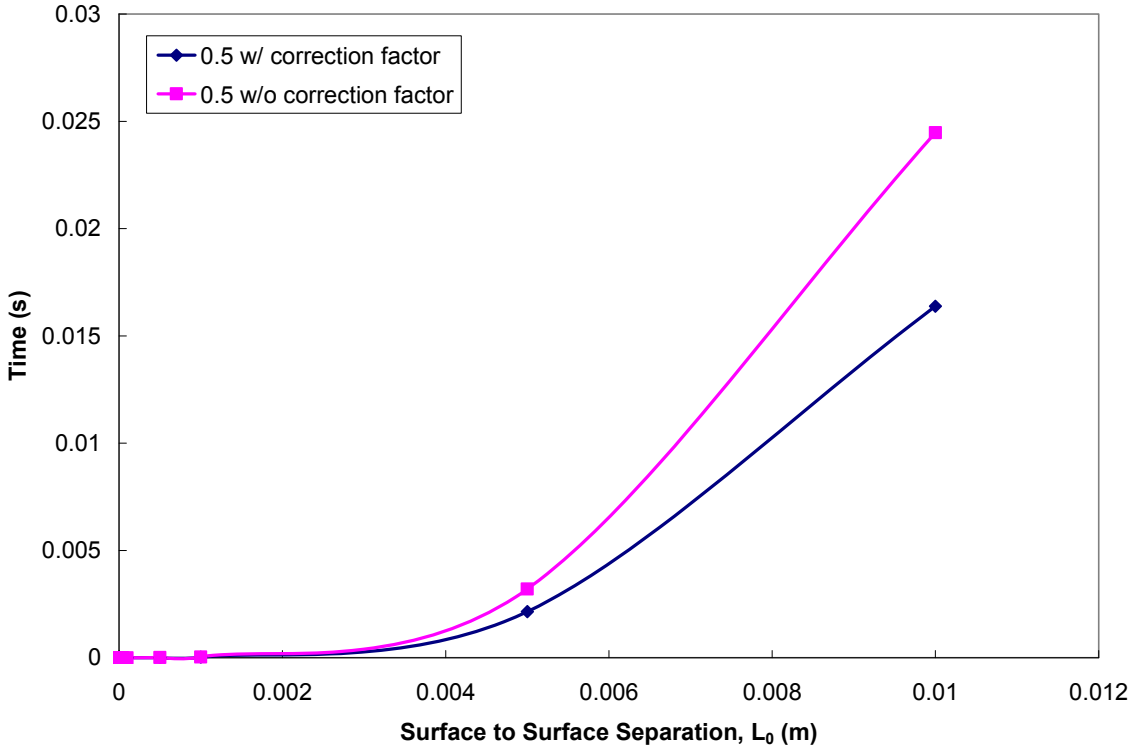

Figure 53: Time versus surface to surface separation for Eac = 0.5 J/m^3, a_1 = 100 µm, and a_2 = 50 µm. The top curve indicates the case for the resonance frequency of the bubble without the correction factor for streaming, and the bottom curve for that with the correction factor. This gap in the two curves decreases quickly as the size of bubble two increases.

4 Experimental

Experiments were run in conjunction with the modeling done to see if the paths the bubbles followed had been predicted correctly. Many of the experiments were run with swarms of bubbles that would emerge at the pressure antinodes due to the negative pressure swing of the acoustic field. Some experiments were also run with single bubbles injected with a syringe into degassed deionized water. Hydrophone measurements were also taken to help determine the acoustic energy density of the system.

4.1 Experimental Setup

The acoustic chamber design employed was a fairly simple structure. The chamber had three main sections: an acrylic chamber centerpiece, two polyethylene support structures, and a transducer and reflector. A schematic of this can be seen in Figure 54. In typical acoustic chambers, the transducers and reflectors are rigidly attached to their support structures. The disadvantage of this is that the sealant is easily fatigued which may result in leakage, and the direct connection to the support structure provides a transmission path for the acoustic energy, which can result in inefficiency in producing strong fields within the liquid itself. To counteract these issues, the chamber design used in this study incorporates a thin Latex membrane (0.02 in. thick) glued around the edges of the transducer and reflector as well as foam strips attached to the back of the latex membrane. These pieces were then sandwiched between the polyethylene support structures and the centerpiece. The latex membranes provide a resilient seal that withstands the vibrations of the transducer over long periods of

operation [132]. The acoustic chamber used was approximately 6.3 cm wide by 6.3 cm deep with a height of 5.7 cm. The transducer (EC-64 by EDO) was 3.8 cm by 3.8 cm with a thickness of 5.08 mm. The reflector was glass and was also 3.8 cm by 3.8 cm with a thickness of 2.23 mm. The transducer and reflector were set approximately 2 cm apart within the chamber.

The signal to the transducer was acquired by utilizing a Fluke 6011A Synthesized Signal Generator (also used was an HP 3325A Synthesizer/Function Generator) attached to an ENI Model 240L RF Power Amplifier. The output signal was then run through a Clarke-Hess Model 2335 Sampling Wattmeter before being transferred to the transducer. The sampling wattmeter allowed for the monitoring of the signal as both frequency and voltage modifications were made. A quantity called the power factor was observed to determine how ideally the system was utilizing the input signal. The closer the power factor was to one, the greater the efficiency of the system at transforming electrical energy into acoustic energy. This value was also used to help tune the system. The frequency was varied to obtain a value of the power factor as close to one as possible.

After the system was electronically hooked up, water was pumped into the chamber using a Cole-Parmer Masterflex Model 7520-00 peristaltic pump. Once the chamber was filled the inlet and outlet ports were sealed. A digital camera, UNIQ UP-930 Progressive Scan CCD Camera, was used to capture images and video to a computer throughout the experiment. A Minolta MD 50 mm lens (1:1.7 ratio) was used for distance images and a Nikon AF Micro Nikkor 60 mm lens (1:2.8 ratio) was used for close-up pictures. The computer imaging software used was EPIX PIXCI D2X. A full schematic of this experimental set-up can be seen in Figure 55.

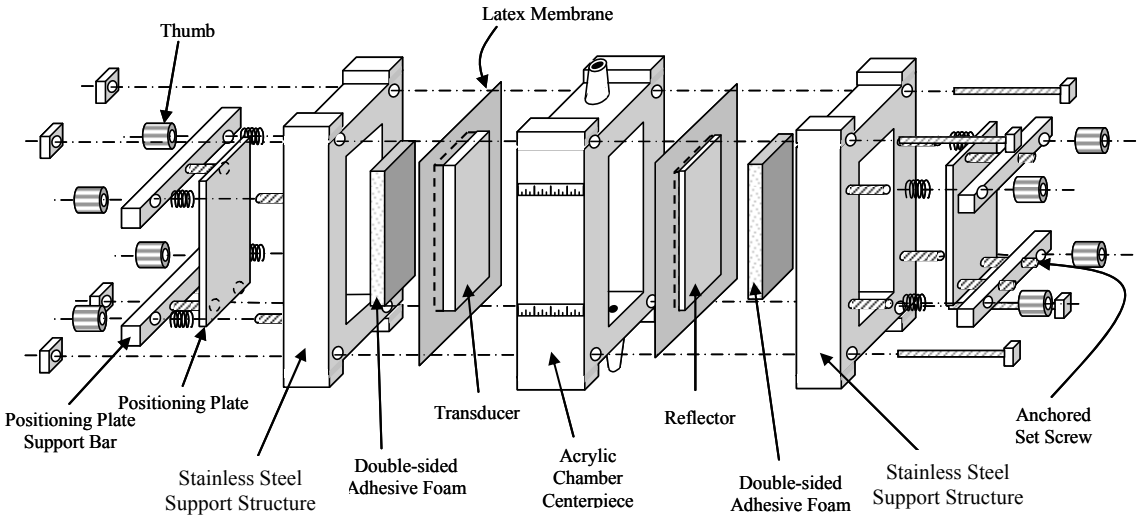

Figure 54: Schematic representation of the acoustic chamber used for experimentation. The transducer and reflector are held in place by double-sided foam attached to an adjustable positioning plate. The fluid suspension flows through the centerpiece, where, upon assembly, an airtight seal is created between the polyethylene support structures, the latex membranes glued to the transducer and reflector, and the chamber centerpiece [132].

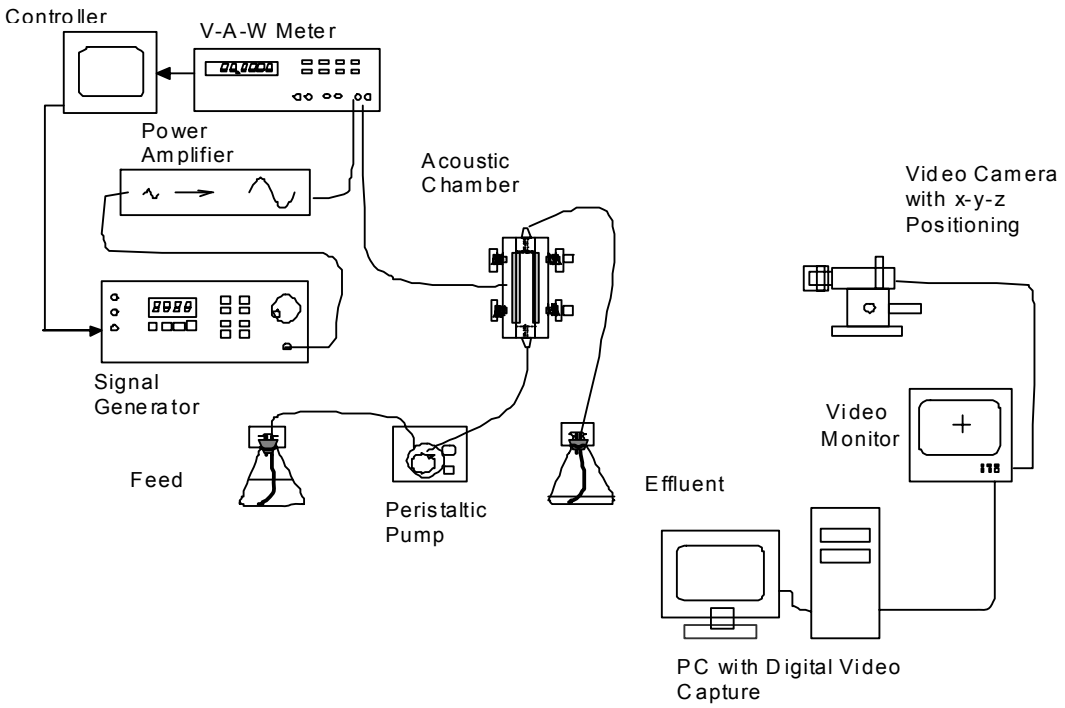

Figure 55: Schematic of experimental setup [5].

When conducting single bubble experiments, the acoustic chamber was filled with degassed deionized water. The water was degassed using a combination of stirring and vacuum pumping, using a Welch 1400 DuoSeal Vacuum Pump. One port of the acoustic chamber was sealed with a septum plug to allow insertion of a needle. The syringes used for these experiments were the Hamilton 7000.5 0.5 µl (26s gauge needle, 1.71 in. in length, HP type tip) or the Hamilton 7001 1 µl (25s gauge needle, 2.75 in. in length, type 2 tip). Swarms of bubbles were achieved by simply degassing the water to a lesser extent or not at all. When running the transducer at high intensities, dissolved gas was drawn out of solution due to the negative pressure swings at the acoustic pressure antinodes within the chamber, and large numbers of bubbles were formed. The normal operating conditions of the chamber were 0.435 MHz and about 30 V p-p.

4.2 Images

Initial images obtained showed both that the bubbles could be banded and that they would rest approximately at the pressure antinodes. Figure 56 shows that the system works well for swarms of bubbles as the bubbles move readily to pressure antinodes where they form distinct bands. Figure 57 shows a picture taken of two bubbles and the distance that they rest from each other. In this instance, the transducer was being operated at 0.55 MHz and 30 V p-p, so the antinodes can be approximated as 1.355 mm apart when calculated by the half wavelength method. The image shows the bubbles to be approximately 1.32 mm apart. Although there are some intrinsic errors in the measurement process, mainly through human error, this is a good indication that the system is working as predicted. It was shown that the majority of the bubbles could remain trapped for up to an hour. Experiments longer in length than an hour were not run.

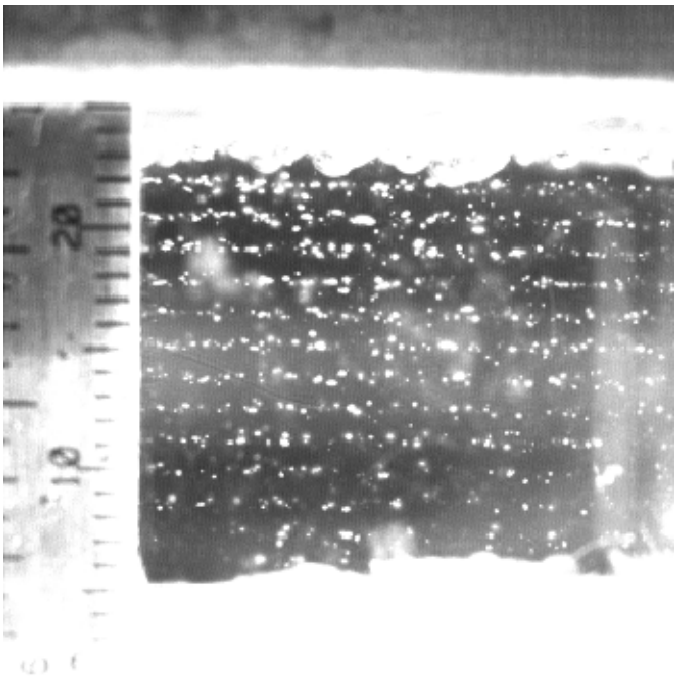

Figure 56: Entrapment of swarms of bubbles in multiple, parallel bands. Chamber operating conditions were 0.55 MHz and about 30 V p-p.

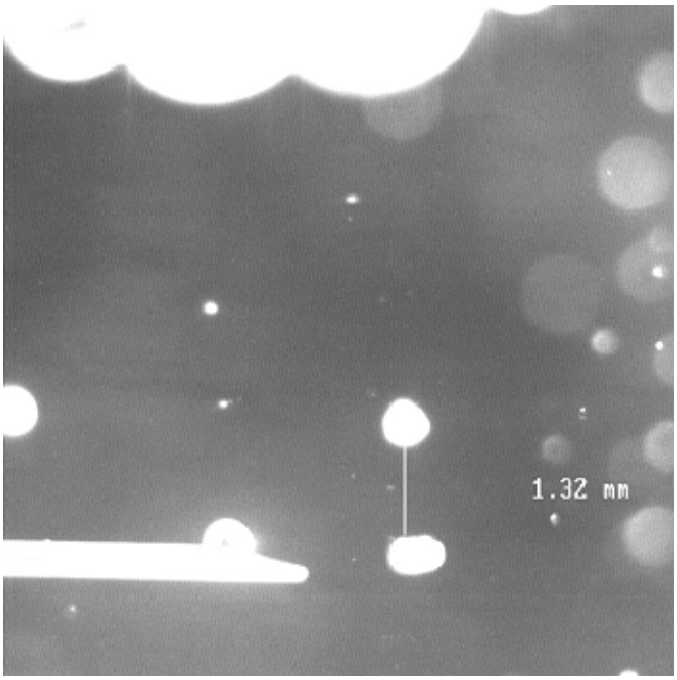

Figure 57: Image of air bubbles in water resting at pressure antinodes within the acoustic chamber. The distance between bubbles is 1.32 mm. Chamber operating conditions were 0.55 MHz and about 30 V p-p.

Initially it was thought that there was some coalescence and subsequent release of the newly enlarged bubbles once a threshold size was reached, but further study showed that this was not necessarily the case. Higher magnification showed bubbles that were initially thought to have coalesced were simply attracted together and had formed bubble clusters. The bubbles initially formed long chains as seen in Figure 58(a). There were three further common bubble formations seen. The first was a "planet" type formation seen in Figure 58 (b). The next two were variations on the planet cluster, and were the "comet" type formation and the "cyclone" type formation seen in Figure 58 (c) and Figure 58 (d), respectively.

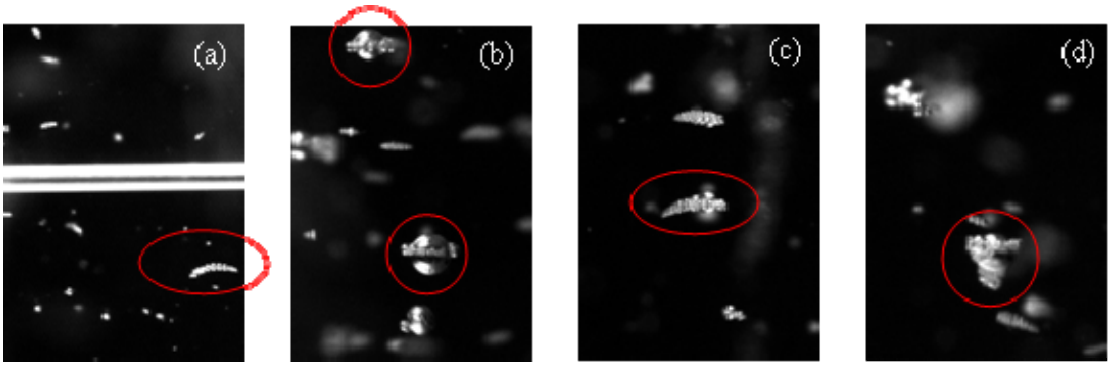

Figure 58: (a) Initial long chain bubble formation, (b) planet type bubble formation (large top bubble approximately 400 µm in diameter, large bottom bubble approximately 550 µm in diameter), (c) comet type bubble formation (large bubble approximately 300 µm in diameter), (d) cyclone type bubble formation (large bubble approximately 500 µm in diameter).

It is thought that the particular bubble formations may be more prevalent in certain areas within the chamber where "hot spots" may occur. Hot spots result from

non-uniformities in the transducer which results in a force perpendicular to the primary acoustic force. But this is difficult to confirm from experiments. Often the case of mother/daughter bubbles is seen [100], as mentioned in the literature survey section, and this helps to increases cluster size. Video taken shows smaller daughter bubbles being transferred in a stream from the mother bubbles to a neighboring bubble due to secondary acoustic forces.

The suggestion was made that perhaps electrostatic forces were preventing the bubbles from coalescing, hence inducing the clustering phenomenon. To this end sodium chloride was added to the DI water (1.05 g NaCl into 400 ml DI H_20). The acoustic chamber was run at the normal frequency of 0.435 MHz and a voltage of 57 V p-p. A power factor of 0.986 was observed indicating the chamber was operating correctly (values of the power factor on in the range of 0.9 – 0.99, with one being the maximum, were typical for the DI water/air system). At these conditions no bubbles were observed to form. The voltage was gradually increased, still with no bubbles appearing. Eventually the voltage reached a value of approximately 118 V p-p. At this point the water had heated to the point where experiments couldn't continue. The addition of the salt lowers the chemical potential of the water. Also, the solubility of oxygen in salt water is lower than that in DI water, which would indicate the addition of salt should cause the gas bubbles to emerge more readily from the water. The addition of salt was done prior to pumping the water into the acoustic chamber, which points to the dissolved gas escaping into the surroundings. Future experiments should involve salt water being injected into an acoustic chamber already filled with DI water to prevent this problem.

Figure 59 shows the collision of two bubbles inserted into the chamber using a GC syringe with a 26s gauge needle. The needle was dipped in 5.5 % Tecophilic polyurethane in chloroform then allowed to dry. This provided a hydrophilic coating which was necessary because previous experiments showed bubbles adhering to the needle instead of releasing. For this experiment the DI water was degassed prior to use. The top bubble has a radius of 182 μm and the bottom bubble has a radius of 233 μm and the transducer was run at a frequency of 0.435 MHz and a voltage of 33 V p-p. In the first picture of the series, the two bubbles have a surface to surface separation of approximately 3 mm. If this picture series is compared to Figure 34 (though Figure 34 should be flipped to get the correct approximate angle), the movement of the two bubbles in Figure 59 correspond to the path shown in Figure 34 fairly well. The initial surface to surface separation for Figure 34 is 5 mm which is close enough to the initial surface to surface separation of 3 mm for Figure 59 to allow for an approximate comparison. Though the measurements show that the smaller bubble is the top bubble and the larger bubble is the bottom bubble, thus indicating that the top bubble should move down to the bottom bubble, the intrinsic error in measuring something this small may have resulted in incorrect radii values. The bubbles are most likely approximately equal in size, possibly allowing for the top bubble to remain stationary while the bottom bubble moves up toward it. Of course for the case of equal sized bubbles the top bubble should move toward the bottom bubble as well as the bottom bubble moving toward the top. Part of this issue may result from streaming from the syringe. But the most likely reason is that the top bubble is not only sitting at a pressure antinode, but is also sitting at a hot spot (hot spots result in a force perpendicular to the primary acoustic force). This would

increase the primary type forces it is experiencing (holding it stationary) without increasing the primary force the bottom bubble is initially experiencing. Figure 60 shows much the same thing as Figure 59 but with two bubble clusters colliding. The radius of the larger bubble in the top cluster of Figure 60 is approximately 500 µm and the initial separation distance between the two tips of the clusters that collide is 1.4 mm.

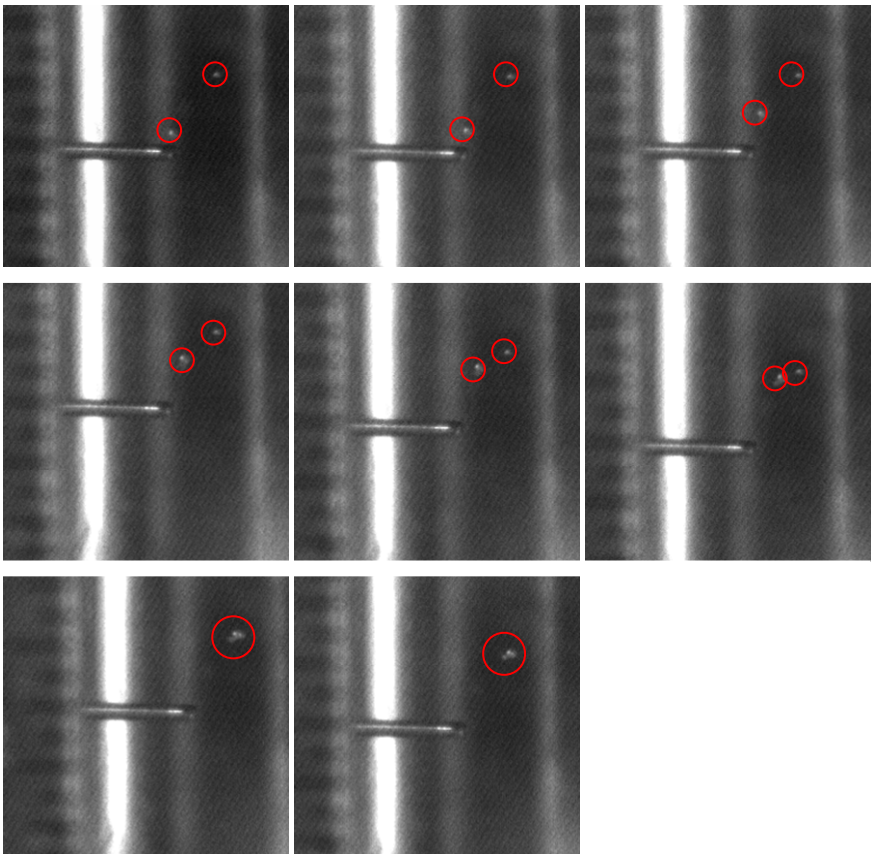

Figure 59: Bubble collision pictures. The radius of the top bubble is about 182 µm and the radius of the bottom bubble is about 233 µm. The frequency and voltage for this experiment was 0.435 MHz and 33 V p-p and the initial surface to surface separation of the two bubbles is approximately 3 mm.

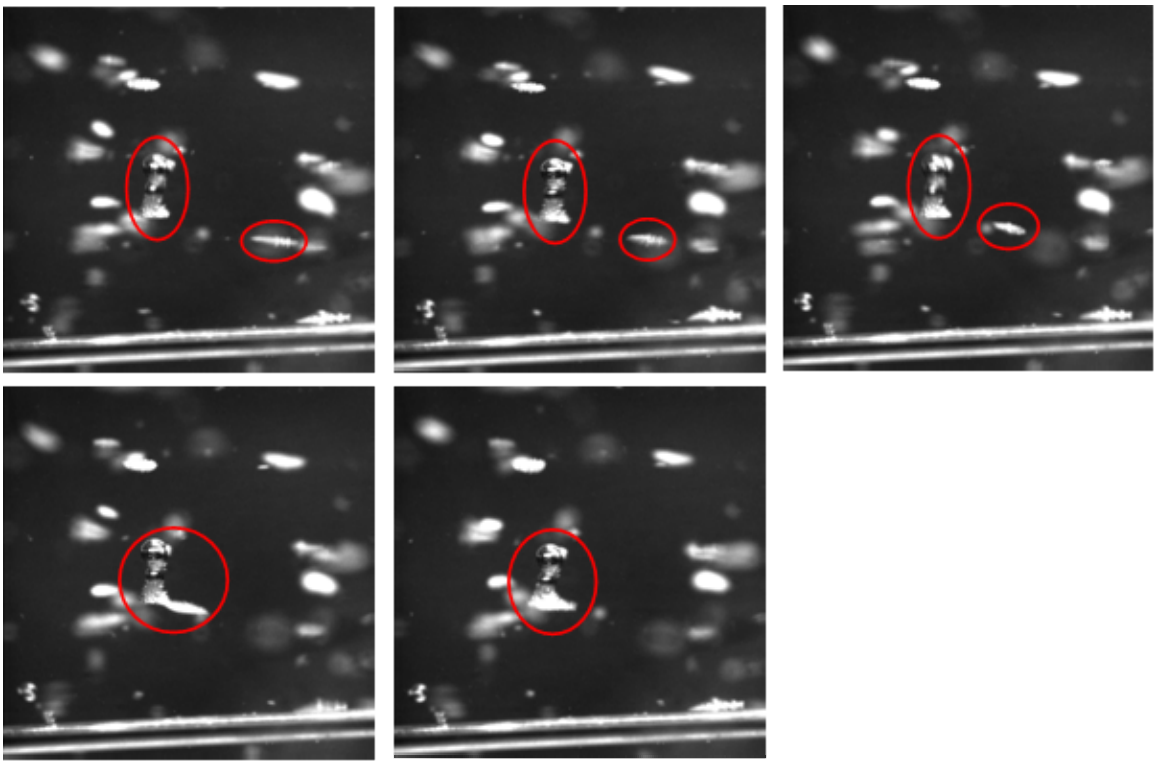

Figure 60: Bubble collision pictures. The radius of the larger bubble in the top cluster is 500 µm. The frequency and voltage for this experiment was 0.435 MHz and 33 V p-p and the initial tip to tip separation of the two bubbles is approximately 1.4 mm

4.3 Hydrophone

To determine the pressure in the acoustic chamber, and thus the average energy density of the system, a hydrophone was utilized. The hydrophone allowed voltage measurements to be taken throughout the system, which can be converted to pressure measurements. These pressure measurements can then be averaged and used to calculate the average energy density throughout the system using $P_s = \sqrt{2\rho_l c_l^2 E_{ac}}$. The hydrophone used was an Onda HNR-0500. A preamplifier (Onda AH 17DB) was also used because the voltage in the fluid was so low. Multiple runs were taken to try to determine how uniform the pressure was throughout the system. For these measurements

the transducer was operated at 0.435 MHz and 16 V p-p. The acoustic chamber was placed on its side so the transducer and reflector were horizontal to each other. Figure 61 is a graph of three runs taken at a depth of about 2 cm and a distance from the side of the chamber of about 2 cm, which puts the hydrophone approximately at the center of the transducer. The hydrophone was then moved micron distances at a time to starting at the transducer (zero point) and ending at the reflector. The voltage readings were monitored as the hydrophone was moved, and measurements were taken at high and low points as well as a few points in between. The voltage was observed and measured with a National Instruments PCI-5102 card with a 5 V p-p and 20 MHz maximum. The software used was National Instruments Scope-SFP (software included with PCI-5102 card).

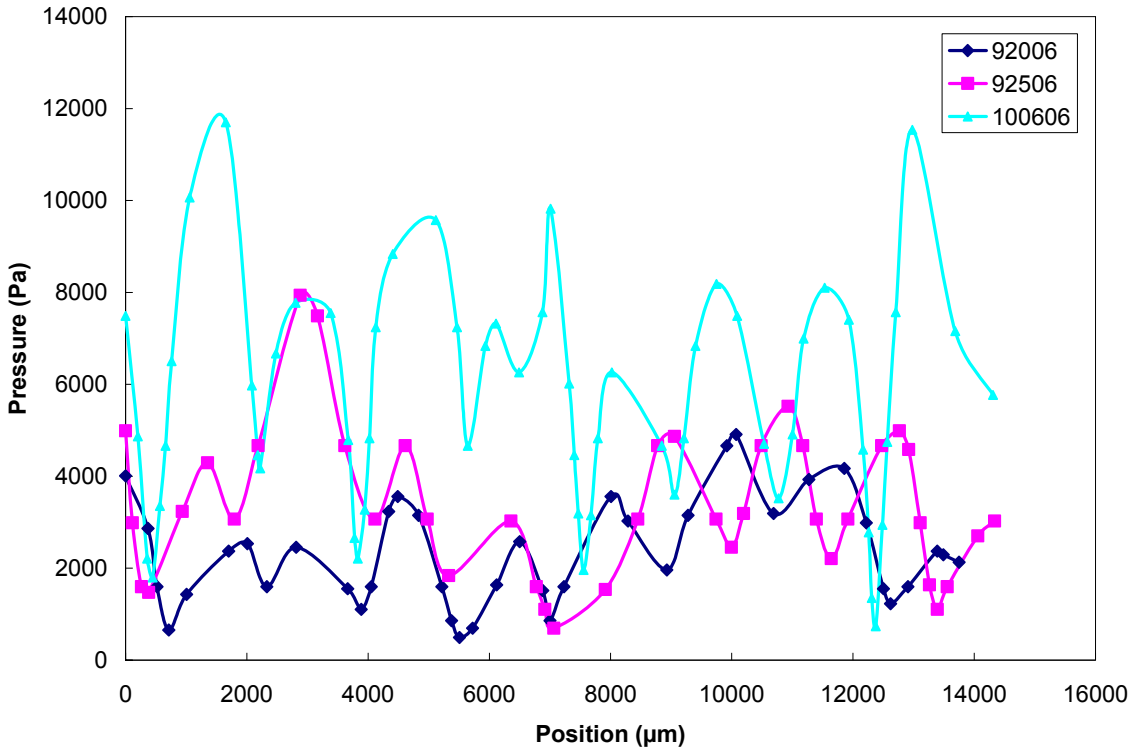

Figure 61: Hydrophone pressure measurements taken in the acoustic chamber with the zero point being the transducer. Measurements were taken at a frequency of 0.435 MHz and 16 V p-p. Curves are labeled based on the day the data was taken. This will correlate to data shown in Table 1.

After taking the voltage measurements, the pressure was calculated using a calibration chart supplied by the company. The pressure was then averaged and used to calculate the average energy density in the chamber. Table 1 shows a summary of this for the three runs shown in Figure 61. The average distance between antinodes is close to the distance that was calculated by the half wavelength method, which is an indication the system is operating as expected. As can be seen, the energy density is about two orders of magnitude lower than that needed to assume a spherical bubble, 0.649 J/m^3 as seen in Figure 9. Unfortunately, the energy density is also about an order of magnitude too low for capture (minimum energy density previously determined to be 0.062 J/m^3 based on the primary force balance). The voltage supplied to the transducer for these experiments were about a factor of two lower than that normally used for capturing images. Since pressure is proportional to voltage and the energy density is proportional to the pressure squared, by doubling the voltage being fed to the transducer (to increase it from the 16 V for the hydrophone experiments to the 30 V most often used for capturing images), the energy density can be multiplied by a factor of four to get a more accurate value for normal operating conditions. Even doing this puts the energy density readings a bit low to assume capture, especially considering the ease at which the bubbles were viewed to be captured within the chamber indicating a higher energy density than measured. One possible explanation is that the hydrophone could have become un-calibrated through use. The most probable explanation, though, is that the open chamber experiment (which is necessary for scanning experiments) alters the pressure in the chamber from that when running it closed. So the hydrophone measurements should be

used mainly for the purpose of locating the pressure antinodes in the system, as opposed to measuring the average energy density in the chamber.

Table 1: Energy density and distance between antinodes based on hydrophone data.

Date	Average Pressure (Pa)	Energy Density (J/m3)	Half λ (μm)	Average Distance Between Antinodes (μm)
92006	2382	1.28E-03	1713	1686
92506	3439	2.67E-03	1713	1792
100606	5672	7.26E-03	1713	1700

4.4 Verification of Bubble Pair Model

To determine if data returned from the bubble pair trajectory model could accurately predict movement of bubbles in experiments, video was obtained of actual bubble motion within the acoustic chamber. Since the hydrophone proved inaccurate in experimental measurement of energy density in the chamber, the model was run at decreasing values of the energy density until an approximate match was obtained. For each energy density the equilibrium resting position of bubble one was calculated using the primary force balance. The primary force balance was also used to calculate the minimum energy density needed to effect capture for each bubble size. Bubble one and bubble two were measured to be within one or two pixels of each other, and thus assumed to be the same size. The average of the two measurements was taken and for Figure 62 $a_1 = a_2 = 117$ μm. The dip shown in the experimental data as bubble two approaches bubble one is commonly seen in experiments and can possibly be attributed to "cold spots" within the chamber (opposite of hot spots indicating dead areas of the transducer).

A more likely possibility is that bubble one could be shielding the reflected acoustic wave coming back from the reflector, which is located at the top of the chamber.

Also, Figure 62 shows that varying the energy density changes the path of the bubbles to a very minor degree. What does change, though, is the time to collision which is represented in Figure 63 for a variety of energy densities. This trend is expected because, once again assuming the secondary acoustic force is the main controlling force, the time to collision is proportional to the inverse of the energy density ($t \propto 1/Eac$). The curve was fit using Origin 7.5 and the equation represented on the graph was then used to calculate the energy density of the experimental system based on the frame rate of the video captured. For this example, the bubbles collided in six frames and for a frame rate of 30 frames/s and collision time of 0.2 +/- 0.03 s is obtained. Using this time with the fitted equation for Figure 63, an energy density for the system of 0.084 +/- 0.177 J/m^3 was calculated.

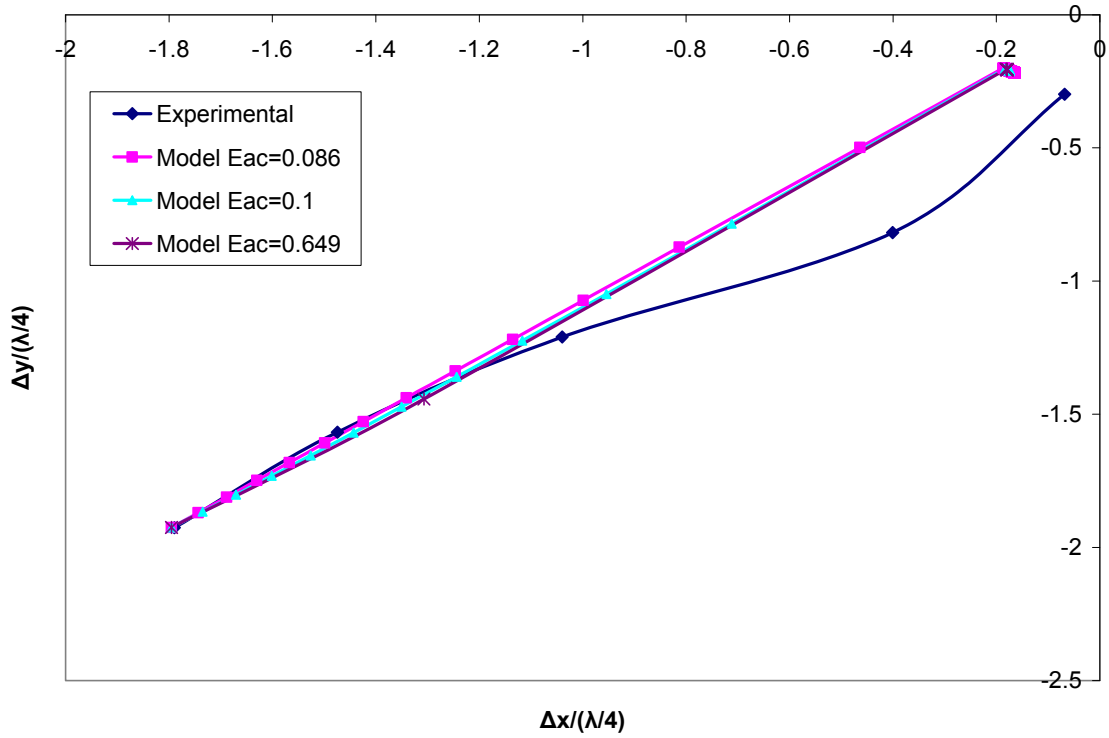

Figure 62: Comparison of experimental data to calculated results from the bubble pair trajectory model for the case of $a_1 = a_2 = 117$ µm.

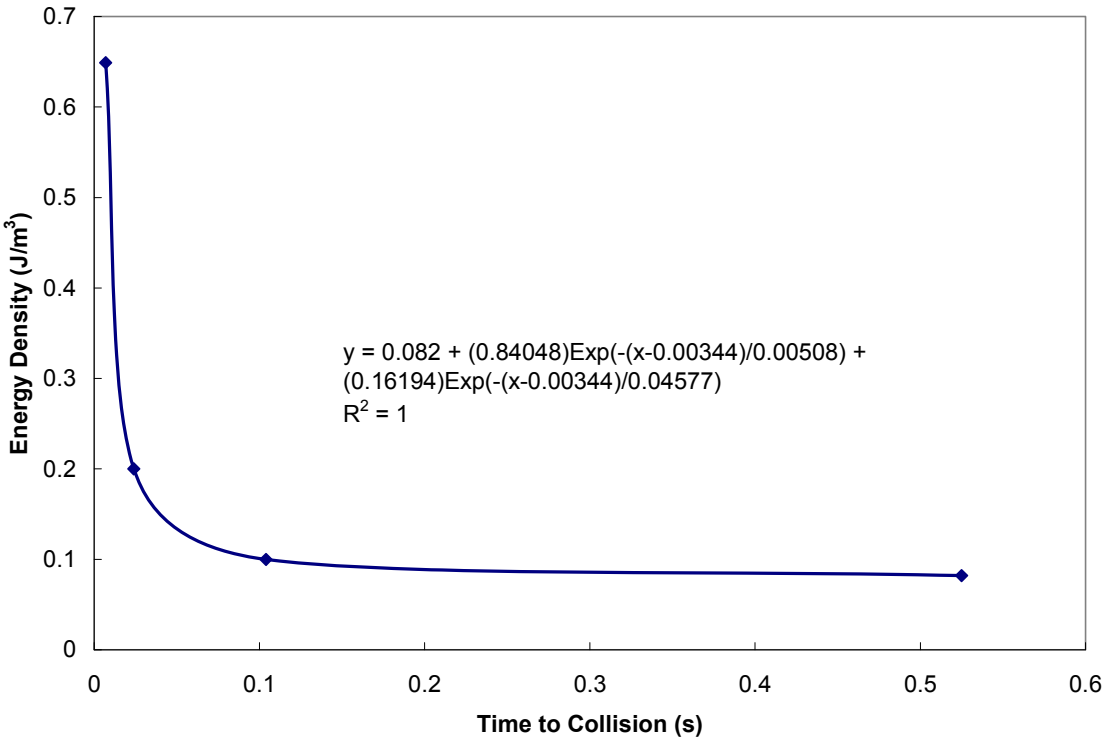

Figure 63: Energy density versus time to collision for the experimental case seen in Figure 62. From this curve the energy density can be determined based on the collision time calculated for the experimental data from the frame rate of video being taken.

A second similar case was run under the same experimental conditions but with $a_1 = a_2 = 132$ μm, seen in Figure 64. The extra swoop, or the portion of the experimental trajectory that is near collision, for the minimum energy density curve is most likely a result of the primary acoustic force trying to push the second bubble to its equilibrium position. It is possible that this would be seen in the other curves if the collision shell around bubble one was made smaller. Again the same trend of decreasing collision time with increasing energy density is seen and Figure 65 shows the energy density versus the collision time. Based on a collision sequence of five frames, and thus a collision time of 0.167 +/- 0.03 s, an energy density of 0.12 +/- 0.216 J/m^3 was calculated using the fit

equation seen in Figure 65. The two cases were for the same operating conditions and this gives a difference of about 30%, which is a fairly decent agreement. It should be noted that due to the nature of the acoustic chamber design, inserting bubbles at different angles is not easily accomplished, so examples for other angles were not obtained.

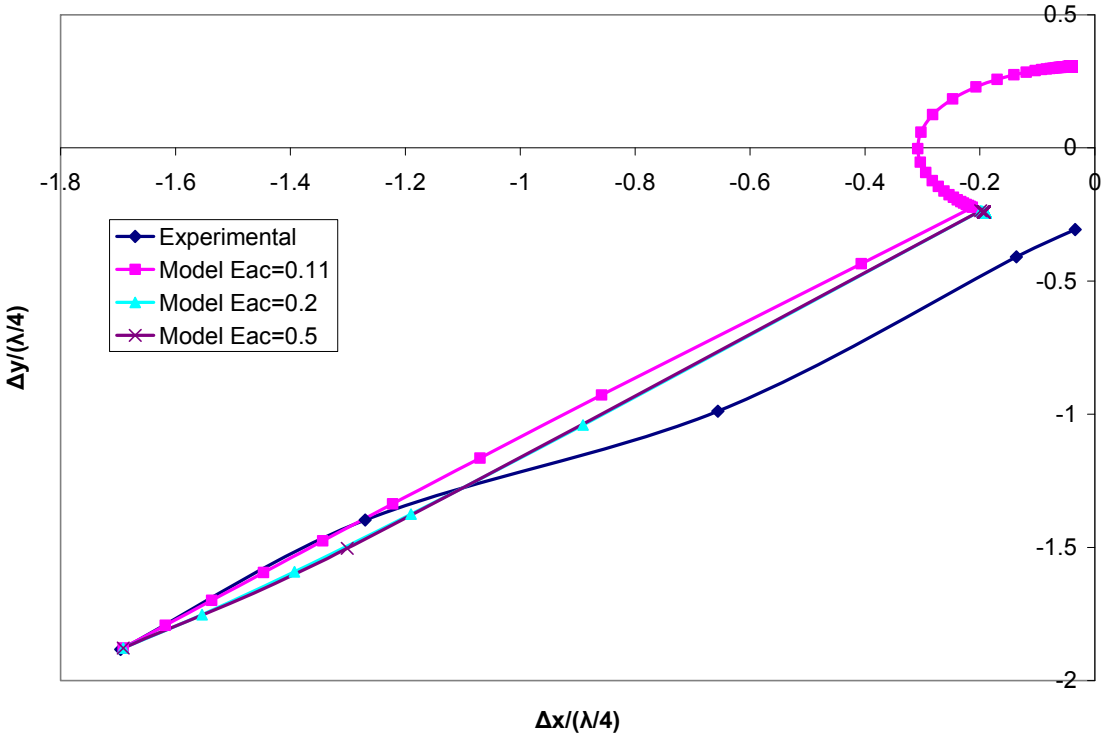

Figure 64: Comparison of experimental data to calculated results from the bubble pair trajectory model for the case of $a_1 = a_2 = 132$ µm

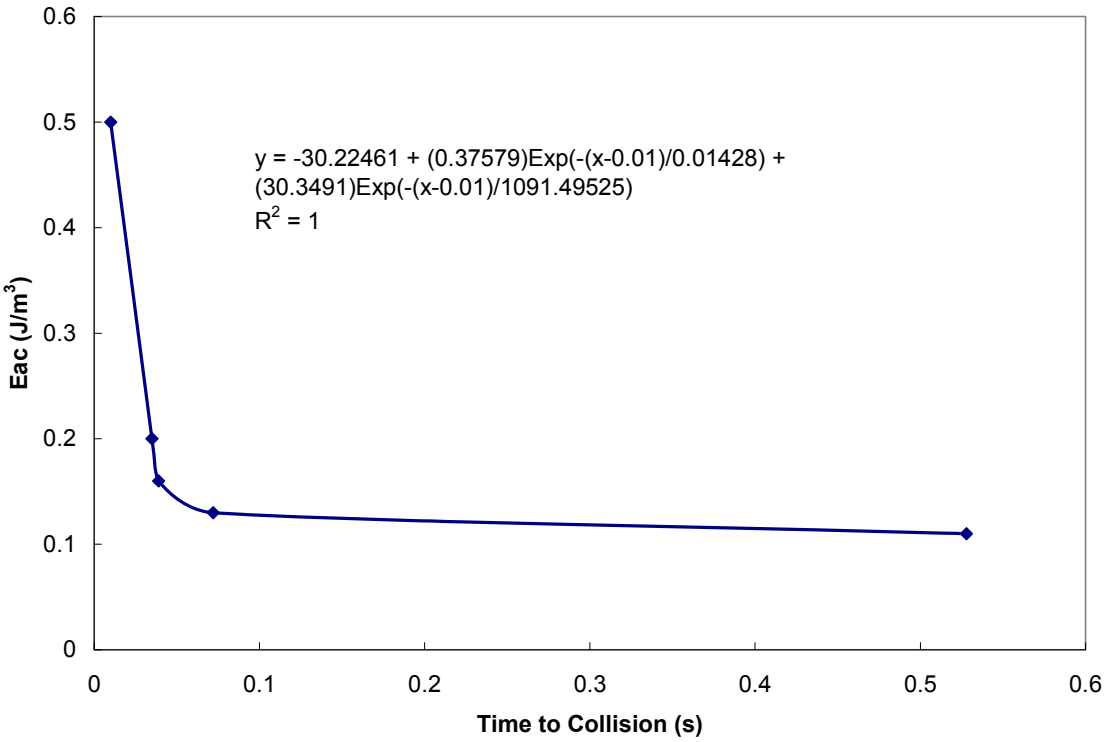

Figure 65: Energy density versus time to collision for the experimental case seen in Figure 64. From this curve the energy density can be determined based on the collision time calculated for the experimental data from the frame rate of video being taken.

5 Conclusions and Future Work

5.1 Summary

The main objective of this research was to develop a fundamental understanding of the effect of forces induced by resonant ultrasonic fields on the entrapment and coalescence phenomena of gas bubbles in a liquid. This included modeling efforts to illustrate the relationship between the size of bubbles, their sphericity, acoustic field parameters (frequency and intensity), bubble equilibrium position relative to acoustic pressure antinodes, and the bubble coalescence phenomena. It also included experiments involving both small numbers of bubbles and large swarms to test the basic predictions of the model. These tasks were accomplished by the derivation and experimental verification of the bubble pair model which determined the path and collision rate for bubbles starting at designated locations within the acoustic chamber.

Initial calculations were done to determine deformation in bubble shape due to acoustic field parameters. This was done by determining the quadrupole projection of the acoustic radiation pressure on a small compressible sphere. Calculations allowed for the determination of the maximum energy density allowable to still assume sphericity of the bubble. The spherical assumption was necessary for less complicated equations for the remainder of the modeling. Figure 9 shows the results of this calculation, indicating that the maximum energy density for a bubble with a radius of 100 μm is 0.649 J/m^3. Experimental hydrophone measurements showed that at normal operating conditions the average energy density of the system falls far below that value, as seen from Figure 61 and Table 1, indicating that the spherical assumption holds for experimental results

assuming the bubbles in the system have a radius of 100 μm or less, which is not necessarily always the case. To this end the maximum energy density for a variety of bubble radii was calculated. The primary force balance on a single bubble was then used to calculate the minimum energy density required to effect capture. Figure 16 give the results of these calculations showing that a bubble with a chosen radius that falls within the shaded area can be assumed spherical and will also be captured based on energy density. It should be noted that hydrophone measurements are suspect because they show an energy density in the acoustic chamber that is too low to effect capture based on calculated results.

To determine the equilibrium resting position and velocity of a single bubble as a function of size and energy density, the primary force balance was solved for the velocity term of the drag force, equation (3.9). Subsequent solving gave equations returning the position and velocity of a single bubble within a resonant acoustic chamber with respect to the location of the acoustic pressure antinodes for a given initial position.

The determination of the relative trajectory of a pair of bubbles as a function of relevant operating parameters required the development of a mathematical model. The relative motion of two bubbles toward one another is governed by both primary forces and by inter-bubble effects and the compilation of these effects result in equations (3.62) and (3.63). The model results indicate that the typical relative trajectory of a bubble pair has an initial slower motion followed by a faster approach followed by collision of the bubble pair. Subsequent calculations showed that for the parameters and bubble sizes stated previously, that the secondary acoustic force was large enough to overcome the difference between the primary acoustic and buoyancy forces, pulling the second bubble

through the pressure nodes and antinodes that separated the bubble pair. This is valid for an initial *y*-coordinate separation of 1.1 cm, again for the previously stated parameters. For the microscopic model these results indicate that the bubble motion is driven primarily by the secondary acoustic force, and that both the slow and fast approach are primarily due to the secondary acoustic force and that, as seen in Figure 17, the secondary acoustic force increases exponentially as the bubbles approach on another.

The trajectory analysis was used to define iso-time collision contours, showing the location, with respect to a fixed bubble one, at which bubble two would have to reside for it to collide with bubble one within the time indicated by the contour. These calculations were done for both variable energy density and variable radii ratios. To represent this data in combined form, each iso-time contour was rotated about the y-axis to form a sphere/ellipsoid allowing for the calculation of volume cleared by the clustering of bubble pairs as a function of time. Collision rate constants were then determined from this data. Section 4.4 shows bubble trajectories taken from experiments compared to trajectories from the model. Fairly good agreement is seen between the two, proving that the model is an accurate prediction of bubble pair trajectories.

Through the literature survey it was discovered that the secondary acoustic force acting between a pair of bubbles is not always attractive, but can change sign based on bubble size and movement of bubbles toward one another. This can result in the forming stable bound pairs or clusters that won't necessarily coalesce like originally believed for this research [64-70, 74, 75, 77]. These types of calculations were beyond the scope of this research, but experimental observations coincided with those observations. No actual coalescence was viewed during experiments, but clusters formed almost

immediately upon introduction of the sound field. A variety of cluster types were observed, with the differences most likely resulting from hot spots causing lateral acoustic forces within the acoustic chamber.

5.2 Suggested Future Work

Further research should include analysis the effect of hot spots within the acoustic chamber. The lateral acoustic forces that arise from non-uniformities of transducer may alter the validity of the spherical assumption and of the droplet pair model by increasing the primary forces acting on a bubble. The intensity and location of these hot spots might also be responsible for the variety of bubble cluster types seen in experiments. If a hydrophone could be found that could return accurate results, pressure measurements could be taken at the location of each type of bubble cluster and then compared to the average pressure of the system.

Future work could also address the issues pertaining to the resonance frequency of the bubbles in the bubble pair model. The equation for the secondary acoustic force could possibly include necessary additions related to the changing sign due primarily to the resonance frequency of the bubble. It may also be possible that the hydrodynamic mobility functions for bubbles differ from those for drops due, once again, to the monopole resonance frequency of the bubbles. A literature search should be done on this.

Because this research was originally proposed for microgravity environments, it would be beneficial to run experiments under these conditions. Models developed would have to be modified slightly to neglect the gravitational effect, and results from the

models and experiments under normal gravity conditions could be compared to those under microgravity to determine how the trajectories and time to collision would change.

Final suggestions regard experimental work. A slightly better design of the acoustic chamber would be beneficial. Currently the positioning screws are rather large and do not allow for minute changes in the position of the transducer. Screws allowing for a larger number of turns per inch would be beneficial. Also, a variety of syringe insertion points would be useful to obtain experimental trajectory results for other angles. Obtaining longer needles for the syringe would also be beneficial so bubbles could be inserted into the chamber closer to the center of the transducer. When running experiments with salt water, the chamber should be filled with DI water first and then salt water should be injected. For hydrophone measurements, one of the ports in the acrylic centerpiece should be enlarged to allow for insertion of the hydrophone so that values of the energy density in a closed system could be measured.

Appendix A1

This appendix shows Mathematica 6 code for the cubic spline calculations discussed in Section 3.3.4.

```
Ag = (sfar - s)/(sfar - snear);
Bg = (s - snear)/(sfar - snear);
Cg = (1/6) * (Ag^3 - Ag) * (sfar - snear)^2;
Dg = (1/6) * (Bg^3 - Bg) * (sfar - snear)^2;

Gfar = 1 - 2 * (2 + 3*μ)/(1 + μ) * λ/((1 + λ)^2 * s) + 8 * μ/(1 + μ) * λ*(λ^2 + 1)/((1 + λ^4) * s^3) - 4 * (2 + 5*μ) * (2 + 3*μ)/(1 + μ)^2 * λ*(λ^3 + 1)/((1 + λ)^5 * s^4);

∂s Gfar

-(24 λ (1 + λ^2) μ)/(s^4 (1 + λ^4) (1 + μ)) + (2 λ (2 + 3 μ))/(s^2 (1 + λ)^2 (1 + μ)) + (16 λ (1 + λ^3) (2 + 3 μ) (2 + 5 μ))/(s^5 (1 + λ)^5 (1 + μ)^2)

DGfar = -(24 λ (1 + λ^2) μ)/(s^4 (1 + λ^4) (1 + μ)) + (2 λ (2 + 3 μ))/(s^2 (1 + λ)^2 (1 + μ)) + (16 λ (1 + λ^3) (2 + 3 μ) (2 + 5 μ))/(s^5 (1 + λ)^5 (1 + μ)^2);

∂s DGfar

(96 λ (1 + λ^2) μ)/(s^5 (1 + λ^4) (1 + μ)) - (4 λ (2 + 3 μ))/(s^3 (1 + λ)^2 (1 + μ)) - (80 λ (1 + λ^3) (2 + 3 μ) (2 + 5 μ))/(s^6 (1 + λ)^5 (1 + μ)^2)

DDGfar = (96 λ (1 + λ^2) μ)/(s^5 (1 + λ^4) (1 + μ)) - (4 λ (2 + 3 μ))/(s^3 (1 + λ)^2 (1 + μ)) - (80 λ (1 + λ^3) (2 + 3 μ) (2 + 5 μ))/(s^6 (1 + λ)^5 (1 + μ)^2);

Λ = π^2 * √2 * μ/(16 * (1 + 1/λ)^(3/2)) * (2/(ξ * (1 + λ)))^(1/2) + λ/(3 * (1 + λ)) * (1 - μ^2/3) * Log[ξ * (1 + λ)/2]^(-1) + C0;

ξ = s - 2;

Gnear = ((B1 + λ * B2) * (3*μ + 2)/(3*μ + 3))/((1 + λ) * (Λ * (B2 + B2/λ) - B1^2/λ * (3*μ + 2)/(3*μ + 3)));
```

∂_s **Gnear**

$$-\frac{\left(B2+\frac{B2}{\lambda}\right)\,(B1+B2\,\lambda)\,(2+3\,\mu)\left(-\frac{\pi^2\,\mu}{16\,(-2+s)^2\left(1+\frac{1}{\lambda}\right)^{3/2}\sqrt{\frac{1}{(-2+s)\,(1+\lambda)}}\,(1+\lambda)}-\frac{\lambda\left(1-\frac{\mu^2}{3}\right)}{3\,(-2+s)\,(1+\lambda)\,\mathrm{Log}\left[\frac{1}{2}\,(-2+s)\,(1+\lambda)\right]^2}\right)}{(1+\lambda)\,(3+3\,\mu)\left(-\frac{B1^2\,(2+3\,\mu)}{\lambda\,(3+3\,\mu)}+\left(B2+\frac{B2}{\lambda}\right)\left(C0+\frac{\pi^2\sqrt{\frac{1}{(-2+s)\,(1+\lambda)}}\,\mu}{8\left(1+\frac{1}{\lambda}\right)^{3/2}}+\frac{\lambda\left(1-\frac{\mu^2}{3}\right)}{3\,(1+\lambda)\,\mathrm{Log}\left[\frac{1}{2}\,(-2+s)\,(1+\lambda)\right]}\right)\right)^2}$$

DGnear =

$$-\left(\left(B2+\frac{B2}{\lambda}\right)\,(B1+B2\,\lambda)\,(2+3\,\mu)\left(-\frac{\pi^2\,\mu}{16\,(-2+s)^2\left(1+\frac{1}{\lambda}\right)^{3/2}\sqrt{\frac{1}{(-2+s)\,(1+\lambda)}}\,(1+\lambda)}-\frac{\lambda\left(1-\frac{\mu^2}{3}\right)}{3\,(-2+s)\,(1+\lambda)\,\mathrm{Log}\left[\frac{1}{2}\,(-2+s)\,(1+\lambda)\right]^2}\right)\right)\Big/$$

$$\left((1+\lambda)\,(3+3\,\mu)\left(-\frac{B1^2\,(2+3\,\mu)}{\lambda\,(3+3\,\mu)}+\left(B2+\frac{B2}{\lambda}\right)\left(C0+\frac{\pi^2\sqrt{\frac{1}{(-2+s)\,(1+\lambda)}}\,\mu}{8\left(1+\frac{1}{\lambda}\right)^{3/2}}+\frac{\lambda\left(1-\frac{\mu^2}{3}\right)}{3\,(1+\lambda)\,\mathrm{Log}\left[\frac{1}{2}\,(-2+s)\,(1+\lambda)\right]}\right)\right)^2\right);$$

∂_s **DGnear**

$$-\left(\left(\text{B2}+\frac{\text{B2}}{\lambda}\right)\ (\text{B1}+\text{B2}\,\lambda)\ (2+3\,\mu)\left(-\frac{\pi^2\,\mu}{32\ (-2+\text{s})^4\ \left(1+\frac{1}{\lambda}\right)^{3/2}\left(\frac{1}{(-2+\text{s})\ (1+\lambda)}\right)^{3/2}\ (1+\lambda)^2}+\right.\right.$$

$$\frac{\pi^2\,\mu}{8\ (-2+\text{s})^3\left(1+\frac{1}{\lambda}\right)^{3/2}\sqrt{\frac{1}{(-2+\text{s})\ (1+\lambda)}}\ (1+\lambda)}+\frac{2\,\lambda\left(1-\frac{\mu^2}{3}\right)}{3\ (-2+\text{s})^2\ (1+\lambda)\ \text{Log}\left[\frac{1}{2}\ (-2+\text{s})\ (1+\lambda)\right]^3}+$$

$$\left.\left.\frac{\lambda\left(1-\frac{\mu^2}{3}\right)}{3\ (-2+\text{s})^2\ (1+\lambda)\ \text{Log}\left[\frac{1}{2}\ (-2+\text{s})\ (1+\lambda)\right]^2}\right)\right)\Bigg/\left((1+\lambda)\ (3+3\,\mu)\right.$$

$$\left.\left(-\frac{\text{B1}^2\ (2+3\,\mu)}{\lambda\ (3+3\,\mu)}+\left(\text{B2}+\frac{\text{B2}}{\lambda}\right)\left(\text{C0}+\frac{\pi^2\sqrt{\frac{1}{(-2+\text{s})\ (1+\lambda)}}\ \mu}{8\left(1+\frac{1}{\lambda}\right)^{3/2}}+\frac{\lambda\left(1-\frac{\mu^2}{3}\right)}{3\ (1+\lambda)\ \text{Log}\left[\frac{1}{2}\ (-2+\text{s})\ (1+\lambda)\right]}\right)\right)^2\right)+$$

$$\left(2\left(\text{B2}+\frac{\text{B2}}{\lambda}\right)^2\ (\text{B1}+\text{B2}\,\lambda)\ (2+3\,\mu)\left(-\frac{\pi^2\,\mu}{16\ (-2+\text{s})^2\left(1+\frac{1}{\lambda}\right)^{3/2}\sqrt{\frac{1}{(-2+\text{s})\ (1+\lambda)}}\ (1+\lambda)}-\right.\right.$$

$$\left.\left.\frac{\lambda\left(1-\frac{\mu^2}{3}\right)}{3\ (-2+\text{s})\ (1+\lambda)\ \text{Log}\left[\frac{1}{2}\ (-2+\text{s})\ (1+\lambda)\right]^2}\right)^2\right)\Bigg/\left((1+\lambda)\ (3+3\,\mu)\right.$$

$$\left.\left.\left(-\frac{\text{B1}^2\ (2+3\,\mu)}{\lambda\ (3+3\,\mu)}+\left(\text{B2}+\frac{\text{B2}}{\lambda}\right)\left(\text{C0}+\frac{\pi^2\sqrt{\frac{1}{(-2+\text{s})\ (1+\lambda)}}\ \mu}{8\left(1+\frac{1}{\lambda}\right)^{3/2}}+\frac{\lambda\left(1-\frac{\mu^2}{3}\right)}{3\ (1+\lambda)\ \text{Log}\left[\frac{1}{2}\ (-2+\text{s})\ (1+\lambda)\right]}\right)\right)^3\right)\right)$$

$$
\begin{aligned}
\mathrm{DDGnear} = & \\
& -\Bigg(\left(\mathrm{B2} + \frac{\mathrm{B2}}{\lambda}\right) (\mathrm{B1} + \mathrm{B2}\,\lambda)\,(2 + 3\,\mu) \\
& \quad \Bigg(-\frac{\pi^2\,\mu}{32\,(-2+\mathrm{s})^4 \left(1+\frac{1}{\lambda}\right)^{3/2} \left(\frac{1}{(-2+\mathrm{s})\,(1+\lambda)}\right)^{3/2} (1+\lambda)^2} + \\
& \quad \frac{\pi^2\,\mu}{8\,(-2+\mathrm{s})^3 \left(1+\frac{1}{\lambda}\right)^{3/2} \sqrt{\frac{1}{(-2+\mathrm{s})\,(1+\lambda)}}\;(1+\lambda)} + \frac{2\,\lambda\left(1-\frac{\mu^2}{3}\right)}{3\,(-2+\mathrm{s})^2\,(1+\lambda)\,\mathrm{Log}\left[\frac{1}{2}\,(-2+\mathrm{s})\,(1+\lambda)\right]^3} + \\
& \quad \frac{\lambda\left(1-\frac{\mu^2}{3}\right)}{3\,(-2+\mathrm{s})^2\,(1+\lambda)\,\mathrm{Log}\left[\frac{1}{2}\,(-2+\mathrm{s})\,(1+\lambda)\right]^2}\Bigg)\Bigg) \Bigg/ \\
& \quad \Bigg((1+\lambda)\,(3+3\,\mu) \\
& \quad \Bigg(-\frac{\mathrm{B1}^2\,(2+3\,\mu)}{\lambda\,(3+3\,\mu)} + \left(\mathrm{B2} + \frac{\mathrm{B2}}{\lambda}\right) \left(\mathrm{C0} + \frac{\pi^2 \sqrt{\frac{1}{(-2+\mathrm{s})\,(1+\lambda)}}\;\mu}{8\left(1+\frac{1}{\lambda}\right)^{3/2}} + \frac{\lambda\left(1-\frac{\mu^2}{3}\right)}{3\,(1+\lambda)\,\mathrm{Log}\left[\frac{1}{2}\,(-2+\mathrm{s})\,(1+\lambda)\right]} \right)\Bigg)^2\Bigg) + \\
& 2\left(\mathrm{B2} + \frac{\mathrm{B2}}{\lambda}\right)^2 (\mathrm{B1} + \mathrm{B2}\,\lambda)\,(2 + 3\,\mu) \\
& \quad \Bigg(-\frac{\pi^2\,\mu}{16\,(-2+\mathrm{s})^2 \left(1+\frac{1}{\lambda}\right)^{3/2} \sqrt{\frac{1}{(-2+\mathrm{s})\,(1+\lambda)}}\;(1+\lambda)} - \\
& \quad \frac{\lambda\left(1-\frac{\mu^2}{3}\right)}{3\,(-2+\mathrm{s})\,(1+\lambda)\,\mathrm{Log}\left[\frac{1}{2}\,(-2+\mathrm{s})\,(1+\lambda)\right]^2}\Bigg)^2 \Bigg/ \\
& \quad \Bigg((1+\lambda)\,(3+3\,\mu) \\
& \quad \Bigg(-\frac{\mathrm{B1}^2\,(2+3\,\mu)}{\lambda\,(3+3\,\mu)} + \left(\mathrm{B2} + \frac{\mathrm{B2}}{\lambda}\right) \left(\mathrm{C0} + \frac{\pi^2 \sqrt{\frac{1}{(-2+\mathrm{s})\,(1+\lambda)}}\;\mu}{8\left(1+\frac{1}{\lambda}\right)^{3/2}} + \frac{\lambda\left(1-\frac{\mu^2}{3}\right)}{3\,(1+\lambda)\,\mathrm{Log}\left[\frac{1}{2}\,(-2+\mathrm{s})\,(1+\lambda)\right]} \right)\Bigg)^3\Bigg);
\end{aligned}
$$

```
Gnear /. s → snear
```

$$\frac{(B1 + B2\,\lambda)\,(2 + 3\,\mu)}{(1+\lambda)\,(3+3\,\mu)\left(-\frac{B1^2\,(2+3\,\mu)}{\lambda\,(3+3\,\mu)} + \left(B2 + \frac{B2}{\lambda}\right)\left(C0 + \frac{\pi^2\sqrt{\frac{1}{(-2+snear)\,(1+\lambda)}}\,\mu}{8\left(1+\frac{1}{\lambda}\right)^{3/2}} + \frac{\lambda\left(1-\frac{\mu^2}{3}\right)}{3\,(1+\lambda)\,\text{Log}\left[\frac{1}{2}\,(-2+snear)\,(1+\lambda)\right]}\right)\right)}$$

```
Gnsn =
```

$$\frac{(B1 + B2\,\lambda)\,(2 + 3\,\mu)}{(1+\lambda)\,(3+3\,\mu)\left(-\frac{B1^2\,(2+3\,\mu)}{\lambda\,(3+3\,\mu)} + \left(B2 + \frac{B2}{\lambda}\right)\left(C0 + \frac{\pi^2\sqrt{\frac{1}{(-2+snear)\,(1+\lambda)}}\,\mu}{8\left(1+\frac{1}{\lambda}\right)^{3/2}} + \frac{\lambda\left(1-\frac{\mu^2}{3}\right)}{3\,(1+\lambda)\,\text{Log}\left[\frac{1}{2}\,(-2+snear)\,(1+\lambda)\right]}\right)\right)};$$

```
DDGnear /. s → snear
```

$$-\left(\left(B2+\frac{B2}{\lambda}\right)\,(B1+B2\,\lambda)\,(2+3\,\mu)\left(-\frac{\pi^2\,\mu}{32\,(-2+\text{snear})^4\left(1+\frac{1}{\lambda}\right)^{3/2}\left(\frac{1}{(-2+\text{snear})\,(1+\lambda)}\right)^{3/2}(1+\lambda)^2}+\right.\right.$$

$$\frac{\pi^2\,\mu}{8\,(-2+\text{snear})^3\left(1+\frac{1}{\lambda}\right)^{3/2}\sqrt{\frac{1}{(-2+\text{snear})\,(1+\lambda)}}\;(1+\lambda)}+$$

$$\frac{2\,\lambda\left(1-\frac{\mu^2}{3}\right)}{3\,(-2+\text{snear})^2\,(1+\lambda)\,\text{Log}\left[\frac{1}{2}\,(-2+\text{snear})\,(1+\lambda)\right]^3}+$$

$$\left.\left.\frac{\lambda\left(1-\frac{\mu^2}{3}\right)}{3\,(-2+\text{snear})^2\,(1+\lambda)\,\text{Log}\left[\frac{1}{2}\,(-2+\text{snear})\,(1+\lambda)\right]^2}\right)\right)\Bigg/\left((1+\lambda)\,(3+3\,\mu)\left(-\frac{B1^2\,(2+3\,\mu)}{\lambda\,(3+3\,\mu)}+\right.\right.$$

$$\left.\left.\left(B2+\frac{B2}{\lambda}\right)\left(C0+\frac{\pi^2\sqrt{\frac{1}{(-2+\text{snear})\,(1+\lambda)}}\;\mu}{8\left(1+\frac{1}{\lambda}\right)^{3/2}}+\frac{\lambda\left(1-\frac{\mu^2}{3}\right)}{3\,(1+\lambda)\,\text{Log}\left[\frac{1}{2}\,(-2+\text{snear})\,(1+\lambda)\right]}\right)\right)^2\right)+$$

$$\left(2\left(B2+\frac{B2}{\lambda}\right)^2(B1+B2\,\lambda)\,(2+3\,\mu)\left(-\frac{\pi^2\,\mu}{16\,(-2+\text{snear})^2\left(1+\frac{1}{\lambda}\right)^{3/2}\sqrt{\frac{1}{(-2+\text{snear})\,(1+\lambda)}}\;(1+\lambda)}-\right.\right.$$

$$\left.\left.\frac{\lambda\left(1-\frac{\mu^2}{3}\right)}{3\,(-2+\text{snear})\,(1+\lambda)\,\text{Log}\left[\frac{1}{2}\,(-2+\text{snear})\,(1+\lambda)\right]^2}\right)^2\right)\Bigg/$$

$$\left((1+\lambda)\,(3+3\,\mu)\left(-\frac{B1^2\,(2+3\,\mu)}{\lambda\,(3+3\,\mu)}+\left(B2+\frac{B2}{\lambda}\right)\left(C0+\frac{\pi^2\sqrt{\frac{1}{(-2+\text{snear})\,(1+\lambda)}}\;\mu}{8\left(1+\frac{1}{\lambda}\right)^{3/2}}+\right.\right.\right.$$

$$\left.\left.\left.\frac{\lambda\left(1-\frac{\mu^2}{3}\right)}{3\,(1+\lambda)\,\text{Log}\left[\frac{1}{2}\,(-2+\text{snear})\,(1+\lambda)\right]}\right)\right)^3\right)$$

$$
\begin{aligned}
\text{DDGnsn} = &-\left(\left(B2 + \frac{B2}{\lambda}\right)(B1 + B2\,\lambda)(2 + 3\,\mu)\right.\\
&\left(-\frac{\pi^2\,\mu}{32\,(-2+\text{snear})^4\left(1+\frac{1}{\lambda}\right)^{3/2}\left(\frac{1}{(-2+\text{snear})(1+\lambda)}\right)^{3/2}(1+\lambda)^2} + \frac{\pi^2\,\mu}{8\,(-2+\text{snear})^3\left(1+\frac{1}{\lambda}\right)^{3/2}\sqrt{\frac{1}{(-2+\text{snear})(1+\lambda)}}\,(1+\lambda)} +\right.\\
&\frac{2\,\lambda\left(1-\frac{\mu^2}{3}\right)}{3\,(-2+\text{snear})^2(1+\lambda)\,\text{Log}\left[\frac{1}{2}(-2+\text{snear})(1+\lambda)\right]^3} +\\
&\left.\left.\frac{\lambda\left(1-\frac{\mu^2}{3}\right)}{3\,(-2+\text{snear})^2(1+\lambda)\,\text{Log}\left[\frac{1}{2}(-2+\text{snear})(1+\lambda)\right]^2}\right)\right)\Big/\\
&\left((1+\lambda)(3+3\,\mu)\right.\\
&\left.\left(-\frac{B1^2\,(2+3\,\mu)}{\lambda\,(3+3\,\mu)} + \left(B2+\frac{B2}{\lambda}\right)\left(C0 + \frac{\pi^2\sqrt{\frac{1}{(-2+\text{snear})(1+\lambda)}}\,\mu}{8\left(1+\frac{1}{\lambda}\right)^{3/2}} + \frac{\lambda\left(1-\frac{\mu^2}{3}\right)}{3\,(1+\lambda)\,\text{Log}\left[\frac{1}{2}(-2+\text{snear})(1+\lambda)\right]}\right)\right)^2\right) +\\
&\left(2\left(B2+\frac{B2}{\lambda}\right)^2(B1+B2\,\lambda)(2+3\,\mu)\right.\\
&\left(-\frac{\pi^2\,\mu}{16\,(-2+\text{snear})^2\left(1+\frac{1}{\lambda}\right)^{3/2}\sqrt{\frac{1}{(-2+\text{snear})(1+\lambda)}}\,(1+\lambda)} -\right.\\
&\left.\left.\frac{\lambda\left(1-\frac{\mu^2}{3}\right)}{3\,(-2+\text{snear})(1+\lambda)\,\text{Log}\left[\frac{1}{2}(-2+\text{snear})(1+\lambda)\right]^2}\right)^2\right)\Big/\\
&\left((1+\lambda)(3+3\,\mu)\right.\\
&\left.\left.\left(-\frac{B1^2\,(2+3\,\mu)}{\lambda\,(3+3\,\mu)} + \left(B2+\frac{B2}{\lambda}\right)\left(C0 + \frac{\pi^2\sqrt{\frac{1}{(-2+\text{snear})(1+\lambda)}}\,\mu}{8\left(1+\frac{1}{\lambda}\right)^{3/2}} + \frac{\lambda\left(1-\frac{\mu^2}{3}\right)}{3\,(1+\lambda)\,\text{Log}\left[\frac{1}{2}(-2+\text{snear})(1+\lambda)\right]}\right)\right)^3\right);
\end{aligned}
$$

```
Gfar /. s → sfar
```

$$1+\frac{8\lambda\left(1+\lambda^2\right)\mu}{\text{sfar}^3\left(1+\lambda^4\right)(1+\mu)}-\frac{2\lambda(2+3\mu)}{\text{sfar}(1+\lambda)^2(1+\mu)}-\frac{4\lambda\left(1+\lambda^3\right)(2+3\mu)(2+5\mu)}{\text{sfar}^4(1+\lambda)^5(1+\mu)^2}$$

```
Gfsf = 1 + 8 λ (1 + λ^2) μ / (sfar^3 (1 + λ^4) (1 + μ)) - 2 λ (2 + 3 μ) / (sfar (1 + λ)^2 (1 + μ)) - 4 λ (1 + λ^3) (2 + 3 μ) (2 + 5 μ) / (sfar^4 (1 + λ)^5 (1 + μ)^2);
```

```
DDGfar /. s → sfar
```

$$\frac{96\lambda\left(1+\lambda^2\right)\mu}{\text{sfar}^5\left(1+\lambda^4\right)(1+\mu)}-\frac{4\lambda(2+3\mu)}{\text{sfar}^3(1+\lambda)^2(1+\mu)}-\frac{80\lambda\left(1+\lambda^3\right)(2+3\mu)(2+5\mu)}{\text{sfar}^6(1+\lambda)^5(1+\mu)^2}$$

```
DDGfsf = 96 λ (1 + λ^2) μ / (sfar^5 (1 + λ^4) (1 + μ)) - 4 λ (2 + 3 μ) / (sfar^3 (1 + λ)^2 (1 + μ)) - 80 λ (1 + λ^3) (2 + 3 μ) (2 + 5 μ) / (sfar^6 (1 + λ)^5 (1 + μ)^2);
```

$$\text{Gmod} = \text{Ag} * \text{Gnsn} + \text{Bg} * \text{Gfsf} + \text{Cg} * \text{DDGnsn} + \text{Dg} * \text{DDGfsf}$$

$$\frac{1}{6}\left(\frac{(s-\text{snear})^3}{(\text{sfar}-\text{snear})^3}-\frac{s-\text{snear}}{\text{sfar}-\text{snear}}\right)(\text{sfar}-\text{snear})^2$$
$$\left(\frac{96\lambda\left(1+\lambda^2\right)\mu}{\text{sfar}^5\left(1+\lambda^4\right)(1+\mu)}-\frac{4\lambda(2+3\mu)}{\text{sfar}^3(1+\lambda)^2(1+\mu)}-\frac{80\lambda\left(1+\lambda^3\right)(2+3\mu)(2+5\mu)}{\text{sfar}^6(1+\lambda)^5(1+\mu)^2}\right)+$$
$$\frac{(s-\text{snear})\left(1+\frac{8\lambda\left(1+\lambda^2\right)\mu}{\text{sfar}^3\left(1+\lambda^4\right)(1+\mu)}-\frac{2\lambda(2+3\mu)}{\text{sfar}(1+\lambda)^2(1+\mu)}-\frac{4\lambda\left(1+\lambda^3\right)(2+3\mu)(2+5\mu)}{\text{sfar}^4(1+\lambda)^5(1+\mu)^2}\right)}{\text{sfar}-\text{snear}}+\frac{1}{6}\left(\frac{(-s+\text{sfar})^3}{(\text{sfar}-\text{snear})^3}-\frac{-s+\text{sfar}}{\text{sfar}-\text{snear}}\right)$$
$$(\text{sfar}-\text{snear})^2\left(-\left(\left(\text{B2}+\frac{\text{B2}}{\lambda}\right)(\text{B1}+\text{B2}\lambda)(2+3\mu)\left(-\frac{\pi^2\mu}{32(-2+\text{snear})^4\left(1+\frac{1}{\lambda}\right)^{3/2}\left(\frac{1}{(-2+\text{snear})(1+\lambda)}\right)^{3/2}(1+\lambda)^2}+\right.\right.\right.$$
$$\frac{\pi^2\mu}{8(-2+\text{snear})^3\left(1+\frac{1}{\lambda}\right)^{3/2}\sqrt{\frac{1}{(-2+\text{snear})(1+\lambda)}}(1+\lambda)}+\frac{2\lambda\left(1-\frac{\mu^2}{3}\right)}{3(-2+\text{snear})^2(1+\lambda)\text{Log}\left[\frac{1}{2}(-2+\text{snear})(1+\lambda)\right]^3}+$$
$$\left.\left.\left.\frac{\lambda\left(1-\frac{\mu^2}{3}\right)}{3(-2+\text{snear})^2(1+\lambda)\text{Log}\left[\frac{1}{2}(-2+\text{snear})(1+\lambda)\right]^2}\right)\right)\Big/\left((1+\lambda)(3+3\mu)\right.$$
$$\left.\left(-\frac{\text{B1}^2(2+3\mu)}{\lambda(3+3\mu)}+\left(\text{B2}+\frac{\text{B2}}{\lambda}\right)\left(\text{C0}+\frac{\pi^2\sqrt{\frac{1}{(-2+\text{snear})(1+\lambda)}}\mu}{8\left(1+\frac{1}{\lambda}\right)^{3/2}}+\frac{\lambda\left(1-\frac{\mu^2}{3}\right)}{3(1+\lambda)\text{Log}\left[\frac{1}{2}(-2+\text{snear})(1+\lambda)\right]}\right)\right)^2\right)+$$
$$\left(2\left(\text{B2}+\frac{\text{B2}}{\lambda}\right)^2(\text{B1}+\text{B2}\lambda)(2+3\mu)\left(-\frac{\pi^2\mu}{16(-2+\text{snear})^2\left(1+\frac{1}{\lambda}\right)^{3/2}\sqrt{\frac{1}{(-2+\text{snear})(1+\lambda)}}(1+\lambda)}-\right.\right.$$
$$\left.\left.\frac{\lambda\left(1-\frac{\mu^2}{3}\right)}{3(-2+\text{snear})(1+\lambda)\text{Log}\left[\frac{1}{2}(-2+\text{snear})(1+\lambda)\right]^2}\right)^2\right)\Big/\left((1+\lambda)(3+3\mu)\right.$$
$$\left.\left.\left(-\frac{\text{B1}^2(2+3\mu)}{\lambda(3+3\mu)}+\left(\text{B2}+\frac{\text{B2}}{\lambda}\right)\left(\text{C0}+\frac{\pi^2\sqrt{\frac{1}{(-2+\text{snear})(1+\lambda)}}\mu}{8\left(1+\frac{1}{\lambda}\right)^{3/2}}+\frac{\lambda\left(1-\frac{\mu^2}{3}\right)}{3(1+\lambda)\text{Log}\left[\frac{1}{2}(-2+\text{snear})(1+\lambda)\right]}\right)\right)^3\right)\right)+$$
$$((-s+\text{sfar})(\text{B1}+\text{B2}\lambda)(2+3\mu))\Big/\left((\text{sfar}-\text{snear})(1+\lambda)(3+3\mu)\right.$$
$$\left.\left.\left(-\frac{\text{B1}^2(2+3\mu)}{\lambda(3+3\mu)}+\left(\text{B2}+\frac{\text{B2}}{\lambda}\right)\left(\text{C0}+\frac{\pi^2\sqrt{\frac{1}{(-2+\text{snear})(1+\lambda)}}\mu}{8\left(1+\frac{1}{\lambda}\right)^{3/2}}+\frac{\lambda\left(1-\frac{\mu^2}{3}\right)}{3(1+\lambda)\text{Log}\left[\frac{1}{2}(-2+\text{snear})(1+\lambda)\right]}\right)\right)\right)\right)$$

```
snear = 2.00004;
sfar = 2.0002;
Gfsf = 0.434161893;
Gnsn = 0.417671626;
B1 = 0.669411286;
B2 = 0.669411286;
C0 = 0.656031192;
μ = 0.0173;
λ = 0.909090909;
```

```
Gmod
```

$$-0.195856\left(-6250.\,(2.0002-s)+2.44141\times10^{11}\,(2.0002-s)^3\right)-$$
$$2.24271\times10^{-9}\left(-6250.\,(-2.00004+s)+2.44141\times10^{11}\,(-2.00004+s)^3\right)+$$
$$1657.48\,(2.0002-s)+2805.06\,(-2.00004+s)$$

```
FullSimplify[%]
```

$$4.78163\times10^{10}\,(-1.99999+s)\,(4.00123+(-4.00061+s)\,s)$$

```
P1 = Plot[Gmod, {s, snear, sfar},
  PlotStyle → {Dashing[{0.03, 0.03}], Thickness[0.012], Hue[1]}, AxesLabel → {"s", "G"}]
```

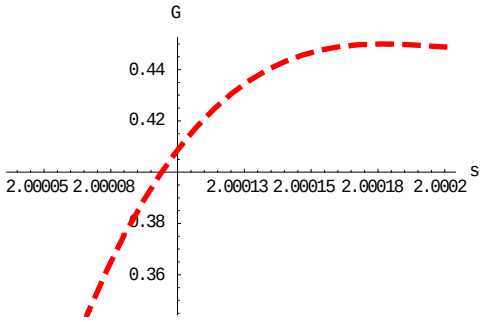

- Graphics -

```
P2 = Plot[Gnear, {s, 2, snear}, PlotStyle → {Thickness[0.012]}, AxesLabel → {"s", "G"}]
```

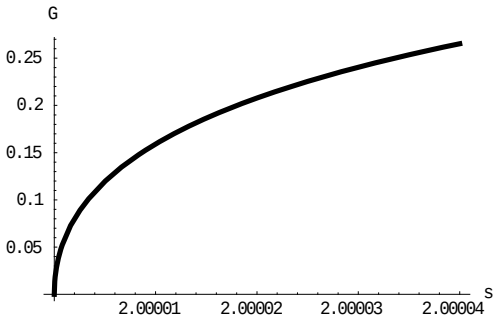

- Graphics -

```
P3 = Plot[Gfar, {s, sfar, 2.0004}, PlotStyle → {Thickness[0.012]}, AxesLabel → {"s", "G"}]
```

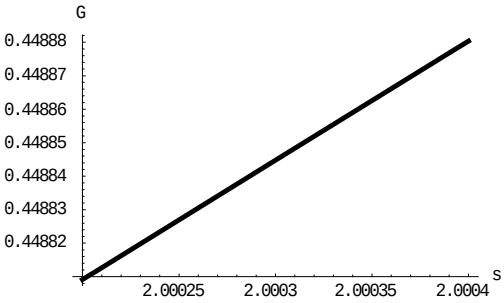


```
- Graphics -
```

```
Show[P1, P2, P3]
```

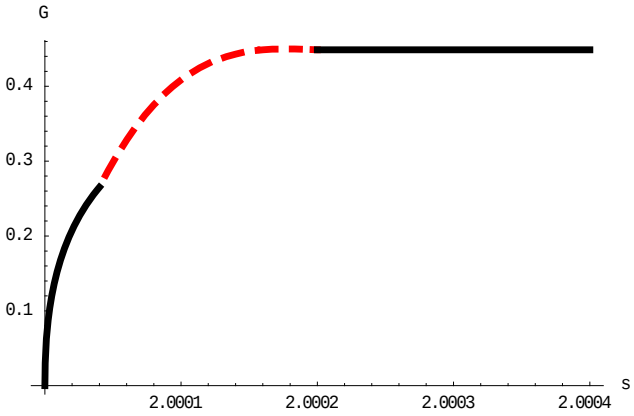


```
- Graphics -
```

Appendix A2

This appendix shows Mathematica 6 code for the bubble pair trajectory model.

```
dVvdW[t_] :=
  (-(4096 A ahat^3 s[t]) / (3 (a1 + a2) (1 + ahat)^2 (-4 + (s[t])^2)^2 (-4 (-1 + ahat)^2 + (1 + ahat)^2 (s[t])^2)^2)) / A;
L[t_] := 1 - (2 + 3 * μ)/(1 + μ) * (ahat^2 + ahat + 1)/(1 + ahat)^2 * 1/s[t] + 4 * μ/(1 + μ) * ((ahat^2 + ahat + 1) * (ahat^2 + 1))/((1 + ahat)^3 * (ahat + 1)) * 1/(s[t])^3;
G[t_] := 1 - 2 * (2 + 3 * μ)/(1 + μ) * ahat^3/(1 + ahat)^2 * 1/s[t] + 8 * μ/(1 + μ) * (ahat * (ahat^2 + 1))/(1 + ahat)^4 * 1/(s[t])^3 -
   4 * ((2 + 5 * μ) * (2 + 3 * μ))/(1 + μ)^2 * (ahat * (ahat^3 + 1))/(1 + ahat)^5 * 1/(s[t])^4;
M[t_] := 1 - (2 + 3 * μ)/(2 * (1 + μ)) * (ahat^2 + ahat + 1)/(1 + ahat)^2 * 1/s[t] - 2 * μ/(1 + μ) * ((ahat^2 + ahat + 1) * (ahat^2 + 1))/((1 + ahat)^3 * (ahat + 1)) * 1/(s[t])^3;
V10[t_] :=
  (2 (p1 - q1) (p1 + q1) (p1 + q1 Sin[a yo1])
     (p1 (p1 + q1 Sin[a yo1]) - Cosh[a Sqrt[-p1^2 + q1^2] t] ((-p1^2 + q1^2) Cos[a yo1] + q1 (q1 + p1 Sin[a yo1])) -
       Sqrt[-p1^2 + q1^2] (q1 + q1 Cos[a yo1] + p1 Sin[a yo1]) Sinh[a Sqrt[-p1^2 + q1^2] t])) /
   ((q1^2 + (-p1 + q1) (p1 + q1) Cos[a yo1] - p1^2 Cosh[a Sqrt[-p1^2 + q1^2] t] -
       2 p1 q1 Sin[a yo1] Sinh[1/2 a Sqrt[-p1^2 + q1^2] t]^2)^2
     (1 +
       (-p1 (q1 + p1 Sin[a yo1]) + q1 Cosh[a Sqrt[-p1^2 + q1^2] t] (p1 + q1 Sin[a yo1]) +
          Sqrt[-p1^2 + q1^2] (p1 + q1 Sin[a yo1]) Sinh[a Sqrt[-p1^2 + q1^2] t])^2 /
        (q1^2 + (-p1 + q1) (p1 + q1) Cos[a yo1] - p1^2 Cosh[a Sqrt[-p1^2 + q1^2] t] -
          2 p1 q1 Sin[a yo1] Sinh[1/2 a Sqrt[-p1^2 + q1^2] t]^2)^2));
```

```
V20[t_] :=
 (2 (p2 - q2) (p2 + q2) (p2 + q2 Sin[a yo2])
    (p2 (p2 + q2 Sin[a yo2]) - Cosh[a Sqrt[-p2^2 + q2^2] t] ((-p2^2 + q2^2) Cos[a yo2] + q2 (q2 + p2 Sin[a yo2])) -
      Sqrt[-p2^2 + q2^2] (q2 + q2 Cos[a yo2] + p2 Sin[a yo2]) Sinh[a Sqrt[-p2^2 + q2^2] t])) /
  ((q2^2 + (-p2 + q2) (p2 + q2) Cos[a yo2] - p2^2 Cosh[a Sqrt[-p2^2 + q2^2] t] -
      2 p2 q2 Sin[a yo2] Sinh[1/2 a Sqrt[-p2^2 + q2^2] t]^2)^2
    (1 +
      (-p2 (q2 + p2 Sin[a yo2]) + q2 Cosh[a Sqrt[-p2^2 + q2^2] t] (p2 + q2 Sin[a yo2]) +
        Sqrt[-p2^2 + q2^2] (p2 + q2 Sin[a yo2]) Sinh[a Sqrt[-p2^2 + q2^2] t])^2 /
       (q2^2 + (-p2 + q2) (p2 + q2) Cos[a yo2] - p2^2 Cosh[a Sqrt[-p2^2 + q2^2] t] -
         2 p2 q2 Sin[a yo2] Sinh[1/2 a Sqrt[-p2^2 + q2^2] t]^2)^2));
V120[t_] := V10[t] - V20[t];
α = (2 * π * Ps^2 * ω^2 * a1 * a2) / (ρl * (ω1^2 - ω^2) * (ω2^2 - ω^2)) (*N*m2*);
Ps = Sqrt[2 * ρl * cl^2 * Eac] (*Pa*);
D120 = (k * T * (μ + 1) * (1 + ahat^-1)) / (2 * π * μl * (3 * μ + 2) * a1) (*m2/S*);
ω1 = 1/a1 * Sqrt[(3 * γ * Px1)/ρl + (6 * γ * σhat)/(ρl * a1) - (2 * σhat)/(ρl * a1)] (*1/S*);
ω2 = 1/a2 * Sqrt[(3 * γ * Px2)/ρl + (6 * γ * σhat)/(ρl * a2) - (2 * σhat)/(ρl * a2)] (*1/S*);
Px1 = 101 325 + (2 * σhat)/a1 (*Pa*);
Px2 = 101 325 + (2 * σhat)/a2 (*Pa*);
F1 = ((1/c^2) * (3 * ρ - (κ * a1/c)^2))/(c^2 * (κ * a1/c)^6 + (3 * ρ - (κ * a1/c)^2)^2);
F2 = ((1/c^2) * (3 * ρ - (κ * a2/c)^2))/(c^2 * (κ * a2/c)^6 + (3 * ρ - (κ * a2/c)^2)^2);
p1 = a1^2/(3 * μl) * (ρl - ρg) * g (*m/S*);
q1 = a1^2/μl * κ * Eac * F1 (*m/S*);
```

```
p2 = a2^2/(3*μl) * (ρl - ρg) * g (*m/S*);
q2 = a2^2/μl * κ * Eac * F2 (*m/S*);
Nac1 = 3*κ*Eac*F1/((ρl - ρg)*g);
Nac2 = 3*κ*Eac*F2/((ρl - ρg)*g);
μg = 1.73*10^-5 (*Ns/m2 = kg/(S*m)*);
ρg = 1.25 (*kg/m3*);
cg = 343 (*m/S*);
μl = 0.001 (*Ns/m2 = kg/(S*m)*);
ρl = 998.23 (*kg/m3*);
cl = 1490 (*m/S*);
a1 = 0.000132 (*m*);
a2 = 0.000132 (*m*);
ahat = a2 / a1
μ = μg / μl;
ρ = ρg / ρl;
c = cg / cl;
k = 1.38065*10^-23 (*kg*m2/S2*K*);
T = 300 (*K*);
A = 3.7*10^-20 (*J*)
ω = f (*1/S*);
σhat = 0.0728 (*surface tension, kg/s2*);
γ = 1.4;
g = 9.81 (*m/S2*);
f = 435 000 (*Hz*);
Eac = 0.649 (*J/m3 = kg/m*s2*);
κ = 2*π/(cl/f) (*1/m*);
λ = cl / f (*m*);
a = 2*κ (*m*);
r = a1 + a2 + 0.0019 (*m*)
s0 = 2*r / (a1 + a2)
x = 222*π/180 (*radians*);
yo1 = 0.001759056596 (*m*) // N
yo2 = yo1 + r*Cos[x] (*m*)
xo1 = 0 (*m*);
xo2 = xo1 + r*Sin[x] (*m*);
```

```
sol =
 NDSolve[
  {s'[t] == (-2 * V120[t])/(a1 + a2) * L[t] * Cos[θ[t]] -
     (4 * D120)/(k * T * (a1 + a2)^2) * G[t] * (A * dVvdW[t] + (2 * α)/(a1 + a2) * 1/(s[t])^2),
   θ'[t] == (2 * V120[t] * M[t] * Sin[θ[t]])/(s[t] * (a1 + a2)), s[0] == 2 * r / (a1 + a2), θ[0] == x}, {s, θ},
  {t, 0, 1}, Method → StiffnessSwitching, AccuracyGoal → Infinity, MaxSteps → 10 000 000,
  MaxStepFraction → 1 / 100 000]
```

```
{{s → InterpolatingFunction[{{0., 1.}}, <>], θ → InterpolatingFunction[{{0., 1.}}, <>]}}
```

```
FindRoot[Evaluate[s[t] /. sol] - 2, {t, 0}]
```

```
{t → 0.509327}
```

```
{s[5.6370585066290565`*^-6], θ[5.6370585066290565`*^-6]/°} /. sol
```

```
{{2., 225.123}}
```

```
ptheta = Plot[Evaluate[θ[t]/° /. sol], {t, 0, 1},
  FrameLabel → {"Time (s)", "Separation  Angle , θ°"},
  BaseStyle → {FontFamily → "Times", FontSize → 14, FontWeight → Bold},
  PlotStyle → {Red, Thickness[0.01]}, PlotRange → {{0, 1}, {210, 240}}, Frame → True
  (*,Ticks→{units,Automatic}*)]
ps = Plot[Evaluate[s[t] /. sol], {t, 0, 0.05},
  FrameLabel → {"Time (s)", "Dimensionless  Separation , s"},
  BaseStyle → {FontFamily → "Times", FontSize → 14, FontWeight → Bold},
  PlotStyle → {Red, Thickness[0.01]}, PlotRange → {{0, 0.05}, {0, 20}},
  AxesOrigin → {0, 2}, Frame → True, Axes → False(*,Ticks→{units,Automatic}*)]
```

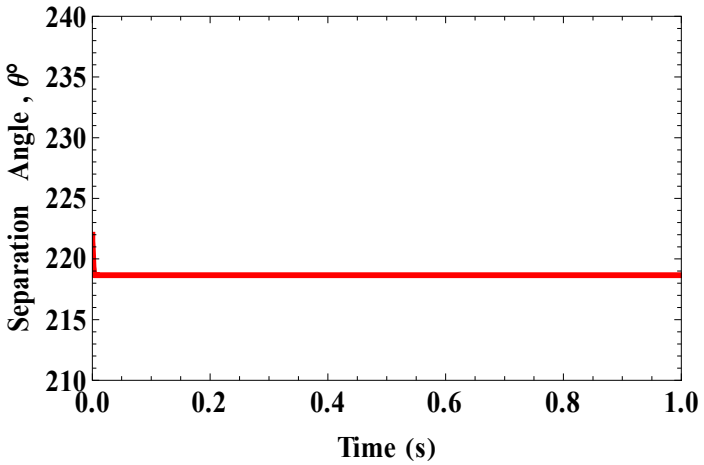

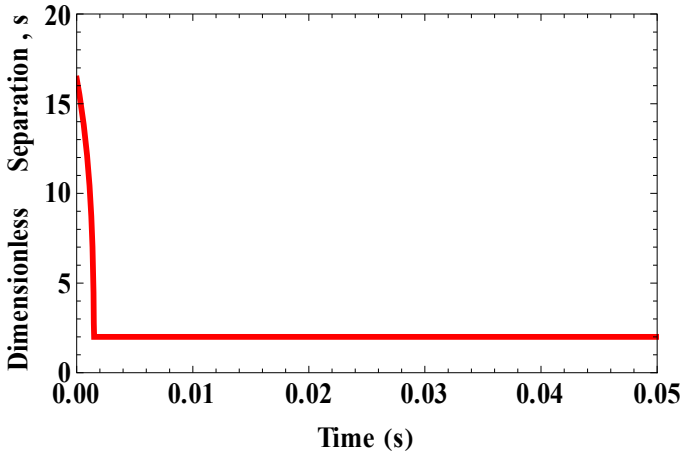


```
Δxf[t_] := (Evaluate[s[t] /. sol] * (a1 + a2) / 2) * Sin[Evaluate[θ[t] /. sol]]
Δyf[t_] := (Evaluate[s[t] /. sol] * (a1 + a2) / 2) * Cos[Evaluate[θ[t] /. sol]]

Export["test.xls",
 {Table[{Δxf[t], Δyf[t], Evaluate[s[t] /. sol], Evaluate[θ[t] /. sol]},
   {t, {0, 1*10^-9, 1*10^-8, 1*10^-7, 1*10^-6, 1*10^-5, 1*10^-4, 1*10^-3,
     1*10^-2, 0.1, 0.125, 0.15, 0.175, 0.2, 0.3, 0.4, 0.5, 1}}]}]
```

```
test.xls
```

```
Plot[Evaluate[(Δxf[t] /. sol) / (λ / 4)], {t, 0, 0.044}, Frame → True,
 FrameLabel → {"Time(s)", "Δxf/(λ/4)"}, BaseStyle → {FontFamily → "Times", FontSize → 14},
 PlotStyle → {Red, Thick}(*,PlotRange→{{0,0.02},{-2,2}}*)]
Plot[Evaluate[(Δyf[t] /. sol) / (λ / 4)], {t, 0, 0.044}(*,PlotRange→{{0,0.02},{-2,1}}*),
 Frame → True, FrameLabel → {"Time(s)", "Δyf/(λ/4)"},
 BaseStyle → {FontFamily → "Times", FontSize → 14}, PlotStyle → {Red, Thick}]
```

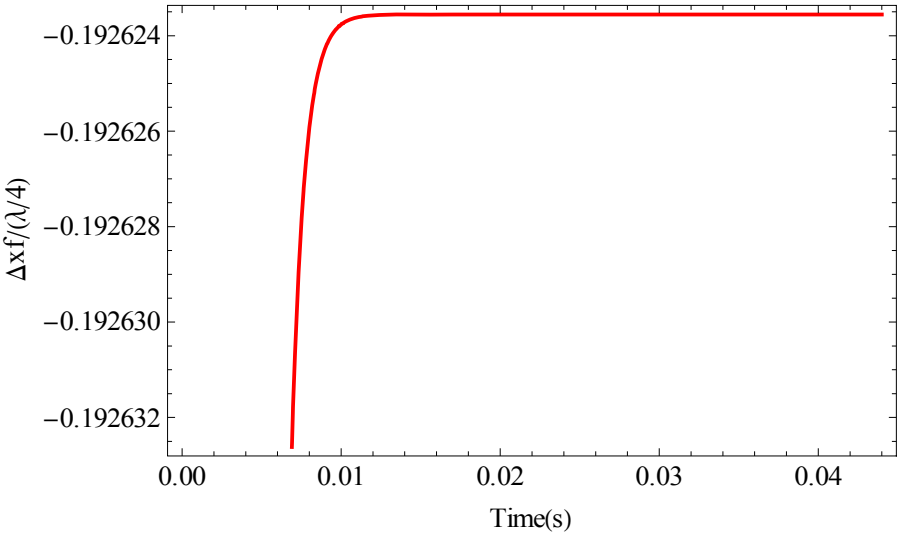

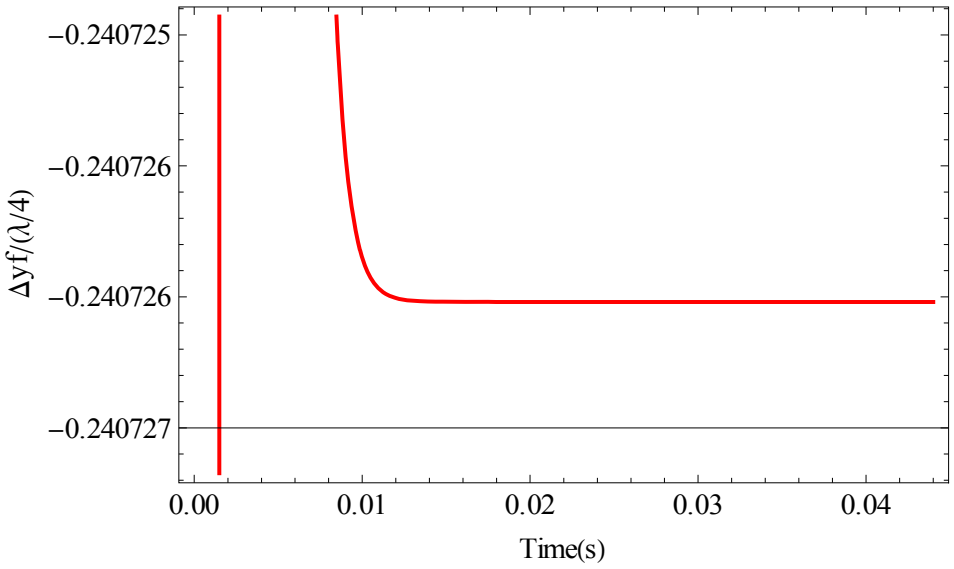


```
ParametricPlot[Evaluate[{(Δxf[t]) / (λ / 4), (Δyf[t]) / (λ / 4)} /. sol], {t, 0, 0.044},
 PlotRange → {{-2, 0}, {-2, 0}}, PlotPoints → 1000, AspectRatio → 0.5, Frame → True,
 FrameLabel → {"Δxf/(λ/4)", "Δyf/(λ/4)"},
 BaseStyle → {FontFamily → "Times", FontSize → 14, FontWeight → Bold},
 PlotStyle → {Red, Thickness[0.01]}, PlotPoints → 100, AspectRatio → 1]
```

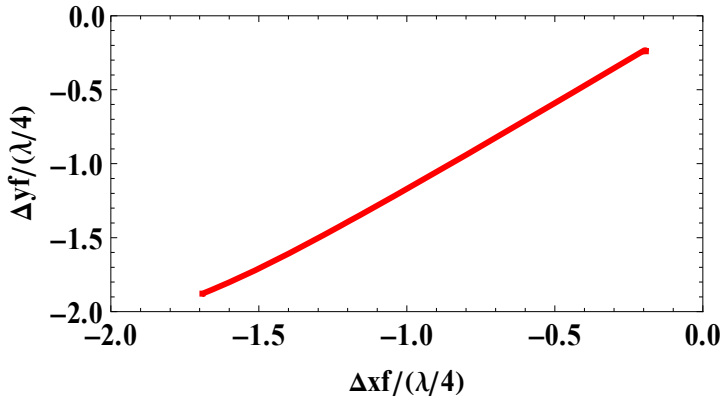


```
Export["testex1.xls", Table[t, {t, 0, 1, 0.001}]]
Export["testex2.xls", Table[(Δxf[t]) / (λ / 4), {t, 0, 1, 0.001}]]
Export["testex3.xls", Table[(Δyf[t]) / (λ / 4), {t, 0, 1, 0.001}]]
```

```
testex1.xls
```

```
testex2.xls
```

```
testex3.xls
```

```
Plot[Evaluate[V120[t] /. sol], {t, 0, 0.1}, AxesLabel → {"Time (s)", "V120 (m/s)"},
 BaseStyle → {FontFamily → "Times", FontSize → 14}, PlotStyle → {Red, Thick}(*,
 PlotRange→{{0,0.1},{-1,0.5}}*)]
```

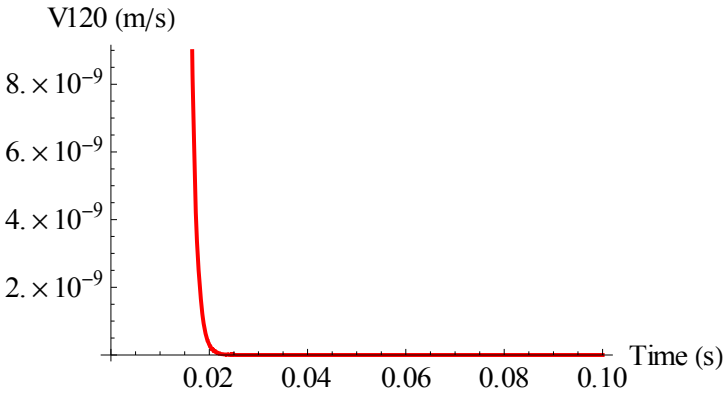


```
Plot[Evaluate[V10[t] /. sol], {t, 0, 0.02}, AxesLabel → {"Time (s)", "V10 (m/s)"},
 BaseStyle → {FontFamily → "Times", FontSize → 14}]
Plot[Evaluate[V20[t] /. sol], {t, 0, 0.02}, AxesLabel → {"Time (s)", "V20 (m/s)"},
 BaseStyle → {FontFamily → "Times", FontSize → 14}]
```

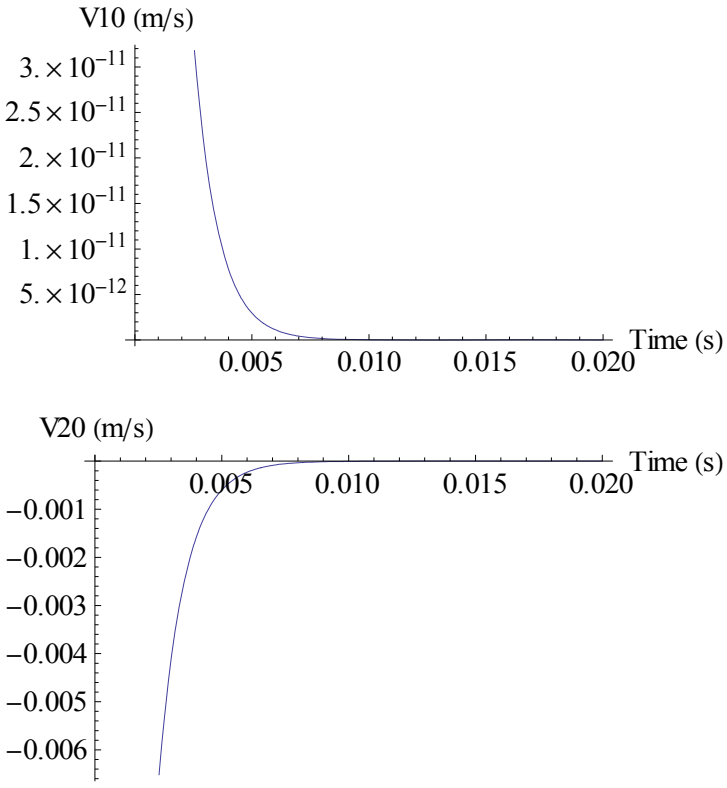

```
Plot[Evaluate[{s[t], s'[t]} /. sol], {t, 0, 0.001},
 AxesLabel → {"Time (s)", "Dimensionless Separation, s and s'"},
 BaseStyle → {FontFamily → "Times", FontSize → 14}, PlotStyle → {Dashed, Thick}
 (*,PlotRange→{{0,0.0002},{-5,5}}*)]
Plot[Evaluate[{θ[t]/°, θ'[t]/°} /. sol], {t, 0, 0.001},
 AxesLabel → {"Time (s)", "Separation Angle, θ° and θ'"},
 BaseStyle → {FontFamily → "Times", FontSize → 14}, PlotStyle → {Dashed, Thick}]
```

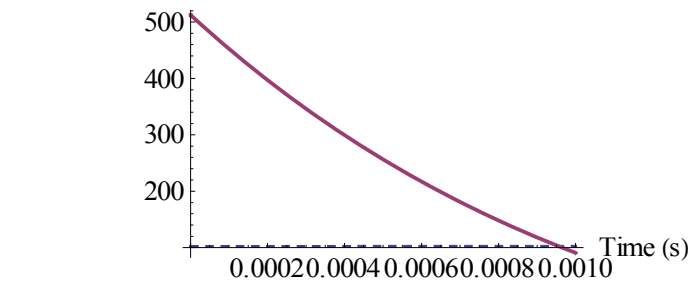

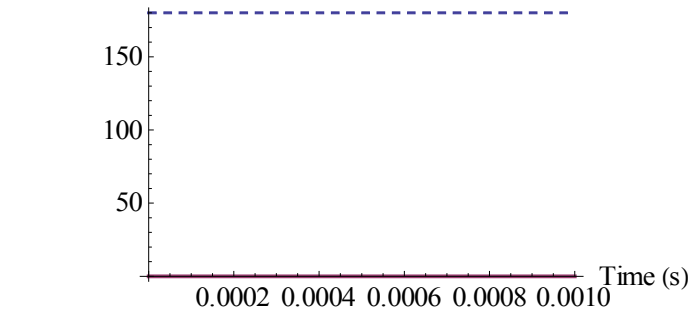


```
Plot[Evaluate[{s'[t]} /. sol], {t, 0, 0.5}, Frame → True,
 FrameLabel → {"Time (s)", "Dimensionless  Separation  Derivative , s'"},
 BaseStyle → {FontFamily → "Times", FontSize → 14}, PlotStyle → {Red, Thick},
 PlotRange → {{0, 0.0002}, {-100, 1}}]
```

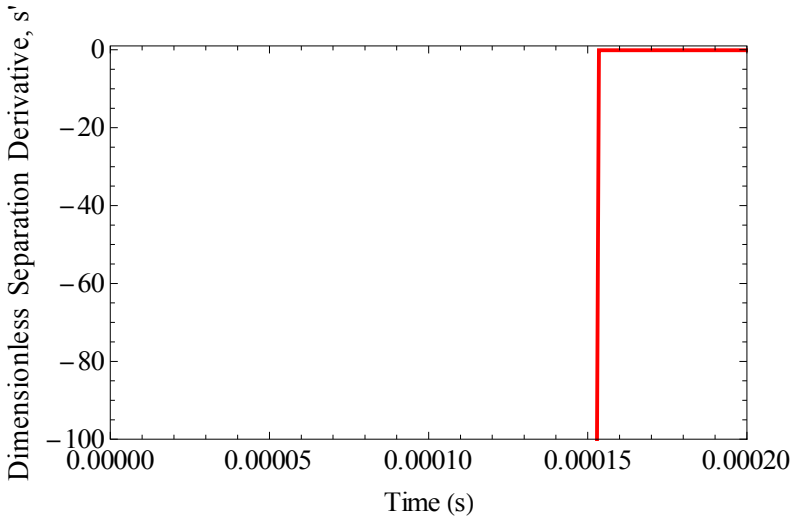

```
ps[[1]]
ptheta[[1]]
```

```
{{{}, {},
  {Hue[0.67, 0.6, 0.6], RGBColor[1, 0, 0], Thickness[0.01], Line[{{1.02041×10^-10, 19.2649},
     {1.53359×10^-6, 18.8234}, {3.06708×10^-6, 18.3514}, {4.60056×10^-6, 17.8462},
     {6.13405×10^-6, 17.304}, {7.66754×10^-6, 16.72}, {9.20103×10^-6, 16.0874},
     {0.0000107345, 15.397}, {0.000012268, 14.636}, {0.0000138015, 13.7853},
     {0.000015335, 12.815}, {0.0000168685, 11.6745}, {0.000018402, 10.2649},
     {0.0000199354, 8.33867}, {0.0000214689, 4.66942}, {0.0000230024, 1.38714},
     {0.0000245359, 1.38714}, {0.0000260694, 1.38714}, {0.0000276029, 1.38714},
     {0.0000291364, 1.38714}, {0.0000306699, 1.38714}, {0.0000322033, 1.38714},
     {0.0000337368, 1.38714}, {0.0000352703, 1.38714}, {0.0000368038, 1.38714},
     {0.0000383373, 1.38714}, {0.0000398708, 1.38714}, {0.0000414043, 1.38715},
     {0.0000429378, 1.38715}, {0.0000444712, 1.38715}, {0.0000460047, 1.38715},
     {0.0000475382, 1.38715}, {0.0000490717, 1.38715}, {0.0000506052, 1.38715},
     {0.0000521387, 1.38715}, {0.0000536722, 1.38715}, {0.0000552057, 1.38715},
     {0.0000567391, 1.38715}, {0.0000582726, 1.38715}, {0.0000598061, 1.38715},
     {0.0000613396, 1.38715}, {0.0000628731, 1.38715}, {0.0000644066, 1.38715},
     {0.0000659401, 1.38715}, {0.0000674736, 1.38715}, {0.000069007, 1.38715},
     {0.0000705405, 1.38715}, {0.000072074, 1.38715}, {0.0000736075, 1.38715},
     {0.0000766745, 1.38715}, {0.0000797415, 1.38715}, {0.0000828084, 1.38715},
     {0.0000858754, 1.38715}, {0.0000920094, 1.38715}, {0.0000981433, 1.38715},
     {0.000151343, 1.38715}, {0.000204542, 1.38715}, {0.000254216, 1.38715},
     {0.000303889, 1.38715}, {0.000352589, 1.38715}, {0.000401288, 1.38715},
     {0.000454115, 1.38715}, {0.000506942, 1.38715}, {0.000556244, 1.38715},
     {0.000605546, 1.38715}, {0.000658975, 1.38715}, {0.000712404, 1.38715},
     {0.000764859, 1.38715}, {0.000817314, 1.38715}, {0.000915173, 1.38715},
     {0.00096823, 1.38715}, {0.00102129, 1.38715}, {0.00107082, 1.38715},
     {0.00112035, 1.38715}, {0.00116891, 1.38715}, {0.00121746, 1.38715},
     {0.00127015, 1.38715}, {0.00132283, 1.38715}, {0.00137199, 1.38715},
     {0.00142115, 1.38715}, {0.00147444, 1.38715}, {0.00152773, 1.38715},
     {0.00158004, 1.38715}, {0.00163235, 1.38715}, {0.00168114, 1.38715},
     {0.00172993, 1.38715}, {0.00178284, 1.38715}, {0.00183576, 1.38715},
     {0.00188515, 1.38715}, {0.00193454, 1.38715}, {0.00198805, 1.38715},
     {0.00204157, 1.38715}, {0.00209411, 1.38715}, {0.00214666, 1.38715},
     {0.00219567, 1.38715}, {0.00224469, 1.38715}, {0.00229784, 1.38715},
     {0.00235098, 1.38715}, {0.0024006, 1.38715}, {0.00245022, 1.38715},
     {0.00249886, 1.38715}, {0.00254751, 1.38715}, {0.00260028, 1.38715},
     {0.00265306, 1.38715}, {0.0027023, 1.38715}, {0.00275155, 1.38715},
     {0.00280492, 1.38715}, {0.0028583, 1.38715}, {0.0029107, 1.38715},
     {0.0029631, 1.38715}, {0.00301198, 1.38715}, {0.00306085, 1.38715},
     {0.00311385, 1.38715}, {0.00316686, 1.38715}, {0.00326581, 1.38715},
     {0.00331431, 1.38715}, {0.00336282, 1.38715}, {0.00341545, 1.38715},
     {0.00346808, 1.38715}, {0.00351718, 1.38715}, {0.00356629, 1.38715},
     {0.00361952, 1.38715}, {0.00367275, 1.38715}, {0.00372246, 1.38715},
     {0.00377217, 1.38715}, {0.0038209, 1.38715}, {0.00386964, 1.38715},
     {0.0039225, 1.38715}, {0.00397536, 1.38715}, {0.00402469, 1.38715},
     {0.00407403, 1.38715}, {0.00412749, 1.38715}, {0.00418095, 1.38715},
     {0.00423344, 1.38715}, {0.00428593, 1.38715}, {0.00433489, 1.38715},
     {0.00438386, 1.38715}, {0.00443695, 1.38715}, {0.00449004, 1.38715},
     {0.0045396, 1.38715}, {0.00458917, 1.38715}, {0.00463776, 1.38715},
     {0.00468635, 1.38715}, {0.00473907, 1.38715}, {0.00479179, 1.38715},
     {0.00484098, 1.38715}, {0.00489017, 1.38715}, {0.00494349, 1.38715},
     {0.00499681, 1.38715}, {0.00499841, 1.38715}, {0.005, 1.38715}}]}}}
```

```
{{{}, {}, {Hue[0.67, 0.6, 0.6], RGBColor[1, 0, 0], Thickness[0.01],
   Line[{{2.04082 × 10^-8, 222.998}, {0.000306718, 221.026}, {0.000613415, 221.026},
     {0.000920113, 221.026}, {0.00122681, 221.026}, {0.00184021, 221.026},
     {0.0024536, 221.026}, {0.00368039, 221.026}, {0.00490718, 221.026},
     {0.00736076, 221.026}, {0.00981434, 221.026}, {0.0147215, 221.026},
     {0.0196287, 221.026}, {0.0302685, 221.026}, {0.0409084, 221.026}, {0.0607779, 221.026},
     {0.0802576, 221.026}, {0.101388, 221.026}, {0.121109, 221.026}, {0.142481, 221.026},
     {0.163463, 221.026}, {0.183035, 221.026}, {0.204257, 221.026}, {0.22407, 221.026},
     {0.243493, 221.026}, {0.264567, 221.026}, {0.284231, 221.026}, {0.305546, 221.026},
     {0.326471, 221.026}, {0.345986, 221.026}, {0.367151, 221.026}, {0.386907, 221.026},
     {0.408314, 221.026}, {0.429331, 221.026}, {0.448938, 221.026}, {0.470196, 221.026},
     {0.490044, 221.026}, {0.509502, 221.026}, {0.530611, 221.026}, {0.55031, 221.026},
     {0.57166, 221.026}, {0.59262, 221.026}, {0.61217, 221.026}, {0.633371, 221.026},
     {0.653162, 221.026}, {0.672563, 221.026}, {0.693616, 221.026}, {0.713258, 221.026},
     {0.734551, 221.026}, {0.754434, 221.026}, {0.773927, 221.026}, {0.795071, 221.026},
     {0.814805, 221.026}, {0.83619, 221.026}, {0.857186, 221.026}, {0.876771, 221.026},
     {0.898007, 221.026}, {0.917833, 221.026}, {0.93727, 221.026}, {0.958357, 221.026},
     {0.978034, 221.026}, {0.999363, 221.026}, {0.999681, 221.026}, {1., 221.026}}]}}}
```

References

1. Skudrzyk, Eugen; The Foundations of Acoustics; © 1971, Springer-Verlag, Wien-New York.
2. "Linear Wave Equation," EqWorld, http://eqworld.ipmnet.ru/en/solutions/lpde/wave-toc.pdf
3. "Sound," HyperPhysics, http://hyperphysics.phy-astr.gsu.edu/hbase/sound/soucon.html
4. "Sound Wave," Whatis?com, http://whatis.techtarget.com/definition/0,,sid9_gci900512,00.html
5. Pangu, Gautam; Acoustically aided coalescence of droplets in aqueous emulsions; Dissertation, Case Western Reserve University, 2005.
6. Feke, D.L., Graf, J.; Nakagawa, M.; "Coalescence, transport, and separations of gas bubbles in liquids using ultrasonic processing techniques," proposal submitted to NASA, 02-OBPR-03-C-0108-0054, Dec. 2003.
7. Yosioka, K.; Kawasima, Y.; "Acoustic radiation pressure on a compressible sphere," *Acustica* **5**, 167 (1955).
8. Wu, J; Du, G; "Acoustic radiation force on a small compressible sphere in a focused beam," *J. Acoust. Soc. Am.* **87**, 997 (1990).
9. Asaki, T.J.; Marston, P.L.; "Acoustic radiation force on a bubble driven above resonance," *J. Acoust. Soc. Am.* **96**, 3096 (1994).
10. Lee, C.P; Wang, T.G.; "Acoustic radiation force on a bubble," *J. Acoust. Soc. Am.* **93**, 997 (1993).
11. Woodside, S.M.; Piret, J.M.; Gröschl, M.; Benes, E.; Bowen, B.D.; "Acoustic force distribution in resonators for ultrasonic particle separation," *AICHE* **44**, 1976 (1998).
12. Gor'kov, L.P.; "On the forces acting on a small particle in an acoustical field in an ideal fluid," *Sov. Phys. Doklady* **6**, 773 (1962).
13. Whitworth, G.; Coakley, W.T.; "Particle column formation in a stationary ultrasonic field," *J. Acoust. Soc. Am.* **91**, 79 (1992).
14. Doinikov, A.A.; "Effects of the second harmonic on the secondary Bjerknes force," *Phys. Rev. E* **59**, 3016 (1999).
15. Doinikov, A.A.; "Viscous effects on the interaction force between two small gas bubbles in a weak acoustic field," *J. Acoust. Soc. Am.* **111**, 1602 (2002).
16. Doinikov, A.A.; "Bjerknes forces between two bubbles in a viscous fluid," *J. Acoust. Soc. Am.* **106**, 3305 (1999).
17. Ida, M.; "Alternative interpretation of the sign reversal of secondary Bjerknes force acting between two pulsating gas bubbles," *Phys. Rev. E* **67**, 1063 (2003).
18. Weiser, M.A.H.; Apfel, R.E.; Neppiras, E.A.; "Interparticle forces on red cells in a standing wave field," *Acustica* **56**, 114 (1984).
19. Apfel, R.E.; "Acoustically induced square law forces and some speculations about gravitation," *Am. J. Phys.* **56**, 726 (1988).
20. "A summary of the early development of ultrasonics prior to the 1950s leading to medical applications," http://www.ob-ultrasound.net/ultrasonics_history.html.

21. "Pythagoras," Stanford Encyclopedia of Philosophy, http://plato.stanford.edu/entries/pythagoras/.
22. Lord Rayleigh, The Theory of Sound, 1877-1878.
23. "Paul Langevin," Obstetric Ultrasound, http://www.ob-ultrasound.net/langevin.html.
24. King, L.V.; "On the acoustic radiation pressure on spheres," *Proceedings of the Royal Society of London A* **147**, 212 (1934).
25. King, L.V.; "On the acoustic radiation pressure on circular disks: inertia and diffraction corrections," *Proceedings of the Royal Society of London A* **153**, 1 (1935).
26. Riera-Franco de Sarabia, E.; Gallego-Juarez, J.A.; Rodriguez, G.; Elvira-Segura, L.; Gonzalez-Gomez, I.; "Application of high-power ultrasound to enhance fluid/solid particle separation processes," *Ultrasonics* **38**, 642 (2000).
27. Tolt, T.L.; Feke, D.L.; *Proceeding of the 23rd Intersociety Energy Conversion Engineering Conference* **4**, 327 (1988).
28. Tolt, T.L.; Feke, D.L.; "Separation of dispersed phases from liquids in acoustically driven chambers," *Chemical Engineering Science* **48**, 527 (1993).
29. Tolt, T.L.; Agglomeration and collection of fine secondary phases in flowing suspensions utilizing resonant ultrasonic fields, Dissertation, Case Western Reserve University, 1990.
30. Mandralis, Z.I.; Feke, D.L.; "Continuous suspension fractionation using acoustic and divided-flow fields," *Chemical Engineering Science* **48**, 3897 (1993).
31. Mandralis, Z.I.; Feke, D.L.; Bolek, W.; Burger, W.; Benes, E.; "Enhanced synchronized ultrasonic and flow-field fractionation of suspensions," *Ultrasonics* **32**, 113 (1994).
32. Mandralis, Z.I.; Wernet, J.H.; Feke, D.L.; "Effects of double-layer relaxation on the interaction of colloidal particles approaching at constant speed," *Journal of Colloid and Interface Science* **182**, 26 (1996).
33. Johnson, D.A.; Feke, D.L.; "Methodology for fractionating suspended particles using ultrasonic standing wave and divided flow fields," *Separations Technology* **5**, 251 (1995).
34. Gupta, S.; Feke, D.L.; Manas-Zloczower, I.; "Fractionation of mixed particulate solids according to compressibility using ultrasonic standing wave fields," *Chemical Engineering Science* **50**, 3275 (1995).
35. Gupta, S.; Feke, D.L.; "Acoustically driven collection of suspended particles within porous media," *Ultrasonics* **35**, 131 (1997).
36. Gupta, S.; Feke, D.L.; "Filtration of particulate suspensions in acoustically driven porous media," *AICHE Journal* **44**, 1005 (1998).
37. Grossner, M.T.; Penrod, A.E.; Belovich, J.M.; Feke, D.L.; "Single fiber model of particle retention in an acoustically driven porous mesh," *Ultrasonics* **41**, 65 (2003).
38. Pangu, G.D.; Feke, D.L.; "Acoustically aided separation of oil droplets from aqueous emulsions," *Chem. Eng. Science* **59**, 3183 (2004).
39. Pangu, G.D.; Feke, D.L.; "Droplet transport and coalescence kinetics in emulsions subjected to acoustic fields," *Ultrasonics* **46**, 289 (2007).

40. Marston, P.L.; Apfel, R.E.; "Acoustically forced shape oscillation of hydrocarbon drops levitated in water," *Journal of Colloid and Interface Science* **68**, 280 (1979).
41. Gardner, E.A.; Apfel, R.E.; "Using acoustics to study and stimulate the coalescence of oil drops surrounded by water," *Journal of Colloid and Interface Science* **159**, 226 (1993).
42. Lamb, H.; Hydrodynamics, 6th edition, Cambridge University Press, London, (1932).
43. Marston, P.L.; "Shape oscillation and static deformation of drops and bubbles driven by modulated radiation stresses – theory;" *J. Acoust. Soc,* **67** (1), 15 (1980).
44. Marston, P.L.; LoPorto-Arione, S.E.; Pullen, G.L.; "Quadrupole projection of the radiation pressure on a compressible sphere;" *J. Acoust. Soc.* **69** (5), 1499 (1981).
45. Yamakoshi, Yoshiki; Ozawa, Yoshiyuki; Masuda, Nobuyuki; "Holographic visualization of secondary ultrasonic waves radiated from micro bubbles," IEEE Ultrasonics Symposium, 1969 (2002).
46. Crum, L.A.; "The polytropic exponent of gas contained within air bubbles pulsating in a liquid," *J. Acoust. Soc. Am.* **73**, 116 (1983).
47. Ida, M; "Avoided crossings in three coupled oscillators as a model system of acoustic bubbles," *Phys. Rev. E* **72**, 036306 (2005).
48. Ida, M; "Phase properties and interaction force of acoustically interacting bubbles: a complementary study of the transition frequency," Physics of Fluids **17**, 097107 (2005).
49. Zheng, X.; Apfel, R.E.; "Acoustic interaction forces between two fluid spheres in an acoustic field," *J. Acoust. Soc. Am.* **97**, 2218 (1995).
50. Harkin, A.; Kaper, T.J.; Nadim, A.; "Coupled pulsation and translation of two gas bubbles in a liquid," *J. Fluid Mech.* **445**, 377 (2001).
51. Barbat, T.; Ashgriz, N.; "Planar dynamics of two interacting bubbles in an acoustic field," *Applied Mathematics and Computation* **157**, 775 (2004).
52. Zhang, X.; Davis, R.H.; "The rate of collisions due to Brownian or gravitational motion of small drops," *J. Fluid Mech.* **230**, 470 (1991).
53. Israelachvili, J.; Intermolecular & Surface Forces, 2nd Edition, Academic Press, San Diego, 1992.
54. Haber, S.; Hesroni, G.; Solan, A.; "On the low Reynolds number motion of two droplets," *Intl. J. Multiphase Flow* **1**, 57 (1973).
55. Rushton, E.; Davies, G.A.; "The slow unsteady settling of two fluid spheres along their line of centers," *Appl. Sci. Res.* **28**, 37 (1973).
56. Zinchenko, A.Z.; "Calculation of hydrodynamic interactions between two drops in a viscous medium," *Prikl. Mat. Mech.* **44**, 30 (1980).
57. Davis, R.H.; Schonberg, J.A.; Rallison, J.M.; "The lubrication force between two viscous drops," *Phys. Fluids A* **1**, 77 (1989).
58. Hetsroni, G.; Haber, S.; "Low Reynolds number motion of two drops submerged in an unbounded arbitrary velocity field," *Int. J. Multiphase Flow* **4**, 1 (1978).
59. Abe, Y.; Kawaji, M.; Watanabe, T.; "Study on bubble motion control by ultrasonic wave," *Experimental Thermal and Fluid Science* **26**, 817 (2002).

60. Watanabe, T.; Kukita, Y.; "Translational and radial motions of a bubble in an acoustic standing wave field," *Phys. Fluids A* **5**, 2682 (1993).
61. Marston, P.L.; "Evaporation-condensation resonance frequency of oscillating vapor bubbles," *J. Acoust. Soc. Am.* **66**, 1516 (1979).
62. Doinikov, A.A.; "Viscous effects on the interaction force between two small gas bubbles in a weak acoustic field," *J. Acoust. Soc. Am.* **111**, 1602 (2002).
63. Ida, M.; "A characteristic frequency of two mutually interacting gas bubbles in an acoustic field," *Phys. Let. A* **297**, 210 (2002).
64. Kornfeld, M.; Suvorov, L.; "On the destructive action of cavitation," *J. Appl. Phys.* **15**, 143 (1944).
65. Zabolotskaya, E.A.; "Interaction of gas bubbles in a sound field," *Sov. Phys. Acoust.* **30**, 365 (1984).
66. Oguz, H.N.; Prosperetti, A.; "A generalization of the impulse and virial theorems with an application to bubble oscillations," *J. Fluid Mech.* **218**, 143 (1990).
67. Doinikov, A.A.; Zavtrak, S.T.; "On the mutual interaction of two gas bubbles in a sound field," *Phys. Fluids* **7**, 1923 (1995).
68. Mettin, R.; Akhatov, I.; Parlitz, U.; Ohl, C.D.; Lauterborn, W.; "Bjerknew forces between small cavitation bubbles in a strong field," *Phys. Rev. E* **56**, 2924 (1997).
69. Zavtrak, S.T.; "On Bjerknes interaction force of two gas bubbles in a sound wave field," *Akust. Zh.* **33**, 240 (1987).
70. Kobelev, Y.A.; Ostrovskii, L.A.; Sutin, A.M.; "Effect of self-clearing for acoustic waves in a liquid with gas bubbles," *Pis'ma Zh. Eksp. Teor. Fiz.* **30**, 423 (1979).
71. Doinikov, A.A.; Zavtrak, S.T.; "Radiation forces between two bubbles in a compressible liquid," *J. Acoust. Soc. Am.* **102**, 1424 (1997).
72. Doinikov, A.A.; "Translational motion of two interacting bubbles in a strong acoustic field," *Phys. Rev. E* **64**, 026301 (2001).
73. Barbat, T.; Ashgriz, N.; Liu, C.S.; "Dynamics of two interacting bubbles in an acoustic field," *J. Fluid Mech.* **389**, 137 (1999).
74. Barbat, T.; Ashgriz, N.; "Planar dynamics of two interacting bubbles in an acoustic field," *Applied Mathematics and Computation* **157**, 775 (2004).
75. Doinikov, A.A.; Zavtrak, S.T.; "On the 'bubbles grapes' induced by a sound field," *J. Acoust. Soc. Am.* **99**, 3849 (1996).
76. Mettin, R.; Akhatov, I.; Parlitz, U.; Ohl, C.D.; Lauterborn, W.; "Bjerknes forces between small cavitation bubbles in a strong acoustic field," *Phys. Rev. E* **56**, 2924 (1997).
77. Harkin, A.; Kaper, T.J.; Nadim, A.; "Coupled pulsation and translation of two gas bubbles in a liquid," *J. Fluid Mech.* **445**, 377 (2001).
78. Crum, L.A.; Prosperetti, A.; "Nonlinear oscillations of gas bubbles in liquids: an interpretation of some experimental results," *J. Acoust. Soc. Am.* **73**, 121 (1983).
79. Eller, A.; "Force on a bubble in a standing acoustic wave," *J. Acoust. Soc. Am.* **43**, 170 (1968).
80. Batchelor, G.K.; "Sedimentation in a dilute polydisperse system of interacting spheres," *J. Fluid Mech.* **119**, 379 (1982).
81. Doinikov, A.A.; "Dissipative effects on Bjerknes forces between two bubbles," *J. Acoust. Soc. Am.* **102**, 747 (1997).

82. Hitt, D.L.; Prosperetti, A.; "Viscous forces on acoustically levitated gas bubbles," *Nonlinear Analysis* **63**, 1517 (2005).
83. Khabeev, N.S.; "Resonance properties of soluble gas bubbles," *Int. J. Heat and Mass Transfer* **49**, 1022 (2006).
84. Devin, C. Jr.; "Survey of thermal, radiation, and viscous damping of pulsating air bubbles in water," *J. Acoust. Soc. Am.* **31**, 1654 (1959).
85. Sitter, J.S.; Snyder, T.J.; Chung, J.N.; Marston, P.L.; "Acoustic field interactions with a boiling system under terrestrial gravity and microgravity," *J. Acoust. Soc. Am.* **104**, 2561 (1998).
86. Abe, Y.; Kawaji, M.; Watanabe, T.; "Study on the bubble motion control by ultrasonic wave," *Experimental Thermal and Fluid Science* **26**,817 (2002).
87. Hawkes, J.J.; Cefai, J.J.; Barrow, D.A.; Coakley, W.T.; Briarty, L.G.; "Ultrasonic manipulation of particles in microgravity," *J. Phys. D: Appl. Phys.* **31**, 1673 (1998).
88. Sunartio, D.; Ashokkumar, M.; Grieser, F.; "Study of the coalescence of acoustic bubbles as a function of frequency, power, and water-soluble additives," *JACS* **129**, 6031 (2007).
89. Crum, L.A.; "Measurements of the growth of air bubbles by rectified diffusion," *J. Acoust. Soc. Am.* **68**, 203 (1980).
90. Crum, L.A.; "Acoustic cavitation series part five – rectified diffusion," *Ultrasonics* **22**, 215 (1984).
91. Asaki, T.J.; Marston, P.; "The effects of a soluble surfactant on quadrupole shape oscillations and dissolution of air bubbles in water," *J. Acoust. Soc. Am.* **102**, 3372 (1997).
92. Asaki, T.J.; Shape oscillations of bubbles in water driven by modulated ultrasonic radiation pressure and applications to interfacial dynamics, Dissertation, Washington State University, 1995.
93. Giribabu, K.; Ghosh, P.; "Adsorption of nonionic surfactants at fluid-fluid interfaces: importance in the coalescence of bubbles and drops," *Chem. Eng. Sci.* **62**, 3057 (2007).
94. Malysa, K.; Krasowska, M.; Krzan, M.; "Influence of surface active substances on bubble motion and collision with various interfaces," *Advances in Colloid and Interface Science* **114-115**, 205 (2005).
95. Levich, V.G.; Physicochemical hydrodynamics, Englewood Clifts: Prentice-Hall, 1962.
96. Frumkin, A.N.; Levich, V.G.; *Zh. Phys. Chim.* **21**, 1183 (1947).
97. "Cavitation" from Encyclopedia of Britannica Online, http://www.britannica.com/eb/article-9021920/cavitation.
98. "High power ultrasound and acoustic cavitation," National Physical Laboratory, http://www.npl.co.uk/server.php?show=ConWebDoc.1875.
99. "Cavitation Tunnel Instrumentation" from Australian Maritime College, http://www.amc.edu.au/cavitation.tunnel/instrumentation.
100. Leighton, T.G.; "Bubble population phenomena in acoustic cavitation," *Ultrasonics Sonochemistry* **2**, S123 (1995).
101. Ashokkumar, M.; Lee, J.; Kentish, S.; Grieser, F.; "Bubbles in an acoustic field: an overview," *Ultrasonics Sonochemistry* **14**, 470 (2007).

102. Putterman, S.J.; "Sonoluminescence: Sound into Light," http://www.physics.ucla.edu/Sonoluminescence/sono.pdf (picture from http://en.wikipedia.org/wiki/Image:Sonoluminescence.png).
103. Akhatov, I.; Parlitz, U.; Lauterborn, W.; "Pattern formation in acoustic cavitation," *J. Acoust. Soc. Am.* **96**, 3627 (1994).
104. Lauterborn, W.; Kurz, T.; Geisler, R.; Schanz, D.; Lindau, O.; "Acoustic cavitation, bubble dynamics and sonoluminescence," *Ultrasonics Sonochemistry* **14**, 484 (2007).
105. Hatanaka, S.; Yasui, K.; Kozuka, T.; Tuziuti, T.; Mitome, H.; "Influence of bubble clustering on multibubble sonoluminescence," *Ultrasonics* **40**, 655 (2002).
106. Posakony, G.L.; Greenwood, L.R.; Ahmed, S.; "Stable multibubble sonoluminescence bubble patterns," *Ultrasonics* **44**, e445 (2006).
107. Maisonhaut, E.; Del Campo, F.J.; Compton, R.G.; "Microelectrode study of single cavitational bubbles induced by 500 kHz ultrasound," *Ultrasonics Sonochemistry* **9**, 275 (2002).
108. Doinikov, A.A.; "Mutual interaction between a bubble and a drop in a sound field," *J. Acoust. Soc. Am.* **99**, 3373 (1996).
109. Doinikov, A.A.; Zavtrak, S.T.; "Interaction force between a bubble and a solid particle in a sound field," *Ultrasonics* **34**, 807 (1996).
110. Gould, R.K.; Coakley, W.T.; Grundy, M.A.; "Upper sound pressure limits on particle concentration in fields of ultrasonic standing-wave at megahertz frequencies," *Ultrasonics* **4**, 239 (1992).
111. Ata, S.; Jameson, G.J.; "The formation of bubble clusters in flotation cells," *Int. J. Mineral Processing* **76**, 123 (2005).
112. O'Brien, W.D. Jr.; "Assessing the risks for modern diagnostic ultrasound imaging," http://www.brl.uiuc.edu/Projects/Bioeffects/Assessing.php.
113. Hendee, W.R.; Holmes, J.H.; Medical physics of CT and ultrasound: tissue imaging and characterization, American Institute of Physics, New York, 1980.
114. Wild, J.J.; "The use of ultrasonic pulses for the measurement of biologic tissues and the detection of tissue density changes," *Surgery* **27**, 183 (1950).
115. Wild, J.J.; Reid, J.M.; "The effects of biological tissues on 15-mc pulsed ultrasound," *J. Acoust. Soc. Am.* **25**, 270 (1953).
116. ter Harr, G.; Wyard, S.J.; "Blood cell banding in ultrasonic standing wave fields: a physical analysis," *Ultras. Med. Bio.* **4**, 111 (1978).
117. Weiser, M.A.H.; Apfel, R.E.; Neppiras, E.A.; "Interparticle forces on red cells in a standing wave field," *Acustica* **56**, 114 (1984).
118. Zhou, C.; Pivarnik, P.; Rand, A.G.; Letcher, S.V.; "Acoustic standing-wave enhancement of a fiber-optic *Salmonella* biosensor," *Biosensors & Bioelectronics* **13**, 495 (1998).
119. Coakley, W.T.; Hawkes, J.J.; Sobanski, M.A.; Cousins, C.M.; Spengler, J.; "Analytical scale ultrasonic standing wave manipulation of cells and microparticles," *Ultrasonics* **38**, 638 (2000).
120. Hawkes, J.J.; Limaye, M.S.; Coakley, W.T.; "Filtration of bacteria and yeast by ultrasound-enhanced sedimentation," *J. Appl. Microbiol.* **82**, 39 (1997).

121. Limaye, M.S.; Coakley, W.T.; "Clarification of small volume microbial suspensions in an ultrasonic standing wave," *J. Appl. Microbiol.* **84**, S150 (1998).
122. Cosgrove, D.; "The background and clinical applications of ultrasound contrast media," Hammersmith Hospital, London, UK; http://www.star-program.com/data--star-program/upload/star_abstracts_681_2001_Cosgrove_1.pdf.
123. Calliada, F.; Campani, R.; Bottinelli, O.; Bozzini, A.; Sommaruga, M.G.; "Ultrasound contrast agents basic principles," *European Journal of Radiology* **27**, S157 (1998).
124. Kim, Y.P.; Fregonese, M.; Mazille, H.; Feron, D.; Santarini, G.; "Ability of acoustic emission technique for detection and monitoring of crevice corrosion on 304L austenitic stainless steel," *NDT&E Int.* **36**, 553 (2003).
125. Birkin, P.R.; Hirsimaki, H.-M.; Frey, J.G.; Leighton, T.G.; "Mass transfer enhancement produced by laser induced cavitation," *Electrochemistry Communications* **8**, 1603 (2006).
126. Marmottant, P.; Hilgenfeldt, S.; "A bubble-driven microfluidics transport element for bioengineering," *PNAS* **101**, 9523 (2004).
127. Liu, R.H.; Yang, J.; Pindera, M.Z.; Athavale, M.; Grodzinski, P.; "Bubble-induced acoustic micromixing," *Lab on a Chip* **2**, 151 (2002).
128. Pandy, A.K.; Kalsi, P.C.; Iyer, R.H.; "Effects of high intensity ultrasound in chemical etching of particle tracks in solid state nuclear track detectors," *NIM B* **134**, 393 (1998).
129. Jyoti, K.K.; Pandit, A.B.; "Hybrid cavitation methods for water disinfection: simultaneous use of chemicals with cavitation," *Ultrasonics Sonochemistry* **10**, 255 (2003).
130. Laschimke, R.; Burger, M.; Vallen, H.; "Acoustic emission analysis and experiments with physical model systems reveal a peculiar nature of the xylem tension," *J. Plant Physiology* **163**, 996 (2006).
131. "Rectified diffusion," from Discovery of Sound in the Sea, http://www.dosits.org/glossary/pop/r-diffusion.htm.
132. Rusinko, D.; Design and Optimization of an Ultrasonic Standing Wave Chamber, Dissertation, Case Western Reserve University, 2000.